LOCAL NATURAL CONVECTION HEAT TRANSFER MEASUREMENTS USING A THIN GOLD-FILM TECHNIQUE

by

© William Stuart Neill

A Thesis Submitted to the Faculty of Graduate Studies and Research in Partial Fulfillment of the Requirements for the Degree of Master of Engineering

Department of Mechanical Engineering
McGill University
Montreal, Canada

NAT. CONVECTION HEAT TRANSFER MEASUREMENTS USING A GOLD-FILM TECHNIQUE

BY

WILLIAM STUART NEILL
DEPT. OF MECH. ENG.

ABSTRACT

This thesis deals with the development and testing of a gold-film technique for taking local natural convection heat transfer measurements. As the rates of heat transfer by natural convection are often of the same magnitude as the heat transfer rates due to wall conduction and radiation, the proposed technique is specially designed to take into account these two modes of heat transfer.

The proposed gold-film technique was evaluated by applying it to take measurements of two-dimensional, steady state, laminar natural convection along a vertical flat plate and in a horizontal concentric annulus, and comparing the experimental results against the corresponding analytical and numerical results.

In the vertical flat plate experiments, five runs were performed in air, with modified Grashof numbers ranging from 5.6×10^7 to 2.7×10^8. The experimental local Nusselt number results were generally within ±9% of the numerical results derived from a similarity solution to the problem. The uncertainties in the experimental results ranged from 9% to 13%. The repeatability of the experimental results was to within ±0.5%.

Five experimental runs of natural convection in a horizontal concentric annulus were undertaken in air, with Rayleigh numbers ranging from 3.0×10^4 to 9.9×10^4. The experimental results were compared to those of a control volume finite-difference simulation of the problem. The experimental Nusselt numbers on the surface of the inner cylinder were

within ±9% of the numerical results for $0^\circ < \theta < 150^\circ$. The agreement between the experimental and numerical results was not as good at the top of the inner cylinder ($\theta > 150^\circ$). The experimental uncertainties in the local Nusselt numbers were between 9% and 20%. The repeatability of the experimental results was ±6%.

SOMMAIRE

La présente thèse traite du développement et des essais relatifs à une technique, utilisant un film d'or, pour mesurer les coefficients de film locaux en convection naturelle.

La technique proposée a été conçue pour tenir compte du transfert de chaleur par conduction et par radiation car ces deux modes sont non-negligeables par rapport aux faibles taux de transfert de chaleur rencontrés en convection naturelle.

La présente technique de mesure à été évaluée en étudiant expérimentalement deux cas de convection naturelle bi-dimensionelle en régime permanent et laminaire. Ces résultats expérimentaux ont été comparés avec des résultats analytiques ou numériques obtenus pour ces mêmes cas.

Dans le premier cas, la convection naturelle le long d'une plaque verticale, située dans l'air, a été étudié. Cinq essais ont été effectués pour des nombres de Grashof modifiés variant de 5.6×10^7 jusqu'à 2.7×10^8. Les nombres de Nusselt trouvés expérimentalement étaient à ±9% près des mêmes nombres de Nusselt obtenus à partir d'une solution analytique utilisant la méthode des similitudes. L'incertitude sur les mesures expérimentales était de l'ordre de 9% à 13%. Les résultats d'une répétition des mêmes expériences concordent

avec les premiers à 0.5% près.

La deuxième expérience concerne l'étude de la convection naturelle dans l'air contenu entre deux cylindres concentriques. Pour cette expérience, cinq essais ont été éffectués pour des nombres de Rayleigh variant de 3.0×10^4 jusqu'à 9.9×10^4. Les nombres de Nusselt, mesurés expérimentalement sur la surface du cylindre interne pour des angles de 0 à 150 degrés, coïncidaient à ±9% près avec les résultats d'une simulation numérique basée sur la méthode des différences finies à volume de contrôle. Par contre, au sommet du cylindre interne l'accord entre les résultats expérimentaux et numériques n'est pas aussi bon. Pour ces essais, l'incertitude sur les mesures expérimentales était de l'ordre de 9% à 20%. Les résultats d'une répétition des mêmes expériences concordent avec les premiers à 6% près.

ACKNOWLEDGEMENTS

I am grateful and wish to thank my advisor, Professor B.R. Baliga, for his guidance and assistance throughout the course of this research. I would also like to express my appreciation to my colleagues, Perry Rose, Michel Bernier, Neil Hookey and Robert McBrien in the Heat Transfer Group for their advice and help in various phases of this investigation.

I would especially like to thank Mr. Arthur Clement, Mr. Jack Kelly and their respective staffs in the Machine Tool and Undergraduate Laboratories for providing technical skills and advice. The Machine Tool Laboratory staff, in particular, were extremely proficient in building equipment required for the experimental portion of this work.

I am grateful to the Department of Mechanical Engineering at McGill University and NSERC for providing financial support for this research. I would also like to acknowledge the McGill University Computing Centre for providing free computer time for the numerical portions of this thesis.

Finally, I would like to thank my wife, Jennifer, and my family for the support they have given me while I was at McGill University.

TABLE OF CONTENTS

PAGE

LIST OF FIGURES

PAGE

PAGE

PAGE

PAGE

LIST OF TABLES

PAGE

NOMENCLATURE

SYMBOL	DESCRIPTION
A	surface area
a, b	coefficients in Eq. (4-17)
C	coefficients
c_p	specific heat at constant pressure
D	diameter
ds	differential element of control surface ∂V
$F(\eta)$	velocity function defined in Eq. (3-15)
Gr	Grashof number
Gr^*	modified Grashof number
$\vec{g}$	acceleration of gravity
h	local convection heat transfer coefficient
I	electrical current
$\vec{J}$	total convection and diffusion flux of ϕ
k	thermal conductivity
L	length of flat plate; gap width of concentric cylinder
Nu	Nusselt number
$\vec{n}$	outward normal vector to ds
P	modified pressure defined in Eq. (4-7)
p	pressure
powlaw	exponent in Eq. (3-27)
Pr	Prandtl number
Q	local heat transfer rate
q	local heat flux
R	result

SYMBOL	DESCRIPTION
R''	electrical resistivity defined in Eq. (2-4)
Ra	Rayleigh number
r	radial coordinate
S	volumetric generation or source term for ϕ
s	electrode separation
T	temperature
TOL	tolerance
u, v	velocity components
V, ∂V	control volume, and surface of the control volume, respectively
V	voltage
w	gold-film sample width; uncertainty level
X	reference length
x, y	spatial coordinates
x	experimental measurement quantity

GREEK SYMBOLS

α	absorptivity; thermal diffusivity; under-relaxation parameter in Eq. (4-18)
β	thermal volumetric expansion coefficient
ψ	stream function defined in Eqs. (3-12) and (3-13)
ϕ	scalar quantity
ε	emissivity
λ	wavelength
η	similarity variable defined in Eq. (3-14)
μ	dynamic viscosity
ν	kinematic viscosity

SYMBOL	DESCRIPTION
ρ	mass density; reflectivity
θ	angular coordinate
$\theta(\eta)$	temperature function defined in Eq. (3-16)
σ	Stefan-Boltzmann constant
τ	transmissivity
Γ	diffusion coefficient of ϕ

SUBSCRIPTS

air	surrounding air
box	constant temperature box
c	cold
cnd	conduction
cnv	convection
D	diameter
e	electrical generation
f	film; fluid
h	hot
i	point on surface of interest; inner cylinder
L	gap width of concentric cylinder;
max	maximum value
n	neighbour point
o	outer cylinder
p	point of interest
rad	radiation
ref	reference

SYMBOL	DESCRIPTION
w	wall
λ	wavelength
∞	infinity

SUPERSCRIPTS

*	nondimensional quantity; estimated quantity
$\rightarrow$	vector quantity
$-$	average
m	iteration number

CHAPTER I

INTRODUCTION

1.1 AIMS AND MOTIVATION

Natural convection is an important mechanism of heat transfer in many engineering systems. Examples of the application of natural convection to solve problems include the cooling of electronic components, thermosyphons designed for emergency cooling of nuclear reactors, and the transfer of heat from residential electric heaters. This thesis is concerned with experimental measurements of local heat transfer coefficients in natural convection problems.

In a number of recent experimental investigations of ***forced*** convection and ***boiling*** heat transfer, local heat transfer measurements have been made using a gold-film technique [1-10]. The technique employs a commercially-available gold-coated plastic sheet as an electrical resistance heater. The gold-film heater is attached to the test section to be studied. When a current is passed through the heater, a nearly-constant heat flux is generated. By measuring temperatures at different locations on the gold-film surface, local heat transfer coefficients may be calculated at these points. The overall goal of this thesis is to adapt this gold-film technique for local measurements in ***natural*** convection problems, and to establish its capabilities and limitations by applying it to test problems.

The gold-film heater possesses a number of properties which make it particularly suitable for heat transfer studies. Firstly, the heater is

manufactured by vacuum-depositing a thin coating of gold on a polyester substrate. This process gives a reasonably uniform thickness of gold on the plastic sheet. Sheets having an electrical resistivity ranging from 3 to 26 Ω/sq. are currently manufactured, and the resistance is only slightly temperature dependent. Secondly, heat conduction along the gold-film heater may be neglected because the gold coating is only a few Angstroms thick. This heat conduction calculation is sometimes subject to large uncertainties when employing thicker metal heaters [9]. Thirdly, because the gold-film and polyester substrate is typically about 0.127 mm (0.005 in.) thick and quite flexible, it may be wrapped around objects with a radius of curvature as small as 19.05 mm (3/4 in.). Finally, the gold-film and polyester base is approximately 80% transparent to visible light. This enables the visualization of the temperature field by placing liquid crystal sheets beneath the gold-film heater. The gold-film heater also allows for flow visualization through the heated surface.

The gold-film technique has been used in various forced convection and boiling heat transfer studies to provide local heat transfer data. Oker and Merte [1] used a gold-film sheet as a surface heater and as a resistance thermometer simultaneously for nucleate boiling studies. Hippensteele et al. [2-4] have used a gold-film heater and liquid crystal composite to measure heat transfer coefficients on a gas turbine airfoil. Simonich and Moffat [5,6] studied heat transfer on a concavely-curved turbulent boundary layer with a gold-film heater/liquid crystal package. Baughn et al. [9] used the gold-film technique in conjunction with fine-gauge thermocouples to measure heat transfer in circular ducts with circumferentially varying heat flux [7], around an abrupt expansion in a

pipe [8], and around cylinders in crossflow [10].

In the aforementioned investigations [1-10], the rates of heat transfer by forced convection or boiling were large in comparison to the rates of heat transfer by conduction inside the test objects on which the heater was mounted and by radiation from the surface of the gold-film heater. Thus, the corrections for heat conduction and radiation were either neglected or amounted to a small fraction of the dominant heat transfer mechanism in these studies. Physically, this means that the nearly uniform ohmic heating in the gold-film manifested itself as an essentially constant heat flux for the forced convection or boiling heat transfer problem, without significant alterations by heat conduction or radiation.

In principle, the gold-film technique should be capable of accurately determining local heat transfer coefficients even when conduction and radiation heat transfer are of appreciable magnitude. The only complications are that heat conduction inside the test object must be computed to determine the actual heat flux distribution at the solid-fluid interface, and then to calculate the proportion of this modified heat flux that leaves the surface as radiation. In order to use such a technique successfully, however, the magnitude of the uncertainties in calculating the rates of conduction and radiation heat transfer must be much smaller than the rate of convection heat transfer that is being measured. The work presented in this thesis is an attempt to determine if the thin gold-film technique can be adapted to accurately measure local heat transfer in the presence of significant conduction and radiation heat transfer.

The main goals of this thesis can be summarized as follows:

(1) Develop a thin gold-film technique to enable the acquisition of local heat transfer data in natural convection problems;

(2) Determine local heat transfer coefficients, using numerical techniques to make corrections for conduction and radiation heat transfer; and

(3) Evaluate the performance of the proposed technique by using it to determine local heat transfer coefficients in two natural convection problems and to verify the results against those of an appropriate theoretical or numerical simulation of each problem.

The two heat transfer problems to be considered in this thesis are laminar natural convection along a vertical flat plate and laminar natural convection in a horizontal concentric annulus. The rates of convection heat transfer in these natural convection problems are quite small compared to those in previous forced convection or boiling experiments [1-10], which makes conduction and radiation heat transfer proportionately more significant. Both of these problems can be simulated quite accurately using numerical techniques.

This work is one part of a comprehensive experimental and numerical research effort, being undertaken in the Department of Mechanical Engineering at McGill University, with the goal of studying practical natural and forced convection problems. The aim of this research program

is to develop a capability to numerically predict fluid flow and heat transfer phenomena using control volume finite-difference and finite-element computer codes that have been extensively verified experimentally. In order to accomplish this goal, accurate local experimental heat transfer data is required for a variety of natural, forced and mixed convection problems. The objective of this thesis is to develop a technique capable of providing such local heat transfer data.

1.2 SYNOPSIS OF TECHNIQUES FOR DETERMINING LOCAL HEAT TRANSFER COEFFICIENTS

Numerous experimental techniques for determining local heat transfer coefficients have been presented in the published literature. A comprehensive survey of all of these investigations will not be attempted here. Much of the theory relevant to measurement techniques in heat transfer has been reviewed in a book edited by Eckert and Goldstein [11]. In particular, the chapters on "Thermocouple Thermometry", by Powell, "Optical Temperature Measurements", by Goldstein, "Transient Techniques for Determining Surface Heat Flux Rates", by Scott, and "Analogies to Heat Transfer Processes", by Eckert, are directly applicable to this study. The literature reviewed in this section is limited to those methods which can be used for taking local natural convection heat transfer measurements and to works which are relevant to the development of the technique used in this thesis. A brief discussion of the advantages and disadvantages of each technique is also included.

Most of the techniques used to measure local heat transfer coefficients

are based on three general methodologies in which: (i) the test surface is maintained at a constant temperature and local heat fluxes are measured; (ii) the analogy between heat and mass transfer is used to infer local heat transfer results by examining an equivalent mass transfer problem; or (iii) the test surface is maintained at a non-uniform temperature, often by attaching an ohmic heater to the surface, and local heat fluxes are calculated.

In techniques which maintain the test surface at a constant temperature, it is necessary to determine local surface heat fluxes. This objective has been accomplished by using heat flux gauges [12-16]; by employing a series of individually powered heating strips, which are adjusted to obtain a nearly-constant surface temperature [17]; and by measuring the temperature gradient in the fluid next to the wall using optical methods [18-22].

Heat flux gauges may be classified into two types [23]: (i) the thermal resistance type; and (ii) the calorimetric type. Thompson [12] has presented an excellent review of the theory of operation of various types of heat flux gauges.

The basic principle of the thermal resistance type of heat flux gauge is to create a one-dimensional heat conduction situation inside the gauge which is driven by the local heat flux at the test surface. An example is the Gardon heat flux gauge [13], which operates by setting up a temperature difference between the centre and the edge of a thin circular membrane. Newman et al. [14] used a modified version of this gauge to study

turbulence effects on heat transfer from a sphere. In their work, a heat flux gauge was accurately calibrated down to 600 W/m^2. Kraabel et al. [15] have designed an instrument capable of taking heat transfer measurements, of magnitude 400 W/m^2, within ±2% of the actual value.

In the calorimetric type of heat flux gauge, the local heat flux is obtained from an energy balance applied to the gauge. Heat is either supplied to or removed from the surface of the heat flux gauge in order to maintain isothermality of the test surface. The Peltier heat flux meter, developed by Shewan et al. [16], has been calibrated to within ±1% over the range of 15 $W/m^2 < q_{conv} < 550\ W/m^2$.

The principle disadvantage of most heat flux gauges is that one probe is required per measurement location. Secondly, the presence of heat flux gauges can distort the heat fluxes that they are attempting to measure. Thirdly, only average heat transfer coefficients over the surface area of the gauge can be determined.

In 1928, Bryant et al. [17] developed a method to measure forced convection heat transfer from the surface of an airfoil in a wind tunnel. Their work involved the application of a number of electric heating elements in the spanwise direction of the airfoil, with small gaps in between for electrical isolation. The power supplied to each heated strip was individually adjusted in order to obtain a nearly-uniform temperature everywhere on the test section surface, thereby minimizing conduction heat transfer inside the airfoil. Heat fluxes, averaged over the area of each element, were calculated by dividing the power supplied to each element by

its respective surface area. The main advantage of this method is that heat transfer coefficients can be obtained using a known, uniform temperature, boundary condition. However, electrical connections must be provided for each heater element and an electronic device to automatically control the power supplied to the heaters is required. It must be emphasized that the heat transfer coefficients are necessarily averaged over the area of each heater. Thus, some knowledge of the heat transfer situation is required beforehand so that the heated strips can be placed appropriately.

Optical techniques have been used to obtain the temperature distribution in a fluid next to a wall maintained at a constant temperature [18-22]. Local heat fluxes, which are proportional to the temperature gradient at the wall, may then be calculated. The most developed of the optical techniques are those that use the known dependence of the index of refraction of the working fluid on temperature. Hauf and Grigull [18] have presented a comprehensive review of three of these techniques, namely the shadowgraph, schlieren and interference methods. For natural convection experiments, interference methods are generally used due to the small fluid density gradients normally encountered. Eckert and Soehngen [19] made the first local heat transfer measurements in a horizontal annular geometry using an interference method. The same authors [20] took photographs of the flow fields next to a vertical flat plate and observed the transition to turbulence using a similar interference method. More recently, Kuehn and Goldstein [21,22] employed a Mach-Zehnder interferometer to study heat transfer between isothermal, concentric and eccentric cylinders.

The interferometer possesses a number of advantages and disadvantages for measuring natural convection heat transfer. The major benefit is that there is no device or probe inside the fluid to disturb the flow and temperature fields. Secondly, the entire field of interest can often be observed simultaneously. On the other hand, the interferometer integrates quantities over the length of the light beam, which limits the method to heat transfer problems which are essentially one- or two-dimensional in nature. Another limitation of the interferometer is that the media to be studied must be transparent to radiation. Finally, the analysis of photographs taken using any of the index of refraction-based methods is prone to large sources of error. Kuehn [22] reported that errors in reading the spacing of the fringes alone gave uncertainties of up to 13%, in regions of high heat fluxes, in his experiments.

The similarities between the physical mechanisms and the governing equations for heat and mass transfer in a constant property fluid suggests that heat transfer results may be inferred from a study of an analogous mass transfer experiment. This is the basis of using the napthalene sublimation and electrochemical techniques to obtain natural convection mass transfer data for studying the corresponding heat transfer problem. The natural convection motion in both of these techniques is driven by buoyancy forces which result from concentration-induced density differences. The two techniques will now be briefly discussed.

The napthalene sublimation technique involves the application of a uniform coating of napthalene to the surface being investigated. The boundary condition of constant mass concentration of napthalene vapour at

the test surface in the mass transfer problem corresponds to a constant temperature boundary condition for the analogous heat transfer experiment. When the experiment is performed, napthalene sublimates at different rates from point to point on the test surface. By measuring the napthalene profile on the test surface before and after the experiment has been performed, local mass transfer coefficients may be determined. This technique has been used to study forced convection in a one-row plate fin and tube heat exchanger [24], in an array of colinear interrupted plates [25], at the surface of a rotating disk [26], and natural convection adjacent to horizontal plates [27].

The major advantage in using a sublimation mass transfer system, especially for natural convection problems, is that heat conduction and radiation losses are avoided. However, there are a number of details which must be considered in order to obtain accurate results. Cur [25] discusses the casting and machining processes used to yield a uniform coating of napthalene on his flat plates. Accurate machining of curved surfaces is much more difficult. Secondly, extraneous sublimation prior to and after the experiment must be minimized. This means that the experiment must be designed for rapid assembly and disassembly. Finally, the technique is not suited for studying phenomena which take a long time to reach steady-state conditions because extraneous sublimation during the transient period cannot be avoided.

Another technique used to take local mass transfer measurements from a surface in a liquid environment is based on electrochemical reactions. In this method, the test surface is made a cathode for an electrochemical

reaction. When a voltage difference is applied between the test surface and the tank containing the electrolytic solution, ions will plate out on the cathode. These ion concentration gradients induce the density differences which drive the natural convection motion.

An excellent review article discussing the theory relevant to the electrochemical method as well as its application to both free and forced convection mass transfer measurements has been presented by Mizushina [28]. The major advantage of this method, in addition to avoiding large heat conduction and radiation effects, is that highly local measurements of mass transfer can be made. Lloyd et al. [29] developed a miniature probe to take local mass transfer measurements at a spacing of 0.05 mm. The probe was used to take both streamwise and spanwise measurements of laminar, transition and turbulent natural convection adjacent to inclined and vertical flat surfaces [30].

The third methodology that has been employed to measure local heat transfer coefficients involves maintaining the test surface at a non-uniform temperature, and then estimating the local heat fluxes at the solid-fluid interface.

Ohmic heating is frequently used to provide a nearly-constant heat flux boundary condition at a test surface. The term nearly-constant is employed because corrections to the heat flux are generally required to account for: (i) conduction heat transfer inside the walls of the test object; (ii) radiation heat transfer from the walls; and (iii) non-uniformities in the resistance of the heater due to thickness and temperature variations.

Early heat transfer measurements using ohmic heating were obtained by passing current through a thick metal wall. In 1930, Eagle and Ferguson [31] studied heat transfer from a tube to water by heating brass tubes. In their work, the calculation of local power generation included corrections to account for non-uniformities in tube thickness and in electrical resistance. External heat loss from the outside of the pipe to ambient was also estimated. Longitudinal heat conduction was negligible in their work. Ede et al. [32] studied flow through a pipe experiencing abrupt convergence and divergence. Heat was supplied by passing current through aluminum brass pipes having diameters of 25.4 mm and 50.8 mm (1 in. and 2 in.), with wall thicknesses of 7.09 mm and 4.32 mm (0.279 in. and 0.170 in.), respectively. Temperatures were measured on the outside of the pipe using copper-constantan thermocouples, and an energy balance was developed to estimate the temperature gradient in the radial direction of the pipe. For the runs with high surface heat flux, they stated that the results are subject to "a significant degree of uncertainty" from this estimation of the temperature difference through the pipe wall. Krall and Sparrow [33] also performed experiments in a circular pipe made of stainless steel. Power was supplied by passing a.c. current through the tube, which had an inside diameter of 19.10 mm (0.752 in.) and a wall thickness of 1.59 mm (1/16 in.). Losses to ambient and heat conduction along the steel tube always totalled less than 3.5% of the convection heat transfer rate.

Giedt [34] was one of the first to attach a thin metal foil to a test surface made of low thermal conductivity material. In his experiments, a nichrome ribbon, with dimensions of 25.4 mm (1 in.) width and 0.051 mm

(0.002 in.) thickness, was helically wound around a lucite cylinder. Measurements of local heat transfer were made around the cylinder, which was oriented in a normal direction to the air stream. Heat conduction along the nichrome ribbon and radiation from the surface of the heater was considered. However, the heat flux redistribution due to conduction inside the lucite cylinder was not calculated. Oosthuizen [35] has shown that substantial errors in determining local heat transfer coefficients have been made in some previous heat transfer studies due to neglecting internal heat conduction, when using thin-film heaters mounted on circular cylinders made of low thermal conductivity materials.

A polyester sheet with a vacuum-deposited gold coating has been used as a heater in a number of recent investigations [1-10]. The electrical resistance of a sample of the gold-film heater typically varies by less than ±10% from the mean value throughout [2,5,9]. In addition, the heater is approximately 80% transparent to light. This permits flow visualization through the heater and the placement of a liquid crystal sheet beneath the heater for both qualitative and quantitative measurements of temperature.

The flexible nature of thin metallic, and gold-film, heaters allows them to be attached to almost any two-dimensional surface. In addition, surfaces which are moderately three-dimensional in nature can also be handled by using a number of heaters [5].

Liquid crystals have been used in conjunction with gold-film heaters to take local heat transfer measurements. Information and theory about the various types of liquid crystals may be obtained from an article by

Fergason [36]. Cholesteric liquid crystals change colours rapidly over a small range of temperature. These colour changes are repeatable for a given liquid crystal sheet and have been calibrated to give quantitative temperature data. Simonich and Moffat [5] calibrated liquid crystal sheets in a constant-temperature water bath which had transparent sides. Using a mercury-vapour light for illumination, particular colours were calibrated to $\pm 0.25^{\circ}C$. The main advantage of employing liquid crystals for temperature measurement is that one obtains information about the entire field within the specified temperature range of the liquid crystals. Simonich and Moffat [6] state that the repeatability of a particular data point was within a 3% standard deviation, with one observer interpreting colour. A second observer, with an agreement of objective, repeated the data point with a 6% standard deviation. Thus, it appears that an imaging system is required to obtain more accurate and repeatable interpretations of colour.

Hippensteele et al. [2] were among the first to publish local convection heat transfer results using a gold-film heater/liquid crystal composite. Qualitative photographs of impingement cooling of a single jet on a flat plate, heat transfer at the endwall of a cascade, and film injection from a cylinder in crossflow were taken. Simonich and Moffat [5] calibrated liquid crystal sheets in order to obtain quantitative local heat transfer coefficients in both natural and forced convection flows. The same authors [6] also obtained local heat transfer measurements on a concavely-curved turbulent boundary layer. Hippensteele et al. [3] have taken local heat transfer measurements on a turbine blade airfoil using heater element/liquid crystal packages and extended their work [4] to

include turbulence and surface roughness effects. Baughn et al. [7-10] attached fine-gauge thermocouples to the back of a gold-film heater to take local forced convection heat transfer measurements. A detailed discussion of the technique and the correction factors employed are given for a number of heat transfer studies [9].

The primary advantages of employing a thin-film technique for taking local heat transfer measurements are: (i) the technique can be implemented relatively easily and quickly; (ii) the accuracy of the method is comparable or better than many other available techniques; and (iii) the equipment and instrumentation required to use the technique are available commercially, and are relatively inexpensive to purchase.

The gold-film technique has only been employed in situations where the rates of conduction and radiation heat transfer at the test surface are relatively small [1-10]. In this thesis, an attempt has been made to use complementary computer models to accurately calculate the heat flux redistribution due to conduction and radiation in natural convection problems, where this redistribution is important.

1.3 SYNOPSIS OF INVESTIGATIONS RELATED TO THE TEST PROBLEMS

1.3.1 Laminar Natural Convection along a Vertical Flat Plate

A number of experimental investigations have been published on natural convection heat transfer along a vertical flat plate. An excellent survey paper on this problem has been presented by Ede [37].

One of the earliest studies was that of Rich [38], who obtained local heat transfer measurements for a plate at inclinations up to 40° from the vertical, using a Mach-Zehnder interferometer. The experiments were performed in air, with a wall boundary condition that was between that of constant heat flux and constant temperature. Measurements were limited to the laminar regime. Kierkus [39] extended this work by taking local velocity and temperature measurements over a range of Grashof numbers, from 10^2 to 4×10^7, with the plate oriented vertically and inclined 45° to the vertical position. He also presented a perturbation analysis for the problem. Comparisons between the calculated results and the experimental data were quite good. Cheesewright [40] measured local temperature and velocity profiles in the turbulent regime. However, data was also taken in the laminar regime, with Grashof numbers ranging from 10^4 to 10^9, to validate the measurement technique. Good agreement was found between his laminar data and that of Ostrach's [41] theoretical solution.

Vliet and Liu [42] conducted experiments involving both laminar and turbulent natural convection along a vertical plate with a constant heat flux boundary condition. For most trials, water was the working fluid, although some of the data was taken in air. Laminar and turbulent local heat transfer correlations for vertical surfaces with a constant heat flux boundary condition were calculated using his data and previous experimental data by Dotson [43]. The transition region between laminar and turbulent natural convection was also studied. Fujii and Imura [44] took data in the laminar range with a variety of plate inclination angles, including the vertical position. The boundary condition for their experiments was

between that of constant heat flux and constant temperature. Fussey and Warneford [45] present transition criteria for an inclined flat plate with constant heat flux as well as heat transfer correlations for laminar and turbulent flow.

Sparrow and Carlson [46] presented results of an experiment designed to investigate the heat flux uniformity at the surface of electrically-heated metallic foils. They conducted natural convection experiments on a vertical flat plate with a constant heat flux boundary condition, and compared their results to the similarity solution to the problem, which was determined by Sparrow and Gregg [47]. The agreement between experiments and theory provided evidence that heat is dissipated uniformly by thin, electrically-heated, metallic heaters. This result is in direct contrast to the results of Tarasuk and Castle [48], who determined that significant nonuniformities in heat flux generation existed at the surface of a 0.025 mm (0.001 in.) 302 precision stainless steel heater.

Theoretical solutions to the governing equations of natural convection along a vertical flat plate have been attempted by: (i) solution of the ordinary differential equations derived from a similarity transformation of the governing equations; and (ii) solving the integral form of the governing equations using assumed velocity and temperature profiles.

Pohlhausen, in collaboration with Schmidt and Beckmann [49], derived simplified equations governing free convection along an isothermal plate by applying Prandtl's boundary layer approximations and assuming that the Boussinesq approximation is valid. The resulting equations were

transformed using a similarity analysis to yield two coupled ordinary differential equations. A solution was given for Pr = 0.733 . Computer solutions to these equations were later obtained by Ostrach [41] for a range of Prandtl Numbers. In addition, Ostrach analyzed the problem in a more formal manner, without invoking the Boussinesq approximation. Sparrow and Gregg [47] presented a similarity transformation for a constant heat flux boundary condition. They also provided comparisons between the results for constant heat flux and constant plate temperature.

An approximate solution to the integral form of the momentum equations was obtained by Squire [50]. Velocity and temperature were prescribed as a function of the perpendicular distance from the plate surface and the boundary layer thickness. When these expressions are substituted into the governing equations, and the integrations are performed, the boundary layer thickness may be obtained. This can be used to calculate the local heat transfer on the plate. The procedure to be followed has been outlined by Eckert [51]. Improvements and modifications to this approach were reviewed by Ede [37] and also by Gebhart [52].

1.3.2 Laminar Natural Convection in a Horizontal Concentric Annulus

Ostrach [53] has presented a review paper dealing with natural convection driven flow inside rectangular cavities and horizontal circular cylinders. Many of the phenomena discussed in this paper are also relevant to natural convection heat transfer in a horizontal concentric annulus.

One of the first published results of natural convection between horizontal concentric cylinders were those of Beckmann [54]. He obtained average heat transfer data for a number of diameter ratios, D_o/D_i, ranging from 1.2 to 8.1, and for Grashof numbers ranging from 10^3 to 10^7, using air, hydrogen, and carbon dioxide as the working fluid. Kraussold [55] extended this work by performing experiments in water, transformer oil, and machine oil, with diameter ratios between 1.2 and 3.0. He used the same apparatus as Beckmann, but with guard heaters installed to minimize the large axial heat conduction errors in Beckmann's work. Liu et al. [56] obtained flow patterns, temperature profiles and overall heat transfer correlations for air, water, and silicone. Results of their tests were significantly different from those of Beckmann and Kraussold in many cases. Their work also contained the first report of unsteady convective flows at certain combinations of Grashof numbers and diameter ratios.

Grigull and Hauf [57] used a Mach-Zehnder interferometer to obtain local heat transfer information over the range of Grashof numbers, Gr_L, from $320 < Gr_L < 7.2 \times 10^5$. Nine gap width/inner cylinder diameter ratios, L/D_i, were considered in their work. Flow visualization, using cigarette smoke, was also undertaken. Lis [58] acquired average heat transfer data in both the laminar and turbulent regimes. A series of runs with helical and axial spacers inside the annuli were also performed, but only small differences from the unobstructed case were observed. Bishop et al. [59] further studied oscillatory flow inside horizontal annuli, and a prediction equation is given for the start of oscillating flow in terms of two non-dimensional parameters, namely L/D_i and Gr_L. Powe et al. [60] categorized the flow patterns in horizontal concentric annuli. Regions of two-

dimensional stable flow, two-dimensional oscillatory flow, two-dimensional multicellular flow, and three-dimensional spiral flow were shown to exist.

Kuehn and Goldstein [21] have presented a most comprehensive series of experiments on natural convection heat transfer between concentric cylinders. Results were obtained in air and water at atmospheric pressure over a range of Rayleigh numbers: $2 \times 10^4 < Ra_L < 1 \times 10^6$. Additional experiments were conducted in a pressurized chamber using nitrogen [22] for Rayleigh numbers of 2×10^2 to 8×10^7. The effect of inner cylinder eccentricity was also considered [61]. A complementary numerical study was performed to study the influence of Prandtl number and diameter ratio on heat transfer [62].

Hessami et al. [63] conducted tests in a horizontal annulus with a radii ratio of 11.4. Experimental data using air, mercury and glycerin as the working fluid are reported in the range of $0.023 < Pr < 10000$ and $0.03 < Gr_{D_i} < 3 \times 10^6$. Numerical solutions were also obtained using both constant and variable property formulations. For air, no significant difference was observed using the two aforementioned formulations.

Natural convection experiments in a horizontal annulus, with a non-isothermal inner cylinder boundary condition, were conducted by van de Sande and Hamer [64]. The inner cylinders were 50.8 mm (2 in.) and 127.0 mm (5 in.) stainless steel tubes, which acted as resistance heaters. The 298.5 mm (11 3/4 in.) outer cylinder was cooled by a waterjacket. The inner cylinder was placed above, below, sideways, and in the concentric position. No mention is made of the degree of heat transfer in the

circumferential direction of the inner cylinder.

1.4 SURVEY OF THE THESIS

There are a total of five chapters in this thesis. In this chapter, the aims of this work and a synopsis of relevant investigations have already been presented. The organization of the remaining four chapters will now be summarized.

In Chapter II, a detailed description of the thin-film technique for measuring local heat transfer coefficients will be presented. The two problems studied, namely, laminar natural convection along a vertical flat plate and laminar natural convection inside a horizontal annulus, are discussed in Chapters III and IV, respectively. The makeup of these two chapters is similar. Firstly, the problem is concisely stated. This is followed by a discussion of the numerical simulation of the problem. Then, construction details of the apparatus and the experimental test procedure are discussed. Finally, a comparison between the experimental results and the numerical simulation are presented. In Chapter V, the contributions of this work are summarized, and improvements and a number of extensions are recommended.

CHAPTER II

GOLD-FILM TECHNIQUE DEVELOPMENT AND CALIBRATION

2.1 DESCRIPTION OF TECHNIQUE

In this section, an overview of the thin-film technique used in this thesis to obtain local natural convection heat transfer measurements is presented.

The technique is based on the ability of a thin-film heater to generate a nearly-constant heat flux. The thin-film heater is attached to the surface of a test object over which the local natural convection heat transfer measurements are to be made. When a voltage is applied across the thin-film heater of uniform electrical resistivity, a uniform current flows through it. The resultant ohmic heating and the local rate of heat transfer from the surface of the heater jointly establish the local heater temperature. Natural convection heat transfer coefficients at the interface between the heater and the fluid may be calculated by determining the convection heat flux and by measuring the surface temperature of the heater at points of interest.

In order to determine the convection heat transfer at the interface between the thin-film heater and the fluid, two other modes of heat transfer must be considered. They are: (i) heat conduction inside the test object that the heater is attached to; and (ii) radiation heat transfer from the surface of the thin-film heater to its surroundings.

If the temperature distribution along all boundaries of a closed region encompassing the test object and the thermal conductivity of all materials inside this region are known, then heat conduction inside the test object may be computed using finite-difference or finite-element methods. This experimental-numerical determination of heat conduction inside the test object requires very accurate measurements of local heater-surface temperature and relatively large variations in this temperature distribution to be successful. The achievement of these requirements in this work was facilitated by the use of carefully calibrated thermocouples and associated instrumentation, and the use of relatively low thermal conductivity materials in the construction of the test object. Plexiglas was used to construct the test object in these experiments, and air was the working fluid.

Radiation heat transfer calculations require the knowledge of the temperature and radiation properties of the heater and all other materials which the heater views. In order to simplify these radiation calculations and enhance the accuracy of the results, it is advantageous to employ materials which radiate essentially as blackbodies or graybodies, whenever possible.

In mathematical terms, and with reference to Fig. 1, an energy balance applied to a point of interest, i, on the surface of a thin-film heater can be expressed as follows:

$$q_{cnv_i} = q_{e_i} - q_{rad_i} - q_{cnd_i} \qquad (2\text{-}1)$$

where q_{cnv_i} is the convection heat flux leaving the heater surface, q_{e_i} is

the local heat flux generated by electrical resistance heating, q_{cnd_i} is the net heat flux leaving the heater by conduction within the test object, and q_{rad_i} is the net heat flux leaving the heater surface by radiation. The convection heat transfer coefficient at point i is defined as:

$$h_i = \left(\frac{q_{cnv_i}}{T_i - T_{ref}} \right) \tag{2-2}$$

and the Nusselt number, or non-dimensional heat transfer coefficient, is defined by the following equation:

$$Nu_i = \frac{h_i \, X_{ref}}{k_f} = \left(\frac{q_{cnv_i}}{(T_i - T_{ref})} \right) \left(\frac{X_{ref}}{k_f} \right) \tag{2-3}$$

where X_{ref} and T_{ref} are an appropriate reference length and temperature, respectively, and k_f is the thermal conductivity of the fluid.

A gold-film heater was used in this work to generate a nearly-constant heat flux. The assumption of a nearly-constant heat flux makes it possible to prescribe an average value for q_{e_i} at all points. Thus, the subscript i will now be dropped from this term. Local heater temperatures were measured using thermocouples which were attached to the back of the heater, at the interface between the heater and the test object. Strictly speaking, heater temperatures at the heater-fluid interface are required to calculate the local Nusselt numbers. A one-dimensional heat conduction analysis on the gold-film heater, however, indicated that the maximum temperature difference across the heater was never more than 0.04°C for the heat fluxes encountered in this work. As will be discussed later in this chapter, the uncertainty in the calibration of the thermocouples is greater than this value. Therefore, the temperatures measured at the back of the gold-film heater were used to calculate local Nusselt numbers.

2.2 SUPPORTING EQUIPMENT AND INSTRUMENTATION

2.2.1 Gold-Film Heater

The gold-film heater employed in this work was manufactured by the Intrex Products Division of Sierracin Corporation. The product, called Intrex G, is fabricated by vacuum-deposition of a thin coating of gold onto a polyester substrate. The gold-film is protected from abrasion by an overcoating of a proprietary ceramic material called Fastex. According to the manufacturer, the gold-film is stable to about 90°C at the coating interface.

Intrex G can be purchased in a variety of gold-film and substrate thicknesses. Some of the manufacturer's specifications for the gold-film used in this study (Film Type 28) are:

(1) The electrical resistivity is 16 Ω/sq. ± 20%;

(2) The total thickness of the substrate and gold-film coating is 0.127 mm (0.005 in.); and

(3) The visible light transmittance is 80% ± 10%.

Standard web dimensions are 914.4 mm x 548.6 m (36 in. x 1800 ft), but the film used in this work was taken from a sample roll with dimensions of 25.4 mm x 15.2 m (12 in. x 50 ft).

Gold-film samples were always handled using clean surgical gloves in this work to avoid making smudge marks and fingerprints on the surface of the gold-film.

The gold-film heater was attached to the surface of plexiglas test objects using a double-sided adhesive (3M Canada Inc., Scotch Brand Tape No. Y-9473). This tape is sold in 25.4 mm (1 in.) wide rolls. The thickness of the tape is 0.254 mm (0.010 in.) and it can withstand temperatures of 149°C over long periods of time. Its adherence to tearing on steel (ASTM D-1000) is 120 N/mm (110 oz/in.). A number of different double-sided tapes were tested in the early stages of this work, but this product had better adherence to plexiglas than any of the other tapes sampled.

The voltage across the gold-film heater was supplied by a d.c. power supply (Hewlett Packard (Canada) Ltd., Model 6294A). This unit is capable of supplying up to 60 W of power. However, the voltage and current ranges are restricted to 0 to 60 V, and 0 to 1 A, respectively.

2.2.2 Gold-Film Cutter

One of the first tasks accomplished in the development of the gold-film technique was the design and construction of an apparatus for cutting the gold-film heater. Some of the considerations which went into the design of the cutter were:

(1) The cutter must be capable of making parallel cuts of 609.6 mm (2 ft) length to within a tolerance of approximately ±0.0254 mm (0.001 in.). This requirement is needed to enable the gold-film to be wrapped around cylindrical objects (25.4 mm < D_i < 194 mm) with a small gap (<0.127 mm) where the ends meet.

(2) The cutter must be able to easily cut through composites of gold-film heater, protective tape, and double-sided adhesive tape.

(3) The heater must lie on a flat, dust-free, surface when it is being cut, in order to avoid scratching the gold coating.

The final design of the gold-film cutting apparatus is shown in Fig. 2. The cutting surface is a 711.2 mm x 711.2 mm x 12.7 mm (28 in. x 28 in. x 1/2 in.) glass plate. The glass plate, which sits on a large table with a corkboard surface, is covered with a sheet of cardboard (0.4 mm thick) to prevent scratching the glass with the cutting knife. The sheet of cardboard is also partially cut when the heater is cut to size. This allows for a reasonable tolerance in adjusting the depth of cut of the knife, and permits the gold-film to be cut cleanly.

Each cutter is designed to slide along a pair of steel rails. The cold-finished square steel rails, with dimensions of 25.4 mm x 25.4 mm x 787.4 mm (1 in. x 1 in. x 31 in.), were precision ground on three sides to obtain a smooth finish. The rails were then oiled to prevent corrosion and provide lubrication for the cutter. The rails are bolted to brass supports which sit on the corkboard, as shown in Fig. 2. The brass supports were

machined so that the rails are separated by 25.4 mm (1.000 in.) and situated 2 to 3 mm above the cutting surface. Set screws were provided on the brass supports to hold the rails in place relative to the glass cutting table.

Each cutter consists of two "T" sections and a knife blade holder. The brass "T" sections were machined so that the bottom of the "T" would slide between the steel rails without play (clearance fit). The two "T" sections are separated by a 76.2 mm (3 in.) long brass piece. A commercial knife blade (Stanley Canada Inc., Part No. 1992) is held firmly in place against the brass middle section by a piece of steel which is screwed to the brass. A closeup of one of the cutting knives is shown in Fig. 3.

2.2.3 Data-Acquisition Equipment

A microprocessor-based data acquisition unit (Hewlett-Packard, Model 3497A) was used to take thermocouple voltage readings and electrical resistance measurements. The unit may be seen in Fig. 4. The unit is equipped with a 5 1/2 digit voltmeter (1 μV resolution) and a programmable current source. The voltmeter has an automatic zeroing feature. The accuracy of a voltage reading in the 0.1 volt range is ±0.007% of reading + 3 μV, if the voltmeter is maintained at 23°C ± 5°C.

Thermocouple voltage measurements were taken using three relay multiplexer assemblies with internal temperature compensation (Hewlett-Packard, Model 44422A). Each assembly contains 20 measurement channels on a special isothermal connector block, for a total system capacity of 60

channels. The assemblies were configured for hardware compensation. Reference junction compensation accuracy is quoted to be ±1°C.

The data acquisition unit was also outfitted with a 20 channel relay multiplexer assembly (Hewlett-Packard, Model 44421A). This assembly was used in conjunction with the programmable current source to take 4-wire resistance measurements. The current source, when set to a current of 0.001 A, is accurate to ±250 nA.

The data acquisition unit was controlled by a microcomputer (Hewlett-Packard, Model 86B). Software for this controller was written in the BASIC computer language, and was developed and tested as a part of this project. Data was stored on 3 1/2 inch diskettes driven by a disk drive unit (Hewlett-Packard, Model 9121). Hardcopies of results were obtained using a dot-matrix printer (Epson Canada Ltd., Model RX-80).

The electrical power supplied to the gold-film heaters was calculated from measurements of voltage and current. Voltage measurements were taken with the aforementioned digital voltmeter. As was discussed in Chapter I, two sets of experiments were undertaken. For the vertical flat plate experiment, current measurements were taken using a digital multimeter (Keithley, Model 197 Autoranging DMM). In the 2000 mA range, the unit has a resolution of 10 μA. The accuracy of this unit operating between 23°C ± 5°C is ±0.2% of reading + 15 counts. For the horizontal concentric annulus experiment, current measurements were made with another digital multimeter (Hewlett-Packard, Model 3478A). The resolution of this unit is 10 μA when using the 3000 mA range, and its accuracy, with autozero on, is

±0.17% of reading + 6 counts.

2.2.4 Temperature Measurement

All quantitative temperature measurements in this work were obtained using chromel-constantan thermocouples made of 30-gauge wires, and insulated with teflon (Omega Engineering Inc., TT-E-30). The procedure used to fabricate the thermocouples was as follows:

(1) About 10 mm of insulation was removed from one end of the wires, using an electrically-heated wire stripper (Teledyne Kinetics, Model TC-1).

(2) The last 5 mm of the chromel and constantan wires were twisted tightly together using two pairs of pliers.

(3) The ends of the twisted wires were cut, leaving just enough wire at the end to make a bead with a thermocouple welder.

(4) The wires were welded together. A variable-current thermocouple welder (Bel-Art Products, Cat. No. 15116) was purchased for this purpose. A wire holder, capable of pivoting in two dimensions, was fabricated from steel to eliminate human errors and ensure repeatable positioning of the wires during the welding process. The thermocouple welder and wire holder may be seen in Fig. 5.

(5) The wires were glued apart above the bead after welding with an electrically-insulating glue (Lepage Ltd., two-part epoxy resin and

hardener) to ensure that they could never make contact.

In the natural convection problems performed in this thesis, the temperature variations over the surface of the gold-film heater were expected to be as little as 2°C for some runs. Therefore, standard calibration coefficients for chromel-constantan thermocouples [65], which have an accuracy of approximately ±0.5°C, could not be used. All thermocouples were calibrated individually against a quartz probe thermometer in order to achieve an accuracy of at least 0.1°C in the temperature measurements.

A round copper block was constructed to keep all of the thermocouple beads at the same temperature during calibration. The copper block, with thermocouple wires and the quartz probe inserted into the drilled holes, is illustrated in Fig. 6. The dimensions of the copper block are 57.2 mm (2 1/4 in.) diameter x 38.1 mm (1 1/2 in.) thickness. The thermocouple wires are inserted into 48 holes of 2.4 mm (3/32 in.) diameter, drilled into the copper block to a depth of 19.1 mm (3/4 in.). At the centre of the piece, a hole was drilled to fit a quartz thermometer probe.

The reference temperatures for the calibrations were obtained using a digital thermometer (Hewlett-Packard, Model 2804A) with an individually calibrated quartz probe (Hewlett-Packard, Model 18111A). The unit was operated in the "medium resolution" mode, which is 0.001°C. The accuracy of the quartz thermometer over the operating range of -50°C to 150°C is ±0.04°C. The factory calibration of the quartz thermometer was recently verified at the National Research Council [66], against a standard platinum

resistance thermometer.

The round copper block, containing the quartz probe and the thermocouple beads, was placed in a refrigerated water bath and circulator (Haake, Model F3-C). The water bath, quartz thermometer and copper block are shown in Fig. 7. The water bath temperature could be set using thumb-wheel dials with 0.1°C resolution. The specified temperature control accuracy of this unit is ±0.02°C over the operating range of -20°C to 150°C. The actual temperature fluctuations observed during a calibration were always less than ±0.003°C.

2.3 TECHNIQUE DEVELOPMENT AND CALIBRATION

2.3.1 Electrode Attachment

The development of an appropriate procedure for attaching electrodes to the gold-film was one of the most challenging parts of this research project. A brief summary of the requirements of the electrode design, major difficulties encountered in initial designs, and the final procedure employed for attaching electrodes to the gold-film are discussed in this section.

The four main requirements of the electrode design are:

(1) Excellent electrical contact with the gold-film along the length of the electrode is needed;

(2) The electrodes must have negligible electrical resistance in comparison to the resistance of the gold-film heater;

(3) The gold-film must not be damaged while attaching the electrodes; and

(4) The electrodes must be attached to the gold-film after it has been mounted on the surface of the test object.

Electrical contact with the gold-film was difficult to achieve due to the small thickness of the gold-film and the unknown composition of its protective ceramic overcoating. In preliminary tests, a two-component electrically conductive epoxy resin containing copper particles (Acheson Colloids Company, Electrodag 5620A/B) was sandwiched between a sample of gold-film and a square copper bar on a flat surface. The electrical resistance of the bonded region turned out to be significant with this design, and this resistance kept varying with time. During the first few hours after making electrodes for a sample of gold-film, the total resistance of the electrodes and gold-film decreased. Afterwards, the resistance slowly increased with time. It is believed that the copper epoxy resin never did cure properly in the regions that were not exposed to air. Other plausible explanations are that the resin reacted with either the gold-film or its protective overcoating, or the bond between the epoxy and the gold-film deteriorated progressively with time.

It was decided, after this initial experience, that the electrodes should be constructed in two pieces. The function of the first piece would solely be to provide electrical contact with the gold-film. The second

piece would have the dual purpose of protecting the electrical contact with the gold-film and providing the required power connections.

A method similar to that employed by Baughn [9] was found to provide a dependable connection to the gold-film heater. Firstly, a stripe of silver-loaded paint (Sunshine Scientific Instruments, Part No. C-24) was painted on the gold-film, in the desired position of the electrode. After the silver-loaded paint had been allowed to cure for at least 24 hours, a copper foil with adhesive backing (3M, Scotch Brand Copper Tape) was attached to it. An aluminum foil with adhesive backing (Mactac Canada Ltd., Tape No. DAA02030), which had a slightly higher resistivity than the copper tape, was used instead of the copper tape for some of the measurements of electrical resistance uniformity. The upper surface of the copper foil and a small adjacent area of the silver paint stripe underneath were painted over with the silver-loaded paint to guarantee good electrical contact. A copper bar, containing screws for attaching the power leads, was bolted over the copper foil and silver-loaded paint to ensure an equipotential electrode and to protect the bonded regions.

The final procedure employed for attaching electrodes to the gold-film is summarized below:

(1) The gold-film was covered with a removable transparent tape (3M, Scotch Brand Magic Plus) for protection, leaving 20 mm wide parallel strips uncovered where the electrodes were to be located.

(2) A thin layer of the silver-loaded paint was applied to the uncovered

regions of the gold-film. The paint was allowed to cure for at least 24 hours.

(3) A 15 mm wide piece of copper tape was applied to the central region of the painted region, leaving a 2 mm stripe of silver-loaded paint exposed on both sides.

(4) A second layer of silver-loaded paint was then applied over the exposed original layer of paint and the upper surface of the copper tape to ensure good electrical contact.

(5) A copper bar, containing the power lead connections, was then bolted over the entire electrode. To ensure good electrical contact, another layer of silver-loaded paint was applied to the corner between the copper bar and the copper tape.

(6) The protective tape was removed from the gold-film heater.

2.3.2 Uniformity of Electrical Resistance of Gold-Film Samples

A brief summary of previously published literature dealing with measurements of the uniformity of electrical resistance of gold-film heaters is presented first in this section. Then, the procedure followed to ascertain the uniformity of the electrical resistance of the gold-film roll used in this work is discussed.

Hippensteele et al. [2] successfully measured the uniformity of light transmission through a sample of the gold-film using a scanning microdensitometer. Maps of isodensity contours of the vapour-deposited gold were produced. This work showed that the largest density gradients were located near the edges of a roll of gold-film. A second technique was employed to determine the minimum and maximum heat transfer coefficients on a horizontal flat plate using a liquid crystal/gold-film composite. A liquid crystal sheet, which was calibrated for one particular colour in a water bath, was used to sense temperature. When power was supplied to this gold-film heater, nonuniformities in the liquid crystal colour were primarily due to variations in the heat flux caused by nonuniformities in the electrical resistance of the gold-film. The power was adjusted to determine the range of power levels needed to produce a certain colour on the liquid crystal sheet over a specified area of the film. The maximum variation in the local heat flux was determined to be ±8% about the mean.

Simonich and Moffatt [5] clamped two ultrasensitive heat flux gauges over a small area on both sides of a sample of gold-film. The gauges were connected in series to measure the total heat release at a location. Traversing a grid of 80 locations on the gold-film, they determined that the absolute difference between the known power input and the measured power output was always within 7%. On average, samples showed a ±10% variation in local heat flux generation.

Baughn et al. [9] measured the electrical resistance of narrow strips of Intrex gold-film. Their results showed that the resistance varied by

only ±4 to 5% from a mean value throughout the central 40% of an 860.0 mm wide roll. Resistance was found to increase near the edges of the film.

Because of the differences in the results of the aforementioned investigations, and due to the fact that the properties of the gold-film could vary from one roll to another, measurements of the uniformity of the electrical resistance of the gold-film were undertaken in this research.

A 203.2 mm (8 in.) length of gold-film was cut from the 304.8 mm (12 in.) wide sample roll and mounted on cardboard using double-sided adhesive tape. The gold film was cut into 12 strips of 25.4 mm (1 in.) width by 203.2 mm length. On each strip, 5 separate resistance measurements were made of 25.4 mm (1 in.) square sections using a small apparatus constructed from plexiglas. The apparatus is shown in Fig. 8.

The important details of the plexiglas apparatus for measuring the electrical resistance of the gold-film strips are as follows. The plexiglas was milled on top to provide a slot for a gold-film sample to fit, and to provide guides for constructing the electrodes. This guaranteed that the electrodes at each measurement location would be separated by exactly 25.4 mm (1 in.). The electrodes were constructed using the procedure described in Section 2.3.1. Holes were drilled and tapped into the plexiglas for bolting the copper bars containing the power leads to the electrode. The width of each strip of gold-film was nominally 25.4 mm (1 in.). Exact measurements of the width of the gold-film strips were made with a 10x magnification profile projector (Nikon, Model V-16) to an accuracy of ±0.0254 mm (0.001 in.).

The resistance of each 25.4 mm square piece of gold-film was measured using a 4-wire resistance technique. The electrical resistivity, R'', of a sample of the gold film is calculated as follows:

$$R'' = \left[\frac{V}{I} \right] \left[\frac{w}{s} \right] \qquad (2\text{-}4)$$

where V is the voltage difference, I is the electrical current, w is the width of the gold-film strip, and s is the distance between the edges of the electrodes (1.000 in.).

Results of the 60 resistivity measurements made using this technique are presented in Table 1. The average resistivity of the samples was 13.54 Ω/sq., and the standard deviation was 0.42 Ω/sq. Assuming tnat the resistivity of the gold-film has a normal distribution about its mean value, then 95% of the samples should have a resistivity of 13.54 Ω/sq. ± 6.2%. This variation in resistivity of gold-film samples is similar to the values reported elsewhere [2,5,9].

2.3.3 Emissivity of the Gold-Film

The average gold-film temperature in the experiments was approximately 45°C. With this gold-film temperature, more than 99% of the radiation is emitted in the wavelength range of $5\ \mu m < \lambda < 100\ \mu m$. Thus, an average emissivity of the gold-film for this wavelength range is required. Unfortunately, the manufacturer of the gold-film has not published radiation properties in the far infrared portion of the electromagnetic spectrum. These measurements could not be made within the timeframe of

this work and the available resources, so the emissivity of the gold-film had to be estimated.

A balance on radiation incident on the surface of the gold-film yields:

$$\rho_\lambda + \alpha_\lambda + \tau_\lambda = 1 \tag{2-5}$$

where ρ_λ, α_λ, and τ_λ are the spectral, hemispherical reflectivity, absorptivity, and transmissivity, respectively. If it is assumed that the irradiation on the gold-film surface is diffuse, Kirchhoff's law [67,68] states that:

$$\varepsilon_\lambda = \alpha_\lambda \tag{2-6}$$

where ε_λ is the spectral, hemispherical emissivity. Substituting this relation into Eq. (2-5), the emissivity of the gold-film may be evaluated as:

$$\varepsilon_\lambda = 1 - \rho_\lambda - \tau_\lambda \tag{2-7}$$

Neher and Edwards [69] published measurements of diffuse reflectance spectra for vacuum-evaporated gold on a wire mesh bonded to mylar. They made their measurements using a far infrared reflectometer. Data were obtained in the wavelength range of $2\ \mu m < \lambda < 100\ \mu m$. In this wavelength range, the reflectance measured 0.78 ± 0.04. Assuming that the transmissivity is also reasonably constant over this wavelength range, and substituting this reflectivity value into Eq. (2-7), the emissivity of the gold-film is:

$$\varepsilon = 0.22 - \tau \qquad 2\ \mu m < \lambda < 100\ \mu m \tag{2-8}$$

The gold-film is designed such that its transmissivity in the infrared region is very low. Therefore, one might expect that the emissivity of the gold-film would be only slightly lower than 0.22. In comparison, the manufacturer [9] has recommended that an emissivity in the range of $0.1 < \varepsilon < 0.2$ be used for radiation calculations.

It was decided that the value of the emissivity would be fine-tuned using some of the results from the horizontal concentric annulus experiment. In particular, the emissivity would be chosen so that the total rate of ohmic heating is equal to the sum of the rates of convection and radiation heat transfer at the gold-film surface. This is simply an integration of Eq. (2-1) over the surface of the gold-film. The heat conduction term drops out because the effect of conduction in this particular experiment, after steady state has been achieved and ignoring end losses, is only to redistribute the heat generated by the gold-film. In mathematical terms, the energy balance applied to the gold-film heater may be expressed as:

$$Q_e \cong \sum_{i=1}^{N} \left(q_{rad_i} A_i + q_{cnv_i} A_i \right) \qquad (2\text{-}9)$$

where Q_e is the power supplied to the gold-film, $q_{rad_i} A_i$ is the net rate of heat transfer from the gold-film to the surroundings by radiation from a small area, A_i, surrounding point i, and $q_{cnv_i} A_i$ is the rate of convection heat transfer from the gold-film to the fluid over the area A_i. In this equation, the only unknowns are q_{rad_i}. To determine the laminar natural convection heat fluxes in this equation, an accurate numerical simulation of the fluid flow and heat transfer in the horizontal concentric annulus

was used. Eq. (2-9) may be solved to determine the total rate of heat transfer by radiation, and then an average value of the total, hemispherical emissivity of the gold-film may be calculated using Eq. (4-27). In this work, the emissivity of the gold-film was determined to be 0.18.

2.3.4 Thermocouple Calibration

The National Bureau of Standards have tabulated temperature as a function of voltage for chromel-constantan (Type-E) thermocouples [65], and a 9th order power-series polynomial, which is accurate to $\pm 0.5^{\circ}C$ over the temperature range of $-100^{\circ}C$ to $1000^{\circ}C$, has been fitted to the data. Because the maximum temperature variation over the surface of the gold-film heater was expected to be as low as $2^{\circ}C$ for some test runs, it was decided that accuracies in temperature measurement of approximately $\pm 0.1^{\circ}C$ would be needed. As the Seebeck coefficient for Type-E thermocouples is approximately 60 $\mu V/^{\circ}C$ at $20^{\circ}C$, the best temperature accuracy that may be obtained with a 1 μV resolution voltmeter, is $0.017^{\circ}C$. Thus, the objective of $0.1^{\circ}C$ accuracy in temperature measurements using Type-E thermocouples may be achieved.

A procedure was developed to calibrate each thermocouple individually against a quartz thermometer over a temperature range of $16^{\circ}C$ to $74^{\circ}C$. The procedure employed to obtain the required temperature-voltage data and estimate the uncertainty of the power-series polynomials fitted to this data is summarized as follows:

(1) The uncalibrated thermocouples and the quartz thermometer were placed into a round copper block , and set carefully into the centre of a water bath (see Section 2.2.4 for equipment specifications).

(2) The water bath temperature controller was set to the lowest temperature in the calibration range (~16°C). The sequence of proceeding from lower to higher temperatures is recommended by the manufacturer of the quartz thermometer to minimize hysteresis effects.

(3) Data was acquired after the quartz thermometer displayed a constant temperature reading (±0.003°C) for at least 5 minutes. The sequence of reading each thermocouple voltage and the quartz thermometer was performed five times, and average voltage values for each thermocouple and the corresponding temperature were obtained.

(4) Step (3) was repeated at 2°C increments in water bath temperature, from 16°C to 74°C.

(5) A fourth-order power-series polynomial equation was fitted to the temperature-voltage data for each thermocouple, using the least squares method, giving:

$$T_j = \sum_{i=0}^{4} \left[C_{i,j} \left(V_j \right)^i \right] \qquad (2\text{-}10)$$

where V_j is the voltage reading of thermocouple j, and $C_{i,j}$ are the polynomial coefficients for thermocouple j.

(6) Steps (2) and (3) were repeated, using 0.1°C increments in temperature, for the temperature ranges of 24.7°C to 25.2°C, 44.7°C to 45.2°C, and 64.7°C to 65.2°C, at least three days after the initial data was taken. The three day delay in time permitted quartz thermometer temperature hysteresis errors to be minimized.

(7) The errors in the temperatures, T_j, obtained by using Eq. (2-10) developed in step (5) for each thermocouple j, were determined by comparing them with the quartz thermometer readings at comparable data points.

The aforementioned procedure was followed to calibrate 40 thermocouples for each experiment. Thermocouple calibrations were done approximately two weeks before each experiment was performed to ensure that the 90 day voltmeter measurement accuracy specification was applicable. Analysis of the results from steps (6) and (7) showed that the difference between the temperatures obtained using the calibration polynomial equations and the quartz thermometer were within ±0.05°C for 95% of the temperature measurements. This result is valid for all three temperature ranges considered in step (6) and for both sets of thermocouple calibrations.

CHAPTER III

LAMINAR NATURAL CONVECTION ALONG A VERTICAL FLAT PLATE

3.1 PROBLEM STATEMENT

The classical heat transfer problem of two-dimensional, steady state, laminar natural convection along a vertical flat plate in an extensive quiescent medium is studied in this chapter. A diagram of the problem is presented in Fig. 9. This problem was selected for the first test of the proposed gold-film technique for two reasons. Firstly, the numerical solution to the problem of natural convection along a vertical flat plate with a constant heat flux boundary condition, obtained by Sparrow and Gregg [47], has been verified experimentally by Sparrow and Carlson [46]. Thus, this test problem enables a critical analysis of the proposed gold-film technique to be made. Secondly, the design and construction of the experimental apparatus is relatively simple and inexpensive.

The two main objectives of this work were: (i) to use the proposed gold-film technique to take local heat transfer measurements of natural convection along a vertical flat plate; and (ii) to compare the experimental results to those of an accurate numerical simulation of the problem.

The equations governing laminar natural convection heat transfer along a vertical flat plate are presented in the next two sections. This is followed by a discussion of the numerical algorithm used to solve the

governing equations. Then, the design and construction details of the experimental apparatus are given. A comparison between the results of the experimental investigation and the numerical simulation is then made. Uncertainties in the experimental results are also discussed.

3.2 NUMERICAL SIMULATION

3.2.1 Governing Equations and Assumptions

The equations governing two-dimensional, steady state, laminar natural convection along a vertical flat plate are presented in this section, with reference to the Cartesian coordinate system shown in Fig. 9. The following assumptions have been made to simplify these equations: (i) the boundary-layer approximations [70] are valid for this problem ; (ii) the fluid is Newtonian, and all its thermophysical properties, except the mass density, are constant; (iii) the mass density is constant in all terms of the governing equations except the buoyancy term; and (iv) viscous dissipation is negligible. Assumption (iii) is known as the Boussinesq approximation [67,68]. The mass density may be expressed in the following approximate form in the buoyancy term:

$$\rho_\infty - \rho = \rho_\infty \beta \left(T - T_\infty \right) \qquad (3\text{-}1)$$

where β is the thermal volumetric expansion coefficient.

The set of governing equations, after invoking the aforementioned four assumptions, reduces to the following [67,68]:

x-momentum

$$u \frac{\partial u}{\partial x} + v \frac{\partial u}{\partial y} = g\beta \left(T - T_\infty \right) + \nu \frac{\partial^2 u}{\partial y^2} \tag{3-2}$$

energy

$$u \frac{\partial T}{\partial x} + v \frac{\partial T}{\partial y} = \alpha \frac{\partial^2 T}{\partial y^2} \tag{3-3}$$

continuity

$$\frac{\partial u}{\partial x} + \frac{\partial v}{\partial y} = 0 \tag{3-4}$$

In addition to Eqs. (3-2) to (3-4), boundary conditions are needed to complete the mathematical model. Again referring to Fig. 9, the boundary conditions for this problem are:

$$\begin{aligned} &\text{(i)} \quad \text{at } y = 0: \quad u = v = 0 \; ; \quad q = q_w \\ &\text{(ii)} \quad \text{at } y \to \infty: \quad u \to 0 \; ; \quad v \to 0 \; ; \quad T \to T_\infty \end{aligned} \tag{3-5}$$

The dimensionless parameters that govern natural convection may be obtained by nondimensionalizing Eqs. (3-2) to (3-4). Introducing,

$$\begin{gathered} x^* = x/L \; ; \quad y^* = y/L \; ; \quad u^* = uL/\nu \; ; \quad v^* = vL/\nu \; ; \\ T^* = \frac{(T - T_\infty)}{(q_w L/k)} \end{gathered} \tag{3-6}$$

the governing equations reduce to:

x-momentum

$$u^* \frac{\partial u^*}{\partial x^*} + v^* \frac{\partial u^*}{\partial y^*} = Gr_L^* T^* + \frac{\partial^2 u^*}{\partial y^{*2}} \tag{3-7}$$

energy

$$u^* \frac{\partial T^*}{\partial x^*} + v^* \frac{\partial T^*}{\partial y^*} = \frac{1}{Pr} \frac{\partial^2 T^*}{\partial y^{*2}} \tag{3-8}$$

continuity

$$\frac{\partial u^*}{\partial x^*} + \frac{\partial v^*}{\partial y^*} = 0 \tag{3-9}$$

The two parameters, Pr, the Prandtl number, and Gr_L^*, the modified Grashof number, are defined as follows:

$$Pr = \frac{\nu}{\alpha} \tag{3-10}$$

$$Gr_L^* = \left(\frac{g\beta q_w L^4}{\nu^2 k} \right) \tag{3-11}$$

3.2.2 Similarity Transformation

In Section 3.2.1, the partial differential equations governing natural convection along a vertical flat plate were presented. In this section, Eqs. (3-7) to (3-9) will be reduced to two ordinary differential equations by introducing a similarity transformation.

Firstly, a stream function, ψ, is defined by the following two equations:

$$u = \frac{\partial \psi}{\partial y} \tag{3-12}$$

$$v = - \frac{\partial \psi}{\partial x} \tag{3-13}$$

Sparrow and Gregg [47] showed that the x-momentum and energy equations may be reduced to two ordinary differential equations using the following similarity transformation:

$$\eta = C_1 \frac{y}{x^{1/5}} \tag{3-14}$$

$$F(\eta) = \frac{\psi}{C_2 \, x^{4/5}} \tag{3-15}$$

$$\theta(\eta) = \frac{C_1 \, (T_\infty - T)}{(x^{1/5} \, q_w/k)} \tag{3-16}$$

where:

$$C_1 = \left[\frac{g \beta q_w}{5 k \nu^2} \right]^{1/5} \tag{3-17}$$

$$C_2 = \left[\frac{5^4 g \beta q_w \nu^3}{k} \right]^{1/5} \tag{3-18}$$

After substituting the above expressions into the governing equations, and performing the required differentiations, the governing equations can be written as follows:

<u>x momentum</u>

$$F''' - 3 (F')^2 + 4F (F'') - \theta = 0 \tag{3-19}$$

<u>energy</u>

$$\theta'' + Pr (4\theta' F - \theta F') = 0 \tag{3-20}$$

where the primed quantities indicate derivatives with respect to η. Note that the continuity equation is automatically satisfied by the introduction of the stream function. The boundary conditions given in Eq. (3-5) are transformed to the following:

$$\begin{aligned} &\text{(i)} \quad \text{at } \eta = 0: \quad F = F' = 0 \; ; \quad \theta' = 1 \\ &\text{(ii)} \quad \text{at } \eta \to \infty: \quad F' \to 0 \; ; \quad \theta \to 0 \end{aligned} \tag{3-21}$$

The Nusselt number is evaluated as follows:

$$Nu_x = \left(\frac{q_w}{(T_{w_x} - T_\infty)} \right) \left(\frac{x}{k} \right) = \left(\frac{-1}{5^{1/5}\, \theta(0)} \right) Gr_x^{*\,1/5} \tag{3-22}$$

where Gr_x^* is the modified Grashof number, and is defined as follows:

$$Gr_x^* = \left(\frac{g\beta q_w x^4}{\nu^2 k} \right) \tag{3-23}$$

The temperature distribution at the surface of the vertical flat plate is:

$$T_{w_x} - T_\infty = -5^{1/5}\, \theta(0) \left(\frac{q_w x}{k} \right) Gr_x^{*\,-1/5} \tag{3-24}$$

Eqs. (3-19) and (3-20), subject to boundary conditions (3-21), were solved numerically by Sparrow and Gregg [47] using a "shooting" method, for Prandtl numbers of 0.1, 1.0, 10.0 and 100.0. As the experiments in this study were performed with air as the working fluid, it was necessary to solve the equations for a Prandtl number of 0.7.

3.2.3 Numerical Solution

In this work, an iterative finite-difference method for boundary value problems was used to solve Eqs. (3-19) and (3-20), with the boundary

conditions given in Eq. (3-21). The main advantage of using a finite-difference method for solving these differential equations is that both the specified initial and terminal boundary conditions are incorporated into the set of discretization equations. This is in direct contrast to "shooting" methods, where additional boundary conditions at the initial point are assumed, and then the differential equations are integrated to the terminal conditions. The guessed boundary conditions are progressively updated, and the integrations are repeated, until the terminal conditions are satisfied. Secondly, as will be seen, the linearized finite-difference equations exhibit a banded matrix structure. Efficient algorithms are available for the solution of linear algebraic equations of this form [71].

The finite-difference form of the derivatives, for unequal η grid spacing, were obtained by manipulating truncated Taylor series for $F(\eta)$ and $\theta(\eta)$. The Taylor series expansions were combined to derive central-difference formulae for the derivatives. The general procedure is outlined in most textbooks dealing with numerical methods, for example [72,73].

Non-linearities in the x-momentum and energy equations were handled by iteratively solving a set of nominally linear equations. The equations used for linearizing products of $F(\eta)$ in this work are:

$$F_i \; F_j = F_i^* \; F_j + F_i \; F_j^* - F_i^* \; F_j^* \qquad i \neq j \tag{3-25}$$

$$F_i^2 = 2F_i \; F_i^* - F_i^{*\,2} \tag{3-26}$$

where * quantities are estimates of $F(\eta)$ from a previous iteration, and i and j are η grid points. Similar equations were used for linearizing products of $\theta(\eta)$.

Iterations were also required in this work because the coupled system of $F(\eta)$ and $\theta(\eta)$ equations were solved sequentially. In solving the momentum equation, $\theta(\eta)$ values from the previous solution of the energy equation were used. Likewise, $F(\eta)$ values from the last iteration of the momentum equation were used to solve the energy equation.

The finite-difference expression used in this work for approximating $F'''(\eta)$ involves five adjacent values of $F(\eta)$. When the discretized x-momentum equations are put into matrix form, the coefficient matrix for $F(\eta)$ is known as a pentadiagonal matrix because all elements of the matrix are zero except those along the central five diagonals. Two special discretization equations must be generated at each of the two bounding values of η in order to complete the set of discretization equations for $F(\eta)$. Three of these equations come directly from applying the boundary conditions at $\eta = 0$ and $\eta \to \infty$, using forward- and backward-difference schemes, respectively. The fourth equation was obtained by setting $F''(\infty) = 0$. Numerical oscillation could occur if the fourth equation is not properly chosen [71].

The finite-difference approximation of the second-order derivatives for $\theta(\eta)$ used in this work involve three adjacent θ values. Thus, the resultant coefficient matrix for $\theta(\eta)$ takes the form of a tridiagonal matrix. The boundary conditions at $\eta = 0$ and $\eta \to \infty$ provide the two additional equations required to complete the set of discretization equations for $\theta(\eta)$.

Two of the boundary conditions for $F(\eta)$ and $\theta(\eta)$ are specified at $\eta \rightarrow \infty$. The maximum value of η, beyond which the solutions of the two sets of discretization equations were independent of the maximum value of η to within a certain tolerance, was denoted as η_{max}. This was determined by solving the two sets of discretization equations a number of times with increasing maximum values of η, while maintaining the same grid point density.

The algorithm used to solve the two sets of coupled discretization equations for $F(\eta)$ and $\theta(\eta)$ is summarized below:

(1) Discretize the calculation domain: Provide an initial guess for η_{max} and specify values of η at all grid points.

(2) Provide guessed values for $F(\eta)$ and $\theta(\eta)$ at all grid points. Use specified values at boundary points, if possible.

(3) Calculate the coefficients in the discretized $F(\eta)$ equations, and solve the resultant equations for $F(\eta)$ using the pentadiagonal matrix algorithm [71].

(4) Calculate the coefficients in the discretized $\theta(\eta)$ equations, and solve the resultant equations for $\theta(\eta)$ using the tridiagonal matrix algorithm [71].

(5) Repeat steps (3) and (4) using most recent values of $F(\eta)$ and $\theta(\eta)$ until the solution has converged. Convergence was monitored by

calculating the relative changes in $F''(0)$ and $\theta(0)$. When the absolute values of these changes were smaller than 1×10^{-6} between successive iterations, the solution was considered to be converged.

(6) Repeat steps (2) to (5) with a different η_{max} and the same grid point concentration until grid independence has been obtained. Grid independence was defined by absolute relative changes of less than 1×10^{-3} in $F''(0)$ and $\theta(0)$ after η_{max} has been doubled.

It must be noted, with regard to step (5), that there is no guarantee that the above procedure will provide a converged solution for $F(\eta)$ and $\theta(\eta)$. In this work, however, converged solutions were obtained for all cases considered. The changes in $F(\eta)$ and $\theta(\eta)$ were under-relaxed because initial tests showed that this enhanced the rate of convergence of the iterative solution algorithm. An under-relaxation factor of 0.7 was used for both sets of discretization equations.

A powerlaw grid, generated by the following equation, was used to concentrate grid points close to the wall:

$$\eta_i = \eta_{max} \left(\frac{i - 1}{N - 1} \right)^{powlaw} \qquad i = 1, N \qquad (3\text{-}27)$$

where N = number of grid points

$powlaw = 1.3$ (for this problem)

The validity of the computer code incorporating the proposed solution procedure was verified using the results of Sparrow and Gregg [47] for Prandtl numbers of 0.1, 1.0, 10.0, and 100.0. A comparison between the present results and those of Sparrow and Gregg is provided in Table 2.

The differential equations were also solved for a fluid with a Prandtl number of 0.70. Substituting the value of $\theta(0)$ into Eq. (3-22), the local Nusselt number may be calculated as follows:

$$Nu_x = 2.06\ Gr_x^{*1/5} \tag{3-28}$$

3.2.4 Application of Numerical Results

The following details must be considered when Eq. (3-28) is used to predict local Nusselt numbers for laminar natural convection heat transfer along a vertical flat plate: (i) the convection heat flux must be determined; and (ii) a suitable reference temperature for evaluating the thermophysical fluid properties is required.

In Section 2.1, an energy balance at the surface of the gold-film heater indicated that conduction and radiation heat transfer must be evaluated in order to calculate local convection heat fluxes. However, the similarity solution presented in the previous sections is only valid for a constant convection heat flux leaving the surface of the vertical flat plate. In this work, an average convection heat flux was determined for each experimental run and used in the corresponding similarity solution. If the similarity solution is to be a meaningful test of the experimental results, the experimental apparatus should be designed so that the convection heat flux is nearly constant along the vertical flat plate. In Section 3.3.1, it will be shown that conduction heat transfer was minimized, by design, for the vertical flat plate apparatus. Thus, only radiation heat transfer remains to be considered.

A procedure was developed to account for an average radiation heat flux from the surface of the gold-film heater. It was determined that the difference between the local and mean radiation heat transfer at any position on the plate will be less than 6% if the difference between the maximum and minimum temperature along the plate is 10°C and the average plate temperature is 318 K.

Consider the flat plate apparatus and the constant temperature box shown in Fig 10. Assuming that the surfaces are diffuse and gray, and that the vertical flat plate may be treated as a small convex object in a large isothermal cavity, the net radiation heat flux leaving a point i on the surface of the vertical flat plate is given by:

$$q_{rad_i} = \sigma \, \varepsilon_w \left(T_{w_i}^4 - T_{box}^4 \right) \tag{3-29}$$

where σ is the Stefan-Boltzmann constant, and ε_w is the emissivity of the gold-film heater. The total net rate of heat transfer by radiation is obtained by using the following approximation:

$$Q_{rad} = \int_0^A q_{rad_i} \, dA \cong \sigma \, \varepsilon_w \sum_{i=1}^{N} \left[\left(T_{w_i}^4 - T_{box}^4 \right) A_{w_i} \right] \tag{3-30}$$

The plate surface temperatures in the above summation were obtained from a cubic spline fit through the experimental data points. The summation was performed in increments of 6.4 mm (1/4 in.) height along the length of the plate. The average radiation heat flux leaving the vertical flat plate is:

$$\bar{q}_{rad} = \frac{Q_{rad}}{A_w} \tag{3-31}$$

Assuming that heat conduction inside the plate is negligible, the average convection heat flux leaving the surface is:

$$\bar{q}_{conv} = q_e - \bar{q}_{rad} \tag{3-32}$$

The thermophysical properties of the fluid were assumed to be constant, as discussed in Section 3.2.1. However, because the fluid temperature varies across the boundary layer, a suitable reference temperature must be chosen to evaluate the fluid properties. In this work, the thermophysical fluid properties were evaluated at a film temperature, T_f, defined by:

$$T_f = \frac{\bar{T}_w + T_{air}}{2} \tag{3-33}$$

An iterative procedure is required to calculate the film temperature, T_f, because the average wall temperature is not known a priori. Firstly, the film temperature is estimated. This allows the modified Grashof number, Gr_x^*, and the plate temperature, T_{w_x}, distribution to be calculated from Eqs. (3-23) and (3-24), respectively. Then, a better estimate of the film temperature is calculated using this new plate temperature distribution to evaluate $\bar{T}_w$. This procedure was repeated until the absolute relative change in Nusselt number between successive iterations was less than 10^{-6}.

3.3 EXPERIMENTAL MEASUREMENTS

3.3.1 Flat Plate Apparatus

A number of constraints were placed on the design of the flat plate apparatus due to limitations of the gold-film heater, the equipment and

instrumentation available in the Heat Transfer Laboratory, and the range of data to be acquired. The major constraints on the design were:

(1) The apparatus was to be designed to provide two-dimensional, steady state, laminar natural convection air flow along the length of the vertical flat plate. The data presented by Vliet and Liu [42] was used to ensure this.

(2) According to the manufacturer, the Intrex gold-film is only stable to approximately 90°C at the coating interface. However, as Baughn et al. [9] reported that they had never heated the gold-film beyond 60°C, this experiment was designed to generate a maximum gold-film temperature of less than 60°C.

(3) The power supply used in this experiment is capable of supplying 60 W of very stable power. However, the maximum allowable voltage and current are 60 V and 1 A, respectively.

(4) The apparatus was to be constructed of stock materials, for both time and financial resource considerations.

(5) The dimensions of the vertical flat plate apparatus were to be such that it could fit into the Heat Transfer Laboratory's constant temperature box. Moreover, as the box was to be used to simulate an extensive, quiescent medium, it was necessary to keep the dimensions of the flat plate small in comparison to the size of the box.

(6) As the similarity solution presented in Section 3.2.3 is valid for a constant heat flux boundary condition, the experiment was to be designed to minimize conduction and radiation heat transfer.

The flat plate was fabricated from plexiglas, with dimensions of 609.6 mm height x 304.8 mm width x 9.5 mm thickness (24 in. x 12 in. x 3/8 in.). However, only a 203.2 mm x 203.2 mm (8 in. x 8 in.) region at the bottom of the plexiglas plate was heated. The back of the plexiglas plate was milled to a thickness of 3.2 mm (1/8 in.) within the heated region.

Spanwise heat conduction at the centreline of the plate was expected to be negligible because of the combination of a thin (3.2 mm) plexiglas plate and small temperature gradients. Longitudinal heat conduction was only expected to be significant at the very top and bottom of the heated region where large temperature gradients exist. Heat transfer through the back of the vertical plate was minimized by providing an identical flat plate with a gold-film heater, 25.4 mm (1 in.) behind the main plate, and filling the space in between with fiberglas insulation. This produces a plane of symmetry between the two heated plates, and conduction heat transfer does not, theoretically, take place across this plane.

On the main test plate, 29 holes of 2.4 mm (3/32 in.) diameter were drilled through the plexiglas for the insertion of thermocouples. The thermocouples located on the centreline of the test plate were used for the calculation of local heat transfer. Rows of thermocouples were placed 25.4 mm (1 in.) on either side of the centreline so that the two-dimensionality of the convection heat transfer along the centre of the

plate could be ascertained. The thermocouple locations, measured from the the leading edge of the plate, were 6.4, 12.7, 25.4, 38.1, 50.8, 76.2, 101.6, 127.0, and 152.4 mm (1/4, 1/2, 1, 1 1/2, 2, 3, 4, 5, and 6 in.). Temperature measurements were only made on the lower 152.4 mm of the plate because it was determined that longitudinal heat conduction would be significant in the upper 50.8 mm of the heated region. Two additional thermocouples were positioned 101.6 mm from the leading edge and 50.8 mm on either side of the vertical centreline of the plate. Another thermocouple, shielded to minimize radiation heat transfer [11], was used to measure air temperature.

The vertical flat plates were fabricated in the following manner. After the machining operations were completed, a 304.8 mm (12 in.) x 304.8 mm (12 in.) liquid crystal sheet with double-sided adhesive backing (Davis Liquid Crystals, Cat. No. 5034-3540) was attached to each plexiglas plate. Then, the thermocouples were attached to the back of the liquid crystal sheets through the drilled holes, using epoxy (Lepage, two-part epoxy resin and hardener). The epoxy was carefully applied so that the 2.4 mm diameter holes in the plexiglas would be completely filled. The lead wires of the thermocouples were epoxied to the plexiglas along the expected isotherms to minimize errors due to heat conduction along the thermocouple wires.

The gold-film heater was fabricated as follows. A 254.0 mm (10 in.) length of gold-film was cut from the 304.8 mm wide sample roll. The gold coating was protected with removable tape (3M, Scotch Brand Magic Plus), and double-sided adhesive (3M, Scotch Brand Tape No. Y9473) was applied to the back of the plastic sheet prior to making the precision cuts, as

discussed in Section 2.2.2. The manufacturer of the gold-film suggests that the heater elements be constructed so that current flow is along the web length. Accordingly, the central 203.2 mm (8 in.) region was used from the 304.8 mm wide piece of gold-film. The 203.2 mm dimension of the gold-film piece became the lengthwise dimension of the heater on the vertical flat plate. The spanwise dimension of the heater did not have to be cut precisely because the construction of the electrodes was designed to ensure that this would be 203.2 mm (8 in.).

Attachment of the gold-film heater to the liquid crystal sheet required two patient people. This work had to be done carefully because the double-sided adhesive could not be moved once it contacted the liquid crystal sheet located on the flat plate. The procedure involved one person peeling the backing tape from the double-sided adhesive, while the other person simultaneously allowed short lengths of the double-sided adhesive on the back of the heater to make contact with the liquid crystal sheet. The gold-film was then very carefully rolled with a plexiglas tube to make sure that the double-sided adhesive stuck uniformly to the liquid crystal sheet. Finally, the protective tape located on the top surface of the gold-film was removed.

The electrodes for the vertical flat plate experiment were fabricated using the procedure discussed in Section 2.3.1. The dimensions of the copper bars, containing the power lead connections, were 25.4 mm x 25.4 mm x 203.2 mm (1 in. x 1 in. x 8 in.).

A stand with adjustable legs was constructed to hold the two flat

plates in a vertical position. This stand may be seen in Fig. 10. The flat plates were bolted to a square steel bar, which was machined at the two ends to produce round cross-sections. The vertical members of the stand were made from an aluminum channel. The ends of the steel bar were inserted into holes cut into the vertical members. This allowed the flat plate to rotate in order to perform experiments on an inclined plate, if desired. For these experiments, the plates were held in a vertical position by a locking mechanism.

The flat plate apparatus was placed in a constant temperature box, which was designed and built by the Heat Transfer group at McGill University. The dimensions of the box are approximately 1750 mm height x 1750 mm width x 1200 mm depth. Four of the walls in the constant temperature box are water-cooled. The water is supplied to the walls from an insulated waterbath, which contains heating and cooling units. The waterbath is cooled by tap water (at about $5^{\circ}C$) which passes through a heat exchanger inside the waterbath. The heating section inside the waterbath consists of two heating coils. A proportional temperature controller (Omega, Model 49) maintains the waterbath set temperature by controlling the power supplied to the heating coils. The four temperature-controlled walls of the box were instrumented with chromel-constantan thermocouples, which were individually calibrated by another graduate student. The other two walls of the box are made of plexiglas sheets, which were designed to be easily removed. The plexiglas walls were insulated for this work with 101.6 mm (4 in.) of fiberglas pink insulation and 25.4 mm (1 in.) of styrofoam insulation.

3.3.2 Test Procedure

The modified Grashof number, Gr_L^*, was varied in these experiments by adjusting the power supplied to the gold-film heaters on the main and back plates. From a numerical simulation of the vertical flat plate problem, not accounting for radiation and conduction heat transfer, it was determined that a surface heat flux of 125 W/m^2 would produce a temperature approximately 33°C above the ambient temperature at the top of the gold-film heater. Thus, if the ambient temperature is maintained at 20°C, the maximum gold-film heater temperature will be less than 60°C, as desired.

Five experimental runs were performed with modified Grashof numbers of 5.6×10^7, 1.1×10^8, 1.6×10^8, 2.1×10^8 and 2.7×10^8, which produced laminar natural convection flow along the heated length of the plate [42]. The corresponding average heat fluxes supplied to the gold-film heater for the five runs were approximately 25, 50, 75, 100 and 125 W/m^2. Repeatability runs were performed for the 25 and 125 W/m^2 heat flux test cases.

The main and back plate gold-film heaters were connected in series for these experiments because the electrical resistances of the two heaters were within 1% of each other. This simplified the experimental equipment requirement as only one power supply was needed.

The data acquisition program employed to take experimental data is described in Appendix A. For each run, the data acquisition program was

left to monitor the gold-film heater temperatures for at least 24 hours after the power supply to the heater had been turned on and set. This was done to ensure that steady state was achieved. The limiting factor influencing the degree of steady state was the ability of the temperature controller to maintain a set temperature for the walls of the constant temperature box. In these experiments, the average wall temperature of the box fluctuated slowly with time, perhaps by as much as $\pm 0.3^{\circ}C$ over a 24 hour period. However, the local gold-film heater temperatures were also found to fluctuate in a similar manner to the average wall temperature of the box. Therefore, steady state was defined by constant differences between the heater temperatures and the average wall temperature of the box.

3.3.3 Calculation of Convection Heat Flux

In Section 2.1, an energy balance was written for the gold-film heater to obtain a general expression for the local convection heat flux, namely:

$$q_{conv_x} = q_e - q_{rad_x} - q_{cnd_x} \tag{3-34}$$

The vertical flat plate experiment was carefully designed to minimize conduction heat transfer. These design details have already been presented in Section 3.3.1. An expression describing the net local radiation heat flux leaving the vertical flat plate heater was derived in Section 3.2.4. Substituting Eq. (3-29) into Eq. (3-34), the local convection heat flux is given by:

$$q_{conv_x} = q_e - \sigma \varepsilon_w \left(T_{w_x}^4 - T_{box}^4 \right) \tag{3-35}$$

3.4 PRESENTATION AND DISCUSSION OF RESULTS

3.4.1 Establishment of Two-Dimensionality of Heat Transfer

Before presenting the final experimental results, the assumption of two-dimensional natural convection heat transfer must be verified. This assumption was made to simplify the governing equations for the numerical simulation. The temperature gradient in the spanwise direction along the centreline of the plate must be very small in order to neglect spanwise heat transfer. Thermocouples were installed on both sides of the centreline of the vertical flat plate to validate this assumption.

For the test cases of $Gr_L^* = 5.6 \times 10^7$ and $Gr_L^* = 2.7 \times 10^8$, spanwise temperature profiles were plotted as a function of distance from the centreline of the vertical flat plate, and are shown in Figs. 11 and 12, respectively. In these two figures, the temperature distribution along the vertical centreline is denoted by "CENTRE", while the temperature distributions 25.4 mm to the left and right of the vertical centreline are indicated by "LEFT" and "RIGHT". For $Gr_L^* = 5.6 \times 10^7$, the temperatures along the left- and right-hand measurement locations on the plate were always within $\pm 0.21^\circ C$ and $\pm 0.12^\circ C$ of the centreline temperature at the corresponding location, respectively. The temperatures for $Gr_L^* = 2.7 \times 10^8$ showed larger temperature variations due to the higher average heat flux, but were still within $\pm 0.97^\circ C$ and $\pm 0.33^\circ C$ for the left- and right-hand sides, respectively.

Qualitative estimates of the temperature across the entire width of the

plate were obtained by examining the colour produced by the liquid crystal sheet which was placed beneath the gold-film heater. A representative photograph is given in Fig. 13. In the photograph, each colour represents an isotherm on the vertical flat plate. Since the isotherms are relatively horizontal across the central region of the plate, they indicate that spanwise heat conduction may be neglected.

The centreline temperatures were not consistently higher or lower than those at the corresponding off-centre measurement locations. On the basis of these results, it was assumed that along the central region of the test plate, two-dimensionality of the natural convection flow was indeed established, for all practical purposes, in this work.

3.4.2 Local Nusselt Numbers

Results

A theoretical relationship between Nusselt number, Nu_x, and non-dimensional distance, x/L, was presented for natural convection heat transfer along a vertical flat plate with a uniform heat flux boundary condition in Section 3.2.2. For a given fluid with constant thermophysical properties, $Nu_x \sim (x/L)^{0.8}$. This result arises because the local heat transfer coefficient, h_x, decreases in the flow direction according to $h_x \sim (x/L)^{-0.2}$, and $Nu_x = (h_x x/k_f)$.

Graphs of local Nusselt number, Nu_x, are plotted as a function of the non-dimensional distance along the vertical flat plate, x/L, in Figs. 14

to 18. The experimental results in each figure are marked with discrete points, while the numerical results are represented by a continuous curve. In addition, a summary of these experimental results, including the results of the corresponding uncertainty analysis, are presented in Tables 3 to 7. Details of the uncertainty analysis and a discussion of the repeatability of the results are given in the following subsections.

A few general comments pertain to all of the experimental runs. Firstly, the experimental Nusselt numbers are generally within ±9% of the numerical results for $1/6 < x/L < 1.0$. This is within the uncertainty in the experimental results. At $x/L = 1/24$, the experimental Nusselt number results lie approximately 28% above the numerical results for all runs. This can be explained by the fact that longitudinal heat conduction within the plate was not accounted for in the calculation of the convection heat flux at the surface of the plate. Longitudinal heat conduction within the plate is quite significant at the very bottom of the vertical flat plate because of the large temperature gradients in that region, and this decreases the corresponding convection heat flux. If this heat conduction was accounted for, the experimental Nusselt numbers at the bottom of the plate would be lower. The fact that the experimental Nusselt numbers are consistently higher than the corresponding numerical results by about 28% at $x/L = 1/24$ supports the explanation that there is a fixed error in the experimental results at this location.

In these experiments, 18% to 22% of the heat generated by the gold-film heater is transferred to the constant temperature box by radiation, as is shown in the results in Tables 3 to 7. This result may intuitively

appear to be quite high, but the low rates of heat transfer by natural convection in air make radiation a significant mode of heat transfer in the experiments undertaken in this work.

Uncertainty Analysis

Kline and McClintock [74] presented one of the first engineering papers dealing with single-sample uncertainty analysis. Their method is based on specifying all experimental measurements in terms of an expected accuracy of the measurement with 20 to 1 odds. For example, an experimental measurement may be recorded as:

$$x_i = \bar{x}_i \pm w_i \ (20{:}1) \tag{3-36}$$

where i is the measurement number, $\bar{x}_i$ is the mean value of the readings, w_i is the uncertainty in the reading, and (20:1) is the specified odds. A result, R, which is a function of many measurements may be expressed as:

$$R = R\ (\ x_1,\ x_2,\ x_3,\ .....,\ x_N\ ) \tag{3-37}$$

The uncertainty in the final result, w_R, with the same odds as the measurements, is given by:

$$w_R = \left[\sum_{i=1}^{N} \left(\frac{\partial R}{\partial x_i} w_i \right)^2 \right]^{1/2} \tag{3-38}$$

In the remainder of this section, results of a single-sample uncertainty analysis for the calculation of local experimental Nusselt numbers are presented.

The equation for calculating local experimental Nusselt numbers, obtained by substituting Eq. (3-35) into Eq. (2-3), is:

$$Nu_x = \left(\frac{q_e - \sigma \varepsilon_w \left(T_{w_x}^4 - T_{box}^4 \right)}{\left(T_{w_x} - T_{air} \right)} \right) \left(\frac{x}{k_f} \right) \qquad (3\text{-}39)$$

An examination of Eq. (3-39) shows that there are a total of five different quantities for which a measurement accuracy must be specified. These quantities are the local heat flux generated by the gold-film heater, temperature measurements, location of temperature measurements, the emissivity of the gold-film heater, and the thermal conductivity of air.

The local heat flux generated by the gold-film heater is directly proportional to local values of electrical resistance. The uniformity of electrical resistance has already been discussed in Section 2.3.2. Measured samples showed a variation of resistance of ±6.2% about the mean value, with odds of 20 to 1.

In Section 2.3.4, thermocouple calibration polynomial equations were determined to be accurate to within ±0.05°C with 20 to 1 odds. When the flat plate apparatus was assembled, the thermocouple beads were epoxied as close as possible to the centre of the 2.4 mm diameter holes. However, it is estimated that a thermocouple bead could be located as much as 1/4 of a diameter, or ±0.6 mm, from the centre of a hole. In order to minimize heat conduction from the thermocouple beads, the thermocouple lead wires were laid along the expected isotherms in the experimental apparatus.

The emissivity of the gold-film heater was determined from an energy

balance, as discussed in Section 2.3.3. It is estimated that the uncertainty in the value of the emissivity is not more than ±20%.

The thermal conductivity of air was calculated from an exponential equation which was fitted to data from the National Bureau of Standards [75]. The uncertainty associated with the use of this equation is ±0.6%. As this uncertainty is much smaller than the uncertainty of local heat flux generation by the gold-film heater, the uncertainty in calculating the thermal conductivity was not included in the calculation of an uncertainty for local Nusselt numbers.

The uncertainties in the experimental local Nusselt numbers are included in Tables 3 to 7. The uncertainties range from 9% to 13%. The major source of these uncertainties is the nonuniformity in the local resistance of the gold-film heater. The uncertainties in the emissivity of the gold-film heater and in the temperature measurements are the two other most significant sources of uncertainty in the experimental results.

The uncertainties in the modified Grashof numbers, Gr_L^*, ranges from 5% to 6% for the experiments undertaken in this work.

Repeatability of Results

Repeatability runs were performed for $Gr_L^* = 5.6 \times 10^7$ and $Gr_L^* = 2.7 \times 10^8$ after the five initial runs had been completed. The Grashof numbers for the repeated runs were within ±2% of the original Grashof numbers for both test cases. Graphs of Nusselt number, Nu_x, versus non-dimensional

distance, x/L, are presented in Figs. 19 and 20, and in tabular form in Tables 8 and 9, for the two test conditions. On the graphs, the original runs are denoted by "TRIAL 1", while the repeated runs are designated by "TRIAL 2". The experimental data points from the repeated runs fall almost perfectly on top of the data from the initial runs for both test cases.

The results of the repeatability runs indicate that: (i) the gold-film heater was not damaged at all during the initial experiments; and (ii) a high level of repeatability may be attained with the proposed gold-film technique and the corresponding experimental procedures.

CHAPTER IV

LAMINAR NATURAL CONVECTION IN A HORIZONTAL CONCENTRIC ANNULUS

4.1 PROBLEM STATEMENT

In this chapter, laminar natural convection heat transfer in the central region of a long, horizontal concentric annulus will be considered. A diagram of the problem is presented in Fig. 21.

A number of natural convection flow regimes have been found to exist for the horizontal concentric annulus geometry with constant-temperature inner and outer walls, as was discussed in Section 1.3.2. Similar flow regimes would also be expected to occur for the same geometry with a non-constant temperature boundary condition. In order to evaluate the capabilities of the gold-film technique with confidence, stable flow inside the annular region is highly desirable. This flow regime occurs for $Gr_L < 2 \times 10^5$ and $D_i/L < 1.5$ [60]. The reasons for selecting this two-dimensional, stable, laminar natural convection regime, were to simplify instrumentation requirements for the experimental work, and to reduce uncertainties and computational costs in the corresponding numerical simulations.

The three main objectives of this experiment were: (i) to use the gold-film technique to obtain local heat transfer data on a curved surface; (ii) to calculate local convection heat fluxes from the experimental data when both radiation and conduction heat transfer are significant; and (iii) to compare the experimental heat transfer results to a numerical simulation of

laminar natural convection in a horizontal concentric annulus.

The equations governing natural convection heat transfer and fluid flow in the central region of a long horizontal annulus are presented in Section 4.2. The solution method employed to solve these equations is then given. In Section 4.3, the design and description of the experimental apparatus, the test procedure followed, and the calculation of experimental results are presented. Finally, the experimental results are compared to those of corresponding numerical simulations in Section 4.4.

4.2 NUMERICAL SIMULATION

4.2.1 Governing Equations and Assumptions

The equations governing two-dimensional, steady state, laminar natural convection in a horizontal concentric annulus will be written with reference to the cylindrical coordinate system (r-θ) shown in Fig. 21. The following assumptions have been made to simplify the Navier-Stokes equations and boundary conditions: (i) the fluid is assumed to be Newtonian, and all its thermophysical properties, except density, are assumed constant; (ii) the Boussinesq approximation [67,68] is invoked; (iii) symmetry about the vertical plane passing through the centres of the concentric cylinders is assumed; and (iv) viscous dissipation is assumed to be negligible. The velocity component in the r-direction is denoted by u, and v represents the velocity component in the θ-direction. The governing equations, with these assumptions and notation, are:

r-momentum

$$\rho_o \left[u \frac{\partial u}{\partial r} + \frac{v}{r} \frac{\partial u}{\partial \theta} \right] = \mu \left[\frac{1}{r} \frac{\partial}{\partial r} \left(r \frac{\partial u}{\partial r} \right) + \frac{1}{r^2} \frac{\partial^2 u}{\partial \theta^2} \right] + \frac{\rho_o v^2}{r} \qquad (4\text{-}1)$$

$$- \mu \left[\frac{u}{r^2} + \frac{2}{r^2} \frac{\partial v}{\partial \theta} \right] - \frac{\partial p}{\partial r} + \rho g \cos(\theta)$$

θ-momentum

$$\rho_o \left[u \frac{\partial v}{\partial r} + \frac{v}{r} \frac{\partial v}{\partial \theta} \right] = \mu \left[\frac{1}{r} \frac{\partial}{\partial r} \left(r \frac{\partial v}{\partial r} \right) + \frac{1}{r^2} \frac{\partial^2 v}{\partial \theta^2} \right] - \frac{\rho_o uv}{r} \qquad (4\text{-}2)$$

$$+ \mu \left[\frac{2}{r^2} \frac{\partial u}{\partial \theta} - \frac{v}{r^2} \right] - \frac{1}{r} \frac{\partial p}{\partial \theta} - \rho g \sin(\theta)$$

energy

$$\rho_o \left[u \frac{\partial T}{\partial r} + \frac{v}{r} \frac{\partial T}{\partial \theta} \right] = \frac{k}{c_p} \left[\frac{1}{r} \frac{\partial}{\partial r} \left(r \frac{\partial T}{\partial r} \right) + \frac{1}{r^2} \frac{\partial^2 T}{\partial \theta^2} \right] \qquad (4\text{-}3)$$

continuity

$$\frac{1}{r} \frac{\partial}{\partial r} \left(ru \right) + \frac{1}{r} \frac{\partial}{\partial \theta} \left(v \right) = 0 \qquad (4\text{-}4)$$

The appropriate boundary conditions for this problem are:

$$\begin{aligned}
&\text{(i)} \quad \text{at } r = r_i: \quad u = v = 0 \; ; \quad T = T_i(\theta) \text{ given} \\
&\text{(ii)} \quad \text{at } r = r_o: \quad u = v = 0 \; ; \quad T = T_o \\
&\text{(iii)} \quad \text{at } \theta = 0^\circ: \quad \frac{\partial u}{\partial \theta} = 0 \; ; \quad v = 0 \; ; \quad \frac{\partial T}{\partial \theta} = 0 \\
&\text{(iv)} \quad \text{at } \theta = 180^\circ: \quad \frac{\partial u}{\partial \theta} = 0 \; ; \quad v = 0 \; ; \quad \frac{\partial T}{\partial \theta} = 0
\end{aligned} \qquad (4\text{-}5)$$

An explanation is required as to why the inner cylinder temperature distribution, rather than the heat flux distribution, is specified for the numerical simulation of fluid flow and heat transfer in the horizontal annulus. When the gold-film technique is employed, the measured wall temperature distribution is used to calculate the local conduction and radiation heat fluxes. Then, the local convection heat fluxes are obtained using Eq. (2-1). These local convection heat fluxes, or equivalently the local Nusselt numbers, calculated from the experimental data should match those obtained from a numerical simulation of the natural convection problem with the same specified temperature boundary condition. This is

the approach taken to compare the experimental results to the numerical simulation.

The dimensionless parameters that govern laminar natural convection in a horizontal concentric annulus may be obtained by nondimensionalizing Eqs. (4-1) to (4-4). Introducing,

$$r^* = r/D_i \;;\quad u^* = uD_i/\nu \;;\quad v^* = vD_i/\nu$$
$$T^* = (T-T_o)/(\bar{T}_i - T_o) \;;\quad P^* = P/(\rho_o \nu^2/D_i^2) \tag{4-6}$$

where a new variable, P, has been defined as follows:

$$P = p - \rho_o r g \cos(\theta) \tag{4-7}$$

The governing equations reduce to:

r-momentum

$$u^* \frac{\partial u^*}{\partial r^*} + \frac{v^*}{r^*}\frac{\partial u^*}{\partial \theta} = \left[\frac{1}{r^*}\frac{\partial}{\partial r^*}\left(r^*\frac{\partial u^*}{\partial r^*}\right) + \frac{1}{r^{*2}}\frac{\partial^2 u^*}{\partial \theta^2}\right] + \frac{v^{*2}}{r^*} - \left[\frac{u^*}{r^{*2}} + \frac{2}{r^{*2}}\frac{\partial v^*}{\partial \theta}\right] - \frac{\partial P^*}{\partial r^*} - \left(Gr^*_{D_i} T^* \cos(\theta)\right) \tag{4-8}$$

θ-momentum

$$u^* \frac{\partial v^*}{\partial r^*} + \frac{v^*}{r^*}\frac{\partial v^*}{\partial \theta} = \left[\frac{1}{r^*}\frac{\partial}{\partial r^*}\left(r^*\frac{\partial v^*}{\partial r^*}\right) + \frac{1}{r^{*2}}\frac{\partial^2 v^*}{\partial \theta^2}\right] - \frac{u^* v^*}{r^*} + \left[\frac{2}{r^{*2}}\frac{\partial u^*}{\partial \theta} - \frac{v^*}{r^{*2}}\right] - \frac{1}{r^*}\frac{\partial P^*}{\partial \theta} + \left(Gr^*_{D_i} T^* \sin(\theta)\right) \tag{4-9}$$

energy

$$u^* \frac{\partial T^*}{\partial r^*} + \frac{v^*}{r^*}\frac{\partial T^*}{\partial \theta} = \frac{1}{Pr}\left[\frac{1}{r^*}\frac{\partial}{\partial r^*}\left(r^*\frac{\partial T^*}{\partial r^*}\right) + \frac{1}{r^{*2}}\frac{\partial^2 T^*}{\partial \theta^2}\right] \tag{4-10}$$

continuity

$$\frac{1}{r^*}\frac{\partial}{\partial r^*}\left(r^* u^* \right) + \frac{1}{r^*}\frac{\partial v^*}{\partial \theta} = 0 \qquad (4\text{-}11)$$

where Gr_{D_i} is a non-dimensional Grashof number defined as follows:

$$Gr_{D_i} = \frac{g\beta\,(\bar{T}_i - T_o)\,D_i^3}{\nu^2} \qquad (4\text{-}12)$$

where $\bar{T}_i$ is the average temperature of the inner cylinder.

4.2.2 Numerical Solution

Patankar [76] has developed efficient control volume-based finite-difference calculation methods for solving fluid flow and heat transfer problems. As this reference contains a complete description of the calculation procedure for steady, two-dimensional, elliptic flows, only adaptations and certain specific details of the method employed here will be given.

General Form of the Governing Equations

The governing equations presented in Section 4.1 may be cast into the following general form:

$$\vec{\nabla} \cdot \vec{J} = S \qquad (4\text{-}13)$$

where S is a volumetric source term, and $\vec{J}$ represents the total convection and diffusion of ϕ. $\vec{J}$ is given by:

$$\vec{J} = \rho\,\vec{v}\,\phi - \Gamma\,\vec{\nabla}\,\phi \qquad (4\text{-}14)$$

where ρ is the mass density, $\vec{v}$ is the velocity vector, and ϕ is a scalar

quantity.

Integral Form of the Conservation Equations

The algebraic or discretization equations for a scalar quantity ϕ are derived by integrating the general differential equation over an appropriate control volume to obtain integral conservation equations of the form:

$$\int_{\partial V} \vec{J}\cdot\vec{n}\, ds = \int_{V} S\, dV \qquad (4\text{-}15)$$

where ∂V is the surface of the control volume, and $\vec{n}$ is the outward normal to the surface element ds. Details of the selection of control volume faces, grid point locations for ϕ, and the derivation of discretization equations will now be outlined.

Domain Discretization

The calculation domain of interest was subdivided into discrete control volumes, and main grid points were located at the centres of the control volumes. The distribution of grid points was uniform in the θ-direction, but grid points were concentrated near the inner and outer boundaries in the r-direction where the largest temperature and velocity gradients occur. The distribution of interior grid points in the r-direction was as follows:

$r_i \leq r \leq r_i + L/4$	1/3 of the interior grid points, with powerlaw distribution to concentrate grid points towards the inner boundary.

$r_i + L/4 \leq r \leq r_i + 3L/4$	1/3 of the interior grid points, with uniform grid point distribution.
$r_i + 3L/4 \leq r \leq r_o$	1/3 of the interior grid points, with powerlaw distribution to concentrate grid points towards the outer boundary.

A typical grid is shown in Fig. 22. Velocity components were calculated at staggered locations to the main grid points, as discussed by Patankar [76].

Discretization Equations

The discretization procedure for the transport term on the left-hand side of Eq. (4-15) has been discussed in detail by Patankar [76], in the context of control volume finite-difference methods. The procedure involves the prescription of a suitable locally one-dimensional profile for ϕ between neighbouring grid points. This profile depends on the relative strengths of convection and diffusion of ϕ, and it is used to approximate the convection-diffusion fluxes at control volume faces. In this work, the hybrid difference scheme [76] was used to express the combined convection-diffusion transport terms in Eq. (4-15).

The source terms in each of the governing equations must also be integrated and discretized. A method consistent with the general procedure discussed by Patankar [76] was employed.

The thermophysical fluid properties were assumed to be constant, except for the mass density in the buoyancy term of the momentum equations. The properties were evaluated at a film temperature, T_f, defined for this problem by:

$$T_f = \frac{\bar{T}_i + T_o}{2} \tag{4-16}$$

where $\bar{T}_i$ is the average inner cylinder temperature.

After algebraic approximations have been obtained for all terms in the integral conservation equations, each equation may be cast in the following general form [76]:

$$a_p \phi_p = \sum_n a_n \phi_n + b_p \tag{4-17}$$

where the summation is performed over the n nodes which neighbour point p.

The discretization equations for the scalar variables u, v, and T were developed from the r-momentum, θ-momentum, and energy equations, respectively. The pressure field is specified indirectly via the continuity equation. When the correct pressure field is substituted into the momentum equations, the resulting velocity field will also satisfy the continuity equation. In this work, the SIMPLEC algorithm, developed by Van Doormaal and Raithby [77] was used for handling this pressure-velocity coupling.

Solution of the Discretization Equations

As discussed previously, an iterative method based on the SIMPLEC algorithm was used to solve the non-linear and coupled equations. In each iteration of this procedure, the equations for u, v, p' and T were decoupled and linearized using guessed values of the dependent variables or values calculated in the previous iteration, as discussed by Patankar [76]. To ensure convergence of this iterative procedure, the implicit under-relaxation procedure of Patankar [76] was used:

$$\frac{a_p}{\alpha}\,\phi_p = \sum_n a_n\phi_n + b_p + \frac{(1 - \alpha)}{\alpha}\,a_p\phi_p^* \qquad (4\text{-}18)$$

where α is the under-relaxation parameter and ϕ_p^* is the value of ϕ at point p from the previous iteration. The under-relaxation parameter was set to 0.5 for the u and v velocity discretization equations, and 1.0 for the other equations.

In each step of the SIMPLEC procedure, a line-by-line iterative method was used to solve the nominally linear decoupled sets of algebraic equations. In this iterative procedure for each scalar variable ϕ, the equation for all the ϕ values located along one grid line are solved simultaneously using the tridiagonal matrix algorithm [71]. The best available estimate for ϕ values along neighbouring grid lines are used when solving for ϕ's along a particular grid line. After all the grid lines have been visited in this manner, one sweep of the solver is considered complete. Four sweeps in alternating directions constitutes one step of this line-by-line procedure. The maximum number of steps of the iterative equation solver, for each scalar variable ϕ, was set to 10.

The convergence of the overall SIMPLEC procedure was ascertained by monitoring the relative change in local convection heat flux at 5 points on the inner surface of the annulus. When the maximum value of the absolute relative changes in these local heat fluxes between two successive iterations was below a certain tolerance, the solution was considered to have converged. Mathematically, the convergence criteria may be represented as:

$$\left(\left| \frac{q_i^m - q_i^{m-2}}{q_i^{m-2}} \right|_{max} \right) \leq TOL \qquad (4\text{-}19)$$

where q_i is the local wall heat flux, TOL is the user-specified tolerance, and m is the current iteration number. In this work, TOL was set to 10^{-4} for most trials.

4.2.3 Numerical Test Problem

The numerical method described in Section 4.2.2 was incorporated into a general computer program. The computer program was debugged thoroughly by applying it to many test problems. The final test problem involved laminar natural convection in a horizontal annulus with constant inner- and outer-wall temperature boundary conditions. This problem has been studied both numerically and experimentally by Kuehn [22].

The concentric cylinder apparatus, constructed as a part of the experimental work, was designed for Rayleigh numbers of 10^4 to 10^5. Unfortunately, the highest Rayleigh number for which Kuehn [22] reported local Nusselt number data is 10^4. This data was used to check the results

of the computer code. The values of the non-dimensional parameters in the test case considered were: $Ra_{D_i} = 10^4$; $Pr = 0.7$; and $D_o/D_i = 2.6$. Ra_{D_i} is an average Rayleigh number based on the inner cylinder diameter, and is defined in this work as follows:

$$Ra_{D_i} = Gr_{D_i} Pr = \frac{g\beta D_i^3 (\bar{T}_i - T_o)}{\alpha \nu} \qquad (4\text{-}20)$$

A grid independence check was performed for the test problem by varying the number of grid points in the r- and θ-directions, while maintaining the grid point distribution described in Section 4.2.2. These results are presented in Table 10. Grid independence of local Nusselt number was essentially achieved with a 29 x 39 grid in the radial and angular dimensions, respectively, for a total of 1131 nodes.

A comparison between the present results, using the 29 x 39 grid, and those of Kuehn [22], are presented in Table 11. The local Nusselt number data from the two studies agree to within ±3% for all values of θ. The minor differences may be attributed mostly to the coarser grid used by Kuehn in his numerical simulations.

4.3 EXPERIMENTAL MEASUREMENTS

4.3.1 Concentric Cylinder Apparatus

Many considerations went into the design of the concentric cylinder apparatus. In Section 3.3.1, the limitations of the gold-film heater and power supply were mentioned. The other major constraints on the design were:

(1) The concentric cylinder apparatus was to be designed to produce two-dimensional, steady state, laminar natural convection air flow in the central region of the annulus.

(2) The gold coating on the heater must not be damaged when it is wrapped around the test object. This put a lower bound on the diameter of the inner cylinder. In this connection, it was noted that the gold-film heater was attached to a cylindrical object with a 50.8 mm (2 in.) diameter in a previous investigation [7].

(3) Thermocouples must be attached to the back of the gold-film heater. This task is more difficult to accomplish with an inner cylinder of small diameter.

(4) The length of the annulus required to ensure two-dimensional flow in the central region of the test section is proportional to the gap width, L, of the annulus. The gap width is defined as follows:

$$L = \left[\frac{(D_o - D_i)}{2} \right] \tag{4-21}$$

It is clear from the above constraints that the design of the concentric cylinder apparatus was a compromise between several factors. Construction of the apparatus is simplified if the dimensions of the inner cylinder are reasonably large. On the other hand, laboratory space and equipment capabilities restrict the size of the overall apparatus.

An iterative procedure was used to determine the size of the inner and

outer cylinders. For initial guessed annulus dimensions and heat flux at the surface of the inner cylinder, the fluid flow and heat transfer computer code presented in Section 4.2.2 was used to obtain an approximate inner wall temperature distribution. Then, a Grashof number based on an average temperature difference was calculated. The results of Powe et al. [60], categorizing the expected flow pattern inside an annulus in terms of the Grashof number and a non-dimensional gap width, were examined to ensure that the flow pattern in the annulus would be two-dimensional and stable. The procedure was repeated with other cylinder dimensions until the expected flow pattern was within the two-dimensional, steady flow regime, and the maximum inner cylinder temperature was less than 60°C.

The final dimensions of the inner and outer cylinder diameters were set to 38.1 mm (1 1/2 in.) and 88.9 mm (3 1/2 in.), respectively. Since a cylinder length/annulus gap ratio of at least 20 is needed to ensure two-dimensional flow in the central region of the annulus, the length of the cylinders was designed to be greater than 508.0 mm (20 in.).

The inner cylinder was fabricated from a 1828.8 mm (6 ft) long plexiglas tube, with an outer diameter of 38.1 mm (1.5 in.) and a wall thickness of 3.2 mm (1/8 in.). It was decided that the inner cylinder had to be constructed in three pieces, as shown in Fig. 23, to render the attachment of thermocouples from the inside of this cylinder as easy as possible. The thermocouples would first be epoxied to the central test section, and then two other pieces of plexiglas tubing would be joined on either side of the central section to complete the inner cylinder. To accomplish this objective, the last 3.2 mm (1/8 in.) on each end of the

108.0 mm (4 1/4 in.) long central section was machined to reduce the outer diameter by 3.2 mm (1/8 in.), as may be seen in Fig. 23. Conversely, the inner diameter of one end of two 257.2 mm (10 1/8 in.) long pieces of plexiglas tubing was increased by approximately 3.2 mm (1/8 in.) until the end pieces could slide fit into the central piece. When joined together, the total length of the inner cylinder was 609.6 mm (24 in.).

A total of 32 holes, of 2.4 mm (3/32 in.) diameter, were drilled in the test section to allow thermocouples to be attached flush with the outer surface of the inner cylinder. The locations of the thermocouples in the test section are given in Table 12. The temperature measurements were distributed between three axial locations in the central section of the inner cylinder to avoid overcrowding the thermocouples in any one cross-section of the inner cylinder. The locations were selected such that symmetry of the temperature field about the vertical plane and two-dimensionality of heat transfer in the central test section could be checked.

The procedure for attaching a thermocouple to the test section was as follows:

(1) The tip of the thermocouple was bent 90° to the lead wires.

(2) The thermocouple lead wires were taped inside the plexiglas tube, along the expected isotherm, so that the thermocouple bead could be located in the centre of the appropriate hole.

(3) The outside of the hole where the thermocouple was to be placed was covered with tape. Then, the hole was filled from the inside with epoxy (Lepage, two-part epoxy resin and hardener).

(4) The thermocouple bead was inserted into the epoxy-filled hole firmly against the tape covering the hole, and was temporarily held in place from the inside with tape. Tweezers were used to help position the thermocouple bead in the proper position.

(5) The lead wires were epoxied to the plexiglas along the expected isotherm at several locations on the inside of the tube.

(6) The epoxy was left to cure for 24 hours. Then, all of the tape employed to hold the thermocouple in position while the epoxy was hardening was removed.

Approximately 3 to 4 thermocouples could be attached to the central portion of the plexiglas inner cylinder per day. After the thermocouples had been attached to the plexiglas, the three pieces of the inner cylinder were epoxied together. Finally, a line was etched along the top of the plexiglas cylinder for use as a reference. A photograph of the instrumented inner cylinder can be seen in Fig. 23.

A 635.0 mm (25 in.) length of gold-film was cut from the sample roll to make the heater. The gold coating was protected with removable tape (3M, Scotch Brand Magic Plus), and double-sided adhesive tape (3M, Scotch Brand Tape No. Y9473) was applied to the back of the plastic sheet. A precision

cut of 609.6 mm x 122.3 mm (24 in. x 4.816 in.) was made from the central region of the gold-film sample using the cutter, as discussed in Section 2.2.2. The gold-film was then attached to the instrumented plexiglas cylinder. Again, two patient persons were needed for this job. While one person peeled the backing tape from the double-sided adhesive on the heater, the other person slowly rolled the plexiglas cylinder onto the double-sided adhesive. The etched line on the plexiglas cylinder provided a guideline for attaching the heater. After the gold-film heater was attached, a gap of aproximately 0.127 mm (0.005 in.) remained at the top of the inner cylinder. This non-heated region was placed at the top of the cylinder ($\theta = 180^{\circ}$) to minimize interruptions to the boundary layer.

The design for the inner cylinder electrodes was conceptually similar to the two-piece design used for the vertical flat plate experiment. The main modification was that a cylindrical copper piece, containing the power leads, had to be designed to clamp onto the copper tape located on the gold-film heater.

The electrodes were made from a 54.0 mm (2 1/8 in.) diameter copper rod. Each electrode was 22.2 mm (7/8 in.) long. A groove, of dimensions 31.8 mm ID x 41.3 mm OD x 6.4 mm depth (1 1/4 in. ID x 1 5/8 in. OD x 1/4 in. depth), was machined on one side of each electrode to enable the electrode to slide fit onto the inner surface of the plexiglas cylinder. A 25.4 mm (1 in.) diameter hole was drilled in the centre of each electrode for the thermocouple leads to pass through. Two semi-circular clamps, of dimensions 38.1 mm ID (nominal) x 54.0 mm OD x 6.4 mm thickness, were made for each electrode. The inner diameters of the two clamps were machined

until the clamps mated closely with the copper tape on the gold-film. A slot was machined in the radial direction on each clamp so that the clamps could be adjusted to press fit against the copper tape on the gold-film heater and then be screwed to the main copper piece. The copper electrodes, before being attached to the gold-film, may be seen in Fig. 24.

The first four steps of the electrode attachment procedure described in Section 2.3.1 were followed. The final steps are summarized below:

(5) The copper electrodes were epoxied to the plexiglas inner cylinder, and allowed to cure for 24 hours. The copper clamps were pressed against the copper tape on the gold-film heater while being screwed to the electrode.

(6) The inside of the plexiglas tube was completely filled with vermiculite insulation (VIL Vermiculite Inc., fine grade).

(7) A layer of silver-loaded paint was applied around the region where the copper clamps contacted the copper tape.

(8) The protective tape was removed from the gold-film heater.

A photograph of a completed electrode is shown in Fig. 25.

The diameter of the inner cylinder after attaching the gold-film heater was 38.9 mm (1.533 in.), and the electrode separation was 563.6 mm (22 3/16 in.). A photograph of the completed inner cylinder assembly may be seen in

Fig. 26.

The outer cylinder was fabricated from a 609.6 mm (24 in.) long, schedule 40, aluminum pipe. The nominal inner and outer diameters of the pipe are 90.1 mm and 101.6 mm (3.548 in. and 4.0 in.), respectively. The outside of the outer cylinder was machined on a lathe to eliminate out-of-roundness. Approximately 12.7 mm (1/2 in.) at the ends of the cylinder were also bored to eliminate out-of-roundness. The inside of the pipe was polished with a fine grade emery paper. Finally, a flat black spray paint (Pascal Inc., Premium Enamel Spray Paint) was applied to the inner surface of the pipe so that the emissivity of the outer surface of the annulus would be approximately equal to unity.

Two aluminum flanges, having dimensions of 101.6 mm (4 in.) ID (nominal), 139.7 mm (5 1/2 in.) OD and a thickness of 6.4 mm (1/4 in.), were constructed. The inner diameter on each flange was bored until the flanges fit tightly onto the ends of the outer cylinder. The flanges were then carefully welded to the outer cylinder.

The inner cylinder was held in the centre of the outer cylinder with two plexiglas end plates, which are shown in Fig. 24. The dimensions of the end plates are 54.0 mm (2 1/8 in.) ID, 139.7 mm (5 1/2 in.) OD and 22.2 mm (7/8 in.) thickness. On one side of each end plate, a 6.4 mm (1/4 in.) length was turned down until the end plates fit tightly into the end of the outer cylinder. Holes were drilled through the end plate and flange so the pieces could be bolted together.

A total of eight thermocouples were attached to the outside surface of the outer cylinder, at the same three axial locations used for the inner cylinder measurements, using a high thermal conductivity epoxy adhesive (Omega, Omegabond 101). Four thermocouples were installed in the central cross section, at 90° intervals, while two thermocouples, separated by 180°, were attached at each of the other two measurement locations.

The outer cylinder was maintained at a constant temperature in these experiments by circulating a fluid through copper tubing wrapped around it. First, a layer of high thermal conductivity paste (Omega, Omegatherm 201) was painted onto the outside surface of the outer cylinder. Then, two 15.2 m (50 ft) rolls of 9.5 mm (3/8 in.) OD copper tubing were tightly wrapped around the outer cylinder in a double helix pattern. A 50/50 mixture of distilled water and antifreeze was pumped in a counterflow arrangement through these two copper tubes. The fluid was maintained at a constant temperature by a waterbath (Canlab, Model W3241-4), which has a fluid capacity of 22.0 l (4.8 Imp. gal.). The unit contains an 800 W heater, and a temperature controller which is accurate to ±0.1°C over a temperature range of 15°C to 95°C.

A centrifugal pump (Cole-Parmer Instrument Co., Cat No. J-7022-20) circulated a distilled water/anti-freeze mixture through the copper tubes wrapped around the outer cylinder. The pump has a maximum flowrate of 36.8 l (10 U.S. gpm) at 3000 rpm.

The concentric cylinder apparatus was assembled and placed into a plexiglas box. The plexiglas box was placed on a steel channel, fitted

with levelling screws. Fiberglas insulation was placed over the ends of the cylinder to reduce heat losses through the electrodes and the plexiglas end plates. The entire concentric cylinder apparatus is shown in Fig. 27.

4.3.2 Test Procedure

Five experimental runs were performed with average gold-film heat fluxes of 25, 50, 75, 100 and 125 W/m^2. The outer cylinder temperature was maintained at 25°C for all runs.

The Rayleigh numbers, Ra_{D_i}, for the five experimental runs were 2.97×10^4, 5.04×10^4, 6.83×10^4, 8.41×10^4, and 9.88×10^4. Repeatability runs were performed for all of the test cases, but only those for the lowest and highest Rayleigh numbers will be presented in this thesis.

The same data acquisition program employed to take the measurements for the vertical flat plate experiment was used in this study. For each experimental run, the data acquisition program monitored the local gold-film temperatures for at least 6 hours after the power supply to the heater had been turned on and set. This was enough time to ensure that steady state conditions had prevailed for at least 3 hours. In these experiments, the average outer cylinder temperature varied by about ±0.02°C after steady state had been achieved. A maximum variation in the outer cylinder temperature of ±0.13°C about the mean value occured with a Rayleigh number of 9.88×10^4. The temperature variations about the mean outer cylinder temperature were lower for the runs with lower Rayleigh numbers.

4.3.3 Calculation of Conduction Heat Flux

In Section 2.1, an energy balance at the surface of the gold-film heater was written. The conduction heat flux, inside the test object to which the heater is attached, is one of the terms in this energy balance. The vertical flat plate experiment, presented in Chapter 3, was designed so that this conduction heat transfer would be negligible. It is either impractical or impossible to reduce heat conduction in many experiments to a low enough rate so that it may be neglected. Therefore, a procedure for obtaining the conduction heat flux must be developed. In this thesis, a numerical simulation of conduction heat transfer inside the plexiglas tube, using the experimental temperatures measured at the surface of the gold-film heater as a boundary condition, was utilized to calculate local conduction heat fluxes.

The equation governing two-dimensional, steady state, heat conduction inside the plexiglas inner tube, and in the vermiculite insulation inside it, is:

$$\frac{1}{r}\frac{\partial T}{\partial r}\left[kr\frac{\partial T}{\partial r}\right] + \frac{1}{r^2}\frac{\partial}{\partial \theta}\left[k\frac{\partial T}{\partial \theta}\right] = 0 \qquad (4\text{-}22)$$

It should be noted that plexiglas and vermiculite have different values of thermal conductivity. The appropriate boundary conditions for this problem are:

$$\begin{aligned} &\text{(i)} \quad \text{at } r = r_i: && T = T_i(\theta) \text{ given} \\ &\text{(ii)} \quad \text{at } r = 0: && \frac{\partial T}{\partial r} = 0 \\ &\text{(iii)} \quad \text{at } \theta = 0^\circ: && \frac{\partial T}{\partial \theta} = 0 \end{aligned} \qquad (4\text{-}23)$$

(iv) at $\theta = 180^{\circ}$: $\frac{\partial T}{\partial \theta} = 0$

A diagram of the heat conduction problem is shown in Fig. 28. The temperature distribution at $r = r_i$, $T_i(\theta)$, is obtained by using cubic splines to interpolate experimentally measured temperatures at discrete points on the outer boundary of the inner cylinder.

Eq. (4-22) represents a special case of Eq. (4-15), where $\vec{v}$ and S are equal to zero. The procedure for solving this equation has been presented in detail by Patankar [76]. In this section, only problem-specific details of the method employed here will be given.

The entire volume of interest was divided into discrete control volumes. The distribution of grid points for the heat conduction calculations was uniform in the θ-direction, and this distribution was picked so that the experimental heat transfer results would be determined at the same points as those in the numerical simulation of natural convection in the annulus, which was discussed in Section 4.2.2. In the r-direction, a uniform distribution of control volumes was employed inside the plexiglas wall. The control volumes were twice as large inside the vermiculite near the plexiglas-vermiculite boundary, and four times as large in the central region of the inner cylinder, as those inside the plexiglas wall. A half control-volume was used in the r-direction at the outer boundary to improve the accuracy of the boundary heat flux determination [76]. This type of grid has been discussed by Patankar [76], and is called a "Type A" grid. A diagram of this domain discretization is given in Fig. 29.

Discretization equations for calculating the temperature at each grid point were generated by suitably adding up algebraic approximations for each term in the integral conservation equations [76]. The thermal conductivities of plexiglas and vermiculite were assumed to be constant, and equal to 0.195 W/m^2 [78] and 0.068 W/m^2 [67], respectively. The heat fluxes at the interface between the two materials were calculated using the harmonic-mean procedure recommended by Patankar [76]. The iterative line-by-line tridiagonal matrix algorithm, discussed in Section 4.2.2, was used to solve the linear, coupled equations.

Convergence of the equation solver was ascertained by monitoring the relative change in local conduction heat flux at all points on the outer boundary. The following criteria was used:

$$\left(\left| \frac{q_{cnd_i}^{m} - q_{cnd_i}^{m-10}}{q_{cnd_i}^{m-10}} \right|_{max} \right) \leq 10^{-4} \qquad (4\text{-}24)$$

where the superscripts represent the step number of the iterative equation solver.

The numerical method described in this section was incorporated into a two-dimensional heat conduction program. The computer program was debugged thoroughly by applying it to several test problems. It was then used to calculate the conduction heat flux, q_{cnd_i}, on the outer surface of the inner cylinder, for all five experimental runs considered in this work.

4.3.4 Calculation of Convection Heat Flux

The local convection heat flux at the surface of the gold-film heater is given by:

$$q_{conv_i} = q_e - q_{rad_i} - q_{cnd_i} \tag{4-25}$$

In order to estimate the radiation heat flux, consider the concentric cylinders as a two-surface enclosure. This is a reasonable assumption for this experimental apparatus because the radiation shape factor between the central portion of the test section of the inner cylinder and the plexiglas end-plates is very small. Assuming that the two surfaces are diffuse and gray, the net radiation heat flux leaving the inner cylinder is given by:

$$q_{rad_i} = \frac{\sigma \left(T_i^4 - T_o^4 \right)}{\frac{1}{\varepsilon_i} + \frac{1 - \varepsilon_o}{\varepsilon_o} \left[\frac{r_i}{r_o} \right]} \tag{4-26}$$

where ε_i is the emissivity of the gold-film heater and ε_o is the emissivity of the outer cylinder.

In this experiment, the outer cylinder was painted flat black so that its emissivity could be assumed equal to unity. Thus, Eq. (4-26) may be simplified in this problem to the following:

$$q_{rad_i} = \varepsilon_i \sigma \left(T_i^4 - T_o^4 \right) \tag{4-27}$$

Substituting Eq. (4-27) into Eq. (4-25), the convection heat flux is calculated by:

$$q_{conv_i} = q_e - q_{cnd_i} - \varepsilon_i \sigma \left(T_i^4 - T_o^4 \right) \tag{4-28}$$

The conduction heat flux, q_{cnd_i}, was calculated using the numerical

procedure discussed in Section 4.3.3.

4.4 PRESENTATION AND DISCUSSION OF RESULTS

4.4.1 Establishment of Two-Dimensionality of Heat Transfer

The experimental apparatus was designed with a large ratio of inner cylinder length to annulus gap width so that three-dimensional end-effects could be neglected in the central test section region. This assumption of two-dimensionality of heat transfer in the region of the test section was verified during the experiments.

Graphs of temperature versus axial distance from the centre of the test section are presented in Figs. 30 and 31 for the test cases with $Ra_{D_i} = 2.97 \times 10^4$ and $Ra_{D_i} = 9.88 \times 10^4$, respectively. Note that the temperature measurements taken at $\theta = -90^\circ$ and $\theta = 90^\circ$ have been superimposed on the graph for each axial location.

The horizontal lines on the graphs, for each of the three values of θ, indicate that the temperature was essentially constant with axial position in the central region of the test section. The maximum difference in the average temperatures at the three axial locations was less than $0.06^\circ C$ for each of the two test cases. This indicates that the heat transfer was essentially two-dimensional in the central region of the annulus.

4.4.2 Establishment of Symmetry of Heat Transfer

The ability of the gold-film heater to generate a symmetrical temperature field about the vertical plane passing through the central axis of the two cylinders is discussed in this section of the thesis.

The thermocouple locations in the test section, given in Table 12, were selected so that the assumption of symmetry of heat transfer could be checked at the three main measurement locations on the inner cylinder. For the test cases of $Ra_{D_i} = 2.97 \times 10^4$ and $Ra_{D_i} = 9.88 \times 10^4$, temperature profiles on both sides of the vertical plane are plotted as a function of θ, in Figs. 32 and 33, and have been labeled "LEFT SIDE" and "RIGHT SIDE".

The temperatures on the left-hand side of the vertical plane are slightly higher for each of the two test cases. The maximum temperature difference between two corresponding symmetrical positions on the heater was 0.21°C for the $Ra_{D_i} = 9.88 \times 10^4$ test case at $\theta = 75°$. However, as this difference is not much greater than the uncertainty of the temperature measurements, the assumption of symmetry of heat transfer about the vertical plane passing through the central axis of the two cylinders is reasonable.

Averaged values of the temperature readings at symmetrical θ locations were used in the calculations of the local Nusselt number results.

4.4.3 Establishment of Grid Independence of Natural Convection Computations

Converged solutions to the equations governing heat transfer and fluid flow in the horizontal annulus were obtained using the computational procedure presented in Section 4.2.2, with five different grids. The grid independence checks were done for the highest Rayleigh number test case, namely $Ra_{D_i} = 9.88 \times 10^4$, because the largest temperature gradients were expected to occur with this run.

For a grid point spacing in the θ direction of less than 15°, the experimental data must be interpolated to provide temperatures at boundary nodes which do not coincide with the experimental data points. A cubic-spline routine was used to interpolate between experimental data points. This is the same procedure that was used for interpolating data for the heat conduction computations, as mentioned in Section 4.3.3.

The results of the grid independence check are summarized in Table 13. Grid independence of local Nusselt number was achieved with 38 grid points in the radial direction and 75 points in the angular direction, for a total of 2850 nodes.

4.4.4 Establishment of Grid Independence of Heat Conduction Computations

A grid independence check was also performed on the heat conduction computer program for the test case of $Ra_{D_i} = 9.88 \times 10^4$. In this check, the total number of grid points in the r-direction was varied, while

maintaining the radial grid point distribution discussed in Section 4.3.3. A uniform grid point distribution was employed in the θ-direction, to be consistent with the grid used for the natural convection computations. The grid independence results are presented in Table 14.

Grid independence of local conduction heat flux was achieved to within 0.5% with 102 grid points in the r-direction. In the θ-direction, changes of up to 1% in local conduction heat flux were observed when increasing the number of grid points in the angular direction from 39 to 75, while maintaining 102 grid points in the radial direction. A 102 x 75 point (r,θ) grid was used for the final heat conduction computations.

4.4.5 Local Nusselt Numbers

Results

A brief description of the expected shape of the local Nusselt number versus angular position graphs will be given before the final results are presented.

For the horizontal concentric annulus experiment, the air density gradients produced by the heated inner cylinder, in conjunction with the gravitational field, create buoyancy forces in the hot air next to the inner cylinder. This causes the air to rise up the inner cylinder. Similarly, the cooled outer cylinder produces density gradients in the air next to the outer cylinder. These gradients, in conjunction with the gravitational field, create a downward flow of cool air next to the outer

cylinder. The flow pattern described above is two-dimensional, and is stable for $10^4 < Ra_{D_i} < 10^5$ [60].

Plots of the experimentally measured inner cylinder surface temperature versus angular position have already been presented in Figs. 32 and 33. These plots show that the inner cylinder surface temperature is lowest at $\theta = 0^\circ$, and then increases only slightly for $0^\circ < \theta < 60^\circ$. The temperature rise is substantially higher over the remaining portion of the heated inner cylinder.

Local Nusselt numbers were calculated using the following equation:

$$Nu_{D_i} = \left[\frac{q_e - \varepsilon_i \sigma (T_i^4 - T_o^4) - q_{cnd_i}}{(T_i - T_o)} \right] \left[\frac{D_i}{k} \right] \qquad (4\text{-}29)$$

Since the local Nusselt number is inversely proportional to the difference between the local heater temperature and the outer cylinder temperature, local Nusselt numbers should start out highest at $\theta = 0^\circ$, decrease slightly for $0^\circ < \theta < 60^\circ$, and decrease most rapidly near the top of the heated cylinder.

Graphs of local Nusselt number are plotted as a function of θ, for $Ra_{D_i} = 2.97 \times 10^4$ and $Ra_{D_i} = 9.88 \times 10^4$ in Figs. 34 and 35, respectively. The experimental results are indicated with discrete points, while the numerical results are represented by a continuous curve. The numerical results were obtained from computer simulations of natural convection in the annulus. In these simulations, the temperature distribution at the surface of the inner cylinder, $T = T_i(\theta)$ at $r = r_i$, was taken from the experimental temperature data. A cubic spline routine was used to interpolate between experimental data points, as required.

The numerical and experimental results agree to within the experimental uncertainties for $0^\circ \leq \theta \leq 150^\circ$. However, the experimental local Nusselt numbers are higher at $\theta = 180^\circ$ than at $\theta = 165^\circ$. This is in direct contrast to the numerical results, which use the experimentally-measured inner cylinder surface temperatures as a boundary condition. Also, observing the local temperature data, the inner cylinder surface temperature does not rise significantly from $\theta = 165^\circ$ to $\theta = 180^\circ$. Physically, the inner cylinder surface temperature should increase continuously from $\theta = 0^\circ$ to $\theta = 180^\circ$.

The unexpected experimental results for $165^\circ \leq \theta \leq 180^\circ$ are probably due to the fact that the 0.127 mm (0.005 in.) gap in the gold-film heater, at the top of the inner cylinder, occurs directly at the location of a thermocouple. Thus, the inner cylinder surface temperature in the vicinity of $\theta = 180^\circ$ is depressed because there is no heat generation in this region. In order to minimize the effect of this problem on the other results, it was decided that the experimentally-measured inner cylinder surface temperature at $\theta = 180^\circ$ should be discarded.

A physically realistic inner cylinder surface temperature at $\theta = 180^\circ$ was obtained by extrapolating the experimental temperature data from $135^\circ \leq \theta \leq 165^\circ$. A cubic polynomial was developed to perform this task. The cubic polynomial may be expressed as follows:

$$T_i(\theta) = C_0 + C_1\theta + C_2\theta^2 + C_3\theta^3 \qquad (4\text{-}30)$$

where C_0, C_1, C_2, and C_3 are polynomial coefficients. Four conditions are

required to obtain the coefficients for the cubic extrapolation. Three of the conditions are that the polynomial equation must pass through the data points at $\theta = 135^\circ$, 150°, and 165°. The final condition imposed was that the temperature gradient must be zero at $\theta = 180^\circ$. This arises from the assumption of symmetry about the vertical plane, which was verified in Section 4.4.2.

The experimental and numerical results of local Nusselt number versus θ for the five test cases, using an extrapolated temperature at $\theta = 180^\circ$, are presented graphically in Figs. 36 to 40, and also in Tables 15 to 19. The temperatures at $\theta = 180^\circ$* in the tables are the raw temperature data, without the aforementioned cubic extrapolation. The experimental local Nusselt numbers are within 8.8% of the numerical results for $0^\circ \leq \theta \leq 150^\circ$ for all five test cases. At $\theta = 165^\circ$, the experimental results are consistently higher than the numerical results, by 30% to 37%. However, the experimental results and the numerical results only differ by approximately 10% at $\theta = 180^\circ$. More important is the fact that the experimental results now follow the same trend as the numerical results, and are physically realistic.

The breakdown of radiation, conduction, and convection heat fluxes for the five test cases are shown in Tables 15 to 19. Conduction heat transfer only acts to redistribute the heat generated in the gold-film heater. Heat is transferred into the plexiglas tube at the top of the inner cylinder, from $120^\circ < \theta < 180^\circ$. This heat is transferred to air at the bottom half of the inner cylinder. Conduction heat transfer is most significant from $165^\circ \leq \theta \leq 180^\circ$. At $\theta = 165^\circ$, 21% of the generated heat is transferred

into the plexiglas for the $Ra_{D_i} = 2.97 \times 10^4$ test case. Radiation heat transfer from the inner cylinder to the outer cylinder, on the other hand, accounts for 18% to 25% of the total heat transfer at the surface of the gold-film heater.

Uncertainty Analysis

The uncertainties related to local heat flux generation, temperature measurements, and the emissivity of the gold-film heater were discussed in Section 3.4.2, with reference to the vertical flat plate experiment. In this section, the uncertainties associated with the Rayleigh numbers, the location of the temperature measurements, and the calculation of the conduction heat flux are described. Then, the uncertainties in the local Nusselt numbers will be presented.

The Rayleigh number for these experiments was defined in Eq. (4-20). The uncertainties associated with the calculation of the Rayleigh numbers are due primarily to the uncertainties in the average inner and outer cylinder temperatures. The uncertainties in the Rayleigh numbers are shown in Tables 15 to 19, and are approximately ±1% of the calculated values.

The local Nusselt numbers were calculated at locations where the temperature measurements were taken. The thermocouples used to take these temperature measurements were epoxied as close as possible to the centres of the 2.4 mm holes drilled in the plexiglas tube. However, it is estimated that a thermocouple bead could be as much as ±0.6 mm from the centre of a hole. This distance represents an angular error of ±1.8°.

The uncertainties in the heat conduction computations are hard to ascertain precisely. Uncertainties in the experimental temperature measurements due to the calibration procedure and the accuracy of the voltmeter were quantified in Section 2.3.4. The numerical errors are due to not having completely grid-independent solutions. These errors were quantified in Section 4.4.4 as being less than 1%.

Contributions to the uncertainties in conduction heat flux that have been analyzed include the uncertainties in temperature measurement and in the estimation of the thermal conductivity of the plexiglas tube and vermiculite insulation. The former was accomplished by defining an average conduction heat flux inside the plexiglas tubing as:

$$\left|\bar{q}_{cnd}\right| = k_i \frac{(T_{i,h} - T_{i,c})}{\frac{\pi}{2} D_i} \qquad (4\text{-}31)$$

where $T_{i,h}$ and $T_{i,c}$ are the maximum and minimum inner cylinder temperatures. The uncertainty in this average conduction heat flux was assumed to apply everywhere.

The influence of uncertainties in the thermal conductivities of plexiglas and vermiculite on the experimental local Nusselt numbers were demonstrated by independently varying the values of the thermal conductivity of plexiglas, by ±5%, and vermiculite by, ±10%. These results are shown in Figs. 41 and 42, respectively. They show that the effect of these uncertainties of 5% to 10% in the thermal conductivities of the test object components is insignificant in the calculation of the local Nusselt numbers.

The final uncertainties for the local values of Nusselt number are included in Tables 15 to 19. These uncertainties range from 9% to 20%. The major contributions to these uncertainties are the nonuniformities in the resistance of the gold-film heater, the uncertainty in the value of the emissivity of the gold-film, and the uncertainties in the calculation of local conduction heat fluxes.

Repeatability of Results

Repeatability runs were performed for the test cases with $Ra_{D_i} = 2.97 \times 10^4$ and $Ra_{D_i} = 9.88 \times 10^4$. These results are shown in Figs. 43 and 44, and in tabular form in Tables 20 and 21. The Rayleigh numbers for the repeated runs were within ±3% of the original Rayleigh numbers. In these figures and tables, the original runs are designated as "TRIAL 1", and the repeated runs are designated as "TRIAL 2". The experimental data points from the repeated runs fall within ±6% of those from the original runs for both test cases. This agreement in results between the original runs and the repeated runs is well within the experimental uncertainties.

CHAPTER V

CONCLUSIONS AND RECOMMENDATIONS

5.1 REVIEW OF THE THESIS

A synopsis of the published literature pertaining to local heat transfer measurement techniques was presented in Section 1.2. This showed that a gold-film technique has successfully been employed in various *forced* convection and ***boiling*** heat transfer studies to provide local heat transfer data. The accuracy of the gold-film technique is comparable to many of the other available techniques for taking local heat transfer measurements, and the instrumentation and equipment required to use the technique are commercially-available and relatively inexpensive to purchase. The gold-film technique is ideally suited for complementary flow visualization studies because the gold-film heater used in the technique is about 80% transparent to visible light.

The work presented in this thesis was undertaken to determine if the gold-film technique can be used to obtain accurate local heat transfer measurements in ***natural*** convection problems. As the rates of heat transfer due to natural convection are typically much smaller than those associated with boiling or forced convection heat transfer, wall conduction and radiation heat transfer must be accounted for in the gold-film technique. The development of a procedure for determining the local conduction and radiation heat fluxes was one of the major goals of this work.

A detailed description of the proposed gold-film technique was

presented in Section 2.1. This was followed by a discussion of the development of a two-step design for attaching electrodes to the gold-film. Measurements of the uniformity of the resistance of the gold-film were undertaken. Results of 60 resistance measurements on 25.4 mm square samples of the gold-film produced an average resistivity of 13.54 Ω/sq., and a standard deviation of 3.1%. The thermocouples used for temperature measurements were individually calibrated against an accurate quartz thermometer in a waterbath from 18°C to 74°C. Fourth-order polynomial equations were fitted to the data. Calibration checks indicated that the polynomial equations were accurate to within ±0.05°C for 95% of the temperature measurements.

An apparatus was designed and constructed to take measurements of two-dimensional, steady state, laminar natural convection along a vertical flat plate. Five experimental runs were performed with modified Grashof numbers ranging from 5.6×10^7 to 2.7×10^8. The uncertainties in the Grashof numbers were 5% to 6%, while the uncertainties in the experimental values of local Nusselt number were typically 9% to 13%. The two-dimensionality of heat transfer at the measurement locations was verified.

A similarity solution of the differential equations governing laminar natural convection along a vertical flat plate was obtained for a constant surface heat flux boundary condition and a Prandtl number of 0.7, using an iterative finite-difference method. The similarity analysis was presented by Sparrow and Gregg [47], but numerical solutions were only given in their work for Prandtl numbers of 0.1, 1.0, 10.0 and 100.0.

In the vertical flat plate experiments, radiation heat transfer from the gold-film heater to the constant temperature box accounted for 18% to 22% of the heat generated in the gold-film. Conduction heat transfer was minimized in this experiment to maintain a nearly-constant convection heat flux at the surface of the vertical flat plate. Graphs of Nusselt number versus x/L were plotted for the five test cases. The differences between the experimental and numerical results were generally less than 9% for all five test cases over the region $1/6 \leq x/L \leq 1$. The overestimation of the local Nusselt numbers for $1/24 < x/L < 1/6$ was anticipated, as longitudinal heat conduction at the bottom of the plate was not accounted for in the experimental work. Repeatability of the experimental local Nusselt numbers was to within ±0.5%.

An experimental apparatus was also designed and constructed for investigating laminar natural convection heat transfer in the central region of a long, horizontal concentric annulus. Five experimental runs were performed with Rayleigh numbers ranging from 2.97×10^4 to 9.88×10^4. The uncertainties in the Rayleigh numbers were approximately ±1%. Test runs verified the two-dimensionality and symmetry of heat transfer in the central region of the annulus.

A numerical simulation of two-dimensional, laminar natural convection inside the horizontal concentric annulus was performed using a control volume finite-difference calculation procedure [76]. The computer program was debugged thoroughly, and applied to several test problems with known solutions. Numerical solutions were then obtained for the five test cases using the experimentally-measured inner cylinder temperature distributions

as boundary conditions.

In the horizontal concentric annulus experiments, the experimentally-determined local Nusselt numbers were within ±9% of the numerical results for $0^\circ \leq \theta < 150^\circ$, for all five test cases. Larger discrepancies between the experimental and numerical results were observed for $150^\circ \leq \theta \leq 180^\circ$. Radiation to the outer cylinder accounted for 18% to 25% of the total heat transfer from the gold-film heater. Wall conduction was a significant mode of heat transfer at the top and bottom of the heater, accounting for up to 21% of the local heat transfer at $\theta = 165^\circ$. The repeatabilty of the local Nusselt numbers was within ±6%.

5.2 SUGGESTIONS FOR IMPROVEMENTS AND EXTENSIONS

The results obtained with the proposed gold-film technique for taking local natural convection heat transfer data were quite encouraging. It is felt that it would be worthwhile to continue the development of the gold-film technique with a goal of reducing the experimental uncertainties. The three largest sources of uncertainty in the proposed gold-film technique are due to: (i) local non-uniformities in the resistance of the gold-film; (ii) the uncertainty in the value of the emissivity of the gold-film; and (iii) the uncertainties in determining conduction heat fluxes.

The calibration of gold-film heaters to determine the local electrical resistance has already been done using liquid crystal sheets [2]. This procedure could be incorporated in future applications of the proposed gold-film technique. Secondly, the radiation properties of several samples of

gold-film should be measured in order to accurately determine the emissivity of the gold-film. As the equipment needed to do this is not available at McGill University, the possibility of using a suitable apparatus at the National Research Council of Canada or at a U.S. Government laboratory should be explored. Thirdly, the use of finer-gauge thermocouples than the ones used in this work would serve the dual-purpose of reducing the uncertainty in positioning thermocouples and in decreasing the associated uncertainties in calculating the conduction heat fluxes.

It is recommended that the gold-film technique be evaluated as a potential technique for taking local turbulent natural convection heat transfer measurements. The successful completion of this project would establish the gold-film technique as a convenient and effective way of measuring local heat transfer coefficients in natural, forced, and mixed convection problems, with laminar and turbulent fluid flow.

REFERENCES

1. Oker, E. and Merte, H., "Semi-Transparent Gold Film as Simultaneous Surface Heater and Resistance Thermometer for Nucleate Boiling Studies", *J. Heat Transfer*, Trans. ASME, Vol. 103, pp. 65-68, 1981.

2. Hippensteele, S.A., Russell, L.M. and Stepka, F.S., "Evaluation of a Method for Heat Transfer Measurements and Thermal Visualization Using a Composite of a Heater Element and Liquid Crystals", NASA TM 81639, 1981.

3. Hippensteele, S.A., Russell, L.M. and Torres, F.J., "Local Heat-Transfer Measurements on a Large Scale-Model Turbine Blade Airfoil Using a Composite of a Heater Element and Liquid Crystals", *J. Engineering for Gas Turbines and Power*, Trans. ASME, Vol. 107, pp. 953-960, 1985.

4. Hippensteele, S.A., Russell, L.M. and Torres, F.J., "Use of a Liquid-Crystal, Heater-Element Composite for Quantitative, High-Resolution Heat Transfer Coefficients on a Turbine Airfoil, Including Turbulence and Surface Roughness Effects", NASA TM 87355, 1987.

5. Simonich, J.C. and Moffat, R.J., "New Technique for Mapping Heat-Transfer Coefficient Contours", *Review Scientific Instrumentation*, Vol. 53, pp. 678-683, 1982.

6. Simonich, J.C. and Moffat, R.J., "Liquid Crystal Visualization of Surface Heat Transfer on a Concavely Curved Turbulent Boundary Layer", *J. Engineering for Gas Turbines for Power*, Trans. ASME, Vol. 106, pp. 619-627, 1984.

7. Baughn, J.W., Hoffman, M.A., Launder, B.E. and Takahashi, R.K., "Turbulent Heat Transport in Circular Ducts With Circumferentially Varying Heat Flux", *J. Heat Transfer*, Trans. ASME, Vol. 106, pp. 64-70, 1984.

8. Baughn, J.W., Hoffman, M.A., Launder, B.E. and Takahashi, R.K., "Local Heat Transfer Downstream of an Abrupt Expansion", *J. Heat Transfer*, Trans. ASME, Vol. 106, pp. 789-796, 1984.

9. Baughn, J.W., Takahashi, R.K., Hoffman, M.A. and McKillop, A.A., "Local Heat Transfer Measurements Using an Electrically Heated Thin Gold-Coated Plastic Sheet", *J. Heat Transfer*, Trans. ASME, Vol. 107, pp. 953-959, 1985.

10. Baughn, J.W., Elderkin, M.J. and McKillop, A.A., "Heat Transfer from a Single Cylinder, Cylinders in Tandem, and Cylinders in the Entrance Region of a Tube Bank with Uniform Heat Flux", *J. Heat Transfer*, Trans. ASME, Vol. 108, pp. 386-391, 1986.

11. Eckert, E.R.G. and Goldstein, R.J., *Measurements in Heat Transfer*, 2nd Edition, McGraw-Hill Book Company, New York, 1970.

12. Thompson, W.P., "Heat Transfer Gages", in *Methods of Experimental Physics*, edited by Emrich, R.J., Vol. 18, Part B, Academic Press, New York, 1981.

13. Gardon, R., "A Transducer for the Measurement of Heat-Flow Rate", *J. Heat Transfer*, Trans. ASME, Vol. 82, pp. 396-398, 1960.

14. Newman, L.B., Sparrow, E.M. and Eckert, E.R.G., "Free Stream Turbulence Effects on Local Heat Transfer from a Sphere", *J. Heat Transfer*, Trans. ASME, Vol. 94, pp 7-16, 1972.

15. Kraabel, J.S., Baughn, J.W. and McKillop, A.A., "An Instrument for the Measurement of Heat Flux from a Surface with Uniform Temperature", *J. Heat Transfer*, Trans. ASME, Vol. 102, pp. 576-578, 1980.

16. Shewen, E.C., Hollands, K.G.T. and Raithby, G.D., "The Measurement of Surface Heat Flux using the Peltier Effect", from *Developments in Experimental Techniques in Heat Transfer and Combustion*, ASME Publication No. HTD-Vol 71, New York, 1987.

17. Bryant, L.W., Ower, E., Halliday, A.S. and Falkner, V.M., "On the Convection of Heat from the Surface of an Aerofoil in a Wind Current", *Aero. Research Committee*, R.M. No. 1162, 1928.

18. Hauf, W. and Grigull, U., "Optical Methods in Heat Transfer", in *Advances in Heat Transfer*, edited by Hartnett, J.P. and Irvine, T.F., Vol. 6, pp. 134-366, Academic Press, New York, 1970.

19. Eckert, E.R.G. and Soehngen, E.E., "Studies on Heat Transfer in Laminar Free Convection with the Zehnder-Mach Interferometer", USAF Tech. Report 5747, 1948.

20. Eckert, E.R.G. and Soehngen, E.E., "Interferometric Studies on the Stability and Transition to Turbulence of a Free Convection Boundary Layer", *Proc. Gen. Discuss. Heat Transfer* ASME-IME, London, 1951.

21. Kuehn, T.H. and Goldstein, R.J., "An Experimental and Theoretical Study of Natural Convection in the Annulus between Horizontal Concentric Cylinders", *J. Fluid Mechanics*, Vol. 74, pp. 695-719, 1976.

22. Kuehn, T.H., "Natural Convection Heat Transfer from a Horizontal Circular Cylinder to a Surrounding Cylindrical Enclosure", Ph.D. Thesis, University of Minnesota, 1976.

23. Goldstein, R.J. and Chiang, H.D., "Measurements of Temperature and Heat Transfer", Chapter 12 in *Handbook of Heat Transfer Applications*", McGraw-Hill Book Company, New York, 1985.

24. Saboya, F.E.M. and Sparrow, E.M., "Local and Average Transfer Coefficients for One-Row Plate Fin and Tube Heat Exchanger Configurations", *J. Heat Transfer*, Trans. ASME, Vol. 96, pp. 265-272, 1974.

25. Cur, O.N., "Experiments on Heat Transfer and Pressure Drop for an Array of Colinear Interrupted Plates", Ph.D. Thesis, University of Minnesota, 1978.

26. Krieth, K., Taylor, J.H. and Chong, J.P., "Heat and Mass Transfer from a Rotating Disk", *J. Heat Transfer*, Trans. ASME, Vol. 82, pp. 53, 1960.

27. Goldstein, R.J., Sparrow, E.M. and Jones, D.C., "Natural Convection Mass Transfer Adjacent to Horizontal Plates", *Int. J. Heat Mass Transfer*, Vol. 16, pp. 1025-1035, 1973.

28. Mizushina, T., "The Electrochemical Method in Transport Phenomena", in *Advances in Heat Transfer*, edited by Hartnett, J.P. and Irvine, T.F., Vol. 7, pp. 87-161, Academic Press, New York, 1971.

29. Lloyd, J.R., Sparrow, E.M. and Eckert, E.R.G., "Local Natural Convection Mass Transfer Measurements", *J. Electrochemical Society*, Vol. 119, pp. 702-707, 1972.

30. Lloyd, J.R., Sparrow, E.M. and Eckert, E.R.G., "Laminar, Transition and Turbulent Natural Convection Adjacent to Inclined and Vertical Surfaces", *Int. J. Heat Mass Transfer*, Vol. 15, pp. 457-473, 1972.

31. Eagle, A. and Ferguson, R.M., "The Coefficients of Heat Transfer from Tube to Water", *Proc. Instn. Mech. Engrs.*, Vol. 2, pp. 985-1030, 1930.

32. Ede, A.J., Hislop, C.I. and Morris, R., "Effect of the Local Heat-Transfer Coefficient in a Pipe of an Abrupt Disturbance of the Fluid Flow: Abrupt Convergence and Divergence of Diameter Ratio 2/1", *Proc. Instn. Mech. Eng.*, Vol. 170, pp. 1113-1126, 1956.

33. Krall, K.M. and Sparrow, E.M., "Turbulent Heat Transfer in the Separated, Reattached and Redevelopment Regions of a Circular Tube, *J. Heat Transfer*, Trans. ASME, Vol. 88, pp. 131-136, 1966.

34. Giedt, W.H., "Investigation of Variation of Point Unit Heat-Transfer Coefficient Around a Cylinder Normal to an Air Stream", Trans. ASME, Vol. 71, pp. 375-381, 1949.

35. Oosthuizen, P.H., "Effects of Internal Conduction on the Determination of Heat Transfer Using Thin Film Heated Models", Queen's University, Department of Mechanical Engineering, Thermal and Fluid Sciences Group, Report No. 3/73, 1973.

36. Fergason, J.L., "Liquid Crystals", *Scientific American*, Vol. 211, No. 2, pp. 76-85, 1964.

37. Ede, A.J., "Advances in Free Convection", in *Advances in Heat Transfer*, edited by Hartnett, J.P. and Irvine, T.F., Vol. 4, pp. 1-64, Academic Press, New York, 1967.

38. Rich, B.R., "An Investigation of Heat Transfer from an Inclined Flat Plate in Free Convection", Trans. ASME, Vol. 75, pp. 489-497, 1953.

39. Kierkus, W.T., "An Analysis of Laminar Free Convection Flow and Heat Transfer about an Inclined Isothermal Plate", *Int. J. Heat Mass Transfer*, Vol. 11, pp. 241-253, 1968.

40. Cheesewright, R., "Turbulent Natural Convection From a Vertical Plane Surface", *J. Heat Transfer*, Trans. ASME, Vol. 90, pp. 1-8, 1968.

41. Ostrach, S., "An Analysis of Laminar Free-Convection Flow and Heat Transfer about a Flat Plate Parallel to the Direction of the Generating Body Force", NACA TR 1111, 1953.

42. Vliet, G.C. and Liu, C.K., "An Experimental Study of Turbulent Natural Convection Boundary Layers", *J. Heat Transfer*, Vol. 91, pp. 517-531, 1969.

43. Dotson, J.P., "Heat Transfer from a Vertical Plate by Free Convection", MS Thesis, Purdue University, 1954.

44. Fujii, T. and Imura, H., "Natural-Convection Heat Transfer from a Plate with Arbitrary Inclination", *Int. J. Heat Mass Transfer*, Vol. 15, pp. 755-767, 1972.

45. Fussey, D.E. and Warneford, I.P., "Free Convection from a Downward Facing Inclined Flat Plate", *Int. J. Heat Mass Transfer*, Vol. 21, pp. 119-126, 1978.

46. Sparrow, E.M. and Carlson, C.K., "Experimental Investigation of Heat Flux Uniformity at Thin, Electrically Heated Metallic Foils", *Int. J. Heat Mass Transfer*, Vol. 30, pp. 604-607, 1987.

47. Sparrow, E.M. and Gregg, J.L., "Laminar Free Convection from a Vertical Plate with Uniform Surface Heat Flux", Trans. ASME, Vol. 78, pp. 435-440, 1956.

48. Tarasuk, J.D. and Castle, G.S.P., "Temperature Distribution in an Electrically Heated Wide Metallic Foil", *J. Heat Transfer*, Trans. ASME, Vol. 105, pp. 210-212, 1983.

49. Schmidt, E. and Beckmann, W., "Das Temperatur- und Geschwindigkeitsfeld vor einer Warme abgebenden senkrechter Platte bei naturlicher Konvektion", *Tech. Mech. u. Thermodynamik*, Bd. 1, Nr. 10, pp. 341- 349, Okt. 1930, cont., Bd. 1, Nr. 11, pp. 391-406, Nov. 1930.

50. Squire, H.B., in *Modern Developments in Fluid Dynamics*, edited by Goldstein, S., Vol. 2, pp. 623-627, Oxford University Press, London and New York, 1938.

51. Eckert, E.R.G., *Introduction to the Transfer of Heat and Mass Transfer*, McGraw-Hill Book Company, New York, 1950.

52. Gebhart, B., "Natural Convection Flows and Stability", in *Advances in Heat Transfer*, edited by Hartnett, J.P. and Irvine, T.F., Vol. 9, pp. 273-349, Academic Press, New York, 1973.

53. Ostrach, S., "Natural Convection in Enclosures", in *Advances in Heat Transfer*, edited by Hartnett, J.P. and Irvine, T.F., Vol. 8, pp. 161-227, Academic Press, New York, 1972.

54. Beckmann, W., "Die Warmeubertragung in zylindrischen Gasschichton bei naturlicher Konvektion, *Forsch. Geb. d. Ingenieurwesen*, Bd. 2, Hept. 5, pp. 165-178, 1931.

55. Kraussold, H., "Wameabgabe von zylindrischen Flussigkeitschichton bei naturlicher Konvection, *Forsch. Geb. d. Ingenieurwesen*, Bd. 5, Hept. 4, pp. 186-188, 1934.

56. Liu, C., Mueller, W.K. and Landis, F., "Natural Convection Heat Transfer in Long Cylindrical Annuli", ASME *Int. Developments in Heat Transfer*, Pt. 4, pp. 976-984, 1961.

57. Grigull, U. and Hauf, W., "Natural Convection in Horizontal Cylindrical Annuli", AIChE *Proc. Third Int. Heat Transfer Conf.*, Vol. 2, pp. 182-195, 1966.

58. Lis, J., "Experimental Investigation of Natural Convection Heat Transfer in Simple and Obstructed Horizontal Annuli", AIChE *Proc. Third Int. Heat Transfer Conf.*, Vol. 2, pp. 196-204, 1966.

59. Bishop, E.H., Carley, C.T. and Powe, R.E., "Natural Convective Oscillating Flow in Cylindrical Annuli", *Int. J. Heat Mass Transfer*, Vol. 11, pp 1741-1752, 1968.

60. Powe, R.E., Carley, C.T. and Bishop, E.H., "Free Convective Flow Patterns in Cylindrical Annuli", *J. Heat Transfer*, Trans. ASME, Vol. 91, pp. 310-314, 1969.

61. Kuehn, T.H. and Goldstein, R.J., "An Experimental Study of Natural Convection Heat Transfer in Concentric and Eccentric Horizontal Cylindrical Annuli", *J. Heat Transfer*, Trans. ASME, Vol. 100, pp. 635-640, 1978.

62. Kuehn, T.H. and Goldstein, R.J., "A Parametric Study of Prandtl Number and Diameter Ratio Effects on Natural Convection Heat Transfer in Horizontal Cylindrical Annuli", *J. Heat Transfer*, Trans. ASME, Vol. 102, pp. 768-770, 1980.

63. Hessami, M.A., Pollard, A., Rowe, R.D. and Ruth, G.W., "A Study of Free Convective Heat Transfer in a Horizontal Annulus with a Large Radii Ratio", *J. Heat Transfer*, Trans. ASME, Vol. 107, pp. 603-610, 1985.

64. van de Sande, E. and Hamer, B.J.G., "Steady and Transient Natural Convection in Enclosures between Horizontal Circular Cylinders (Constant Heat Flux)", *Int. J. Heat Mass Transfer*, Vol. 22, pp. 361-370, 1979.

65. "Thermocouple Reference Tables", NBS Monograph 125, National Bureau of Standards, Washington, D.C., 1979.

66. Lawlor, D., "Calibration of One Hewlett-Packard Quartz Thermometer, Model 2804A, Serial No. 2432A01529", NRC *Physics Division*, Report No. APH2833, 1987.

67. Holman, J.P., *Heat Transfer*, 5th edition, McGraw-Hill Book Company, New York, 1981.

68. Incropera, F.P. and DeWitt, D.P., *Fundamentals of Heat and Mass Transfer*, 2nd edition, J. Wiley and Sons, New York, 1985.

69. Neher, R.T. and Edwards, D.K., "Far Infrared Reflectometer for Imperfectly Diffuse Specimens", *Applied Optics*, Vol. 4, No. 7, pp. 775-781, 1965.

70. Schlichting, H., *Boundary-Layer Theory*, 7th edition, McGraw-Hill Book Company, New York, 1979.

71. Na, T.Y., *Computational Methods in Engineering Boundary Value Problems*, Academic Press, New York, 1979.

72. Jones, M.L., Smith, G.M. and Wolford, J.C., *Applied Numerical Methods for Digital Computation with Fortran and CSMP*, 2nd edition, Harper and Row Publishers, New York, 1977.

73. Burden, R.L., Faires, J.D. and Reynolds, A.C., *Numerical Analysis*, 2nd Edition, Prindle, Weber and Schmidt, Boston, 1981.

74. Kline, S.J. and McClintock, F.A., "Describing Uncertainties in Single-Sample Experiments", *Mechanical Engineering*, Vol. 75, pp. 3-8, 1953.

75. "Tables of Thermal Properties of Gases", NBS Circular 564, National Bureau of Standards, Washington, D.C., 1955.

76. Patankar, S.V., *Numerical Heat Transfer and Fluid Flow*, McGraw-Hill Book Company, New York, 1980.

77. Van Doormaal, J.P. and Raithby, G.D., "Enhancements of the SIMPLE Method for Predicting Incompressible Fluid Flows", *Numerical Heat Transfer*, Vol. 7, pp. 147-163, 1984.

78. Kreith, F. and Black, W.Z., *Basic Heat Transfer*, Harper and Row, Publishers, New York, 1980.

APPENDIX A

DATA ACQUISITION PROGRAM

A computer program was written to acquire data using the equipment described in Section 2.2.3. After initialization of the coefficients in the thermocouple calibration polynomials, the program operates in one of three user-specified modes, namely: (i) setup mode; (ii) monitor mode; and (ii) final reading mode. A brief description of these three modes of operation are given in the remainder of this section.

The setup mode is designed to help the user adjust the voltage drop across the gold-film heater, prior to commencing a test, in order to obtain the desired heat flux at the surface of the heater. Because the resistance of the heater is slightly temperature dependent, setting the voltage source to give a certain heat flux is an iterative process. The computer assists the user by measuring the voltage drop across the heater, asking for the current reading from the ammeter to be manually input, and then calculating the heat flux generated inside the gold-film heater.

The monitor mode is designed to read the thermocouple voltages at prescribed time intervals, convert the voltages to temperatures using power-series polynomials obtained from thermocouple calibration runs, display the thermocouple temperatures, and calculate changes in temperatures from the last reading. This assists the user in determining when steady state has been achieved.

The final reading mode is dedicated to taking, storing, and displaying

data after steady state has been achieved. In addition to taking the temperature readings, the power supplied to the gold-film is measured. The ambient temperature and the barometric pressure in the laboratory are also recorded. Non-dimensional parameters relevant to the run are calculated. All of the data is stored on 3 1/2 inch hard diskettes, and a hard copy of the data is also printed.

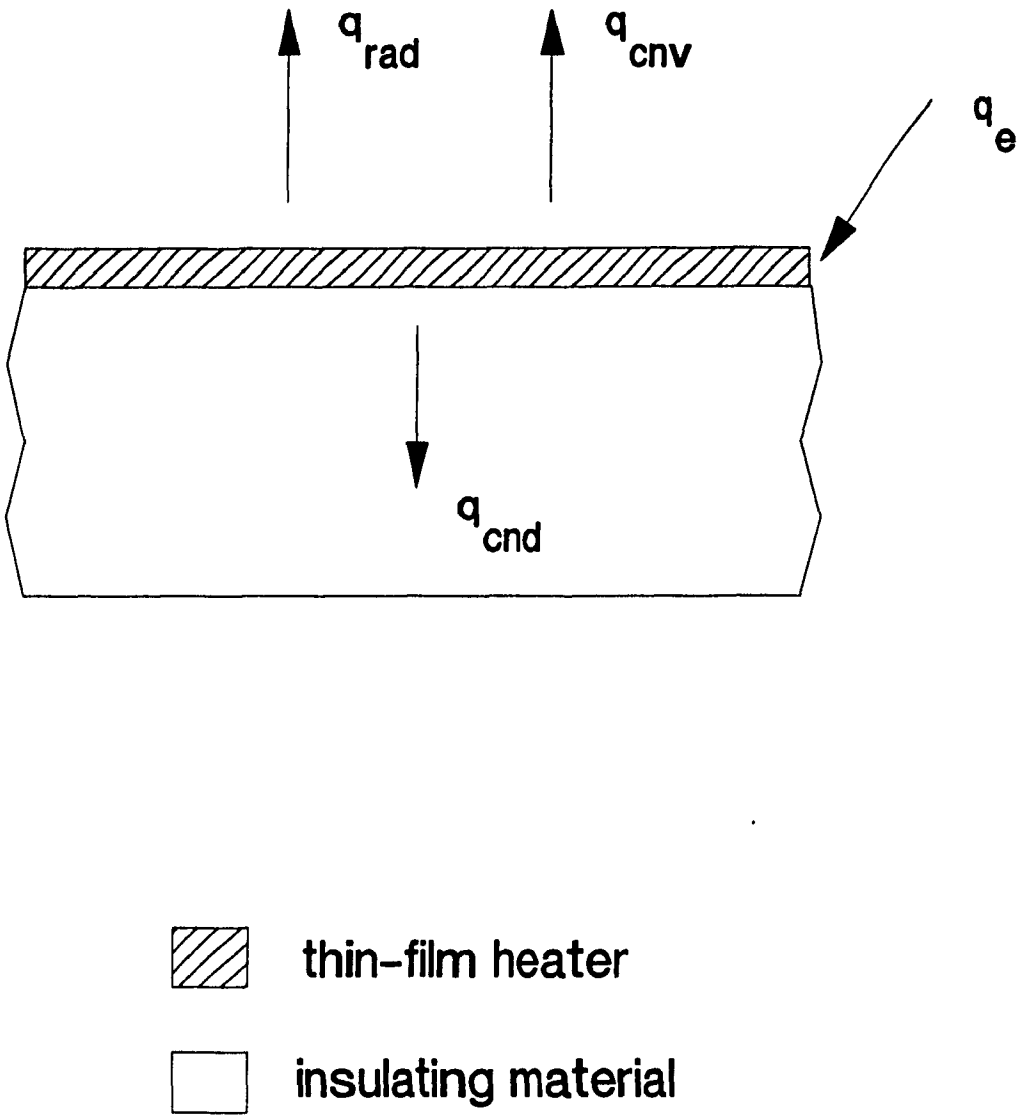

Figure 1: Energy balance applied to a point of interest, i, on the surface of a thin-film heater.

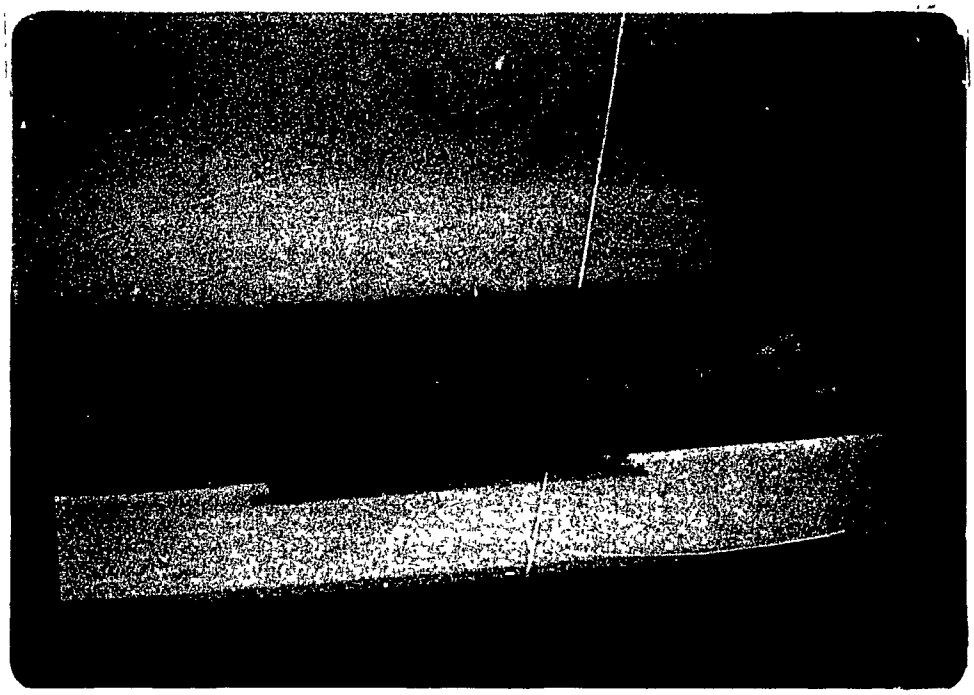

Figure 2: Photograph of the gold-film cutting apparatus.

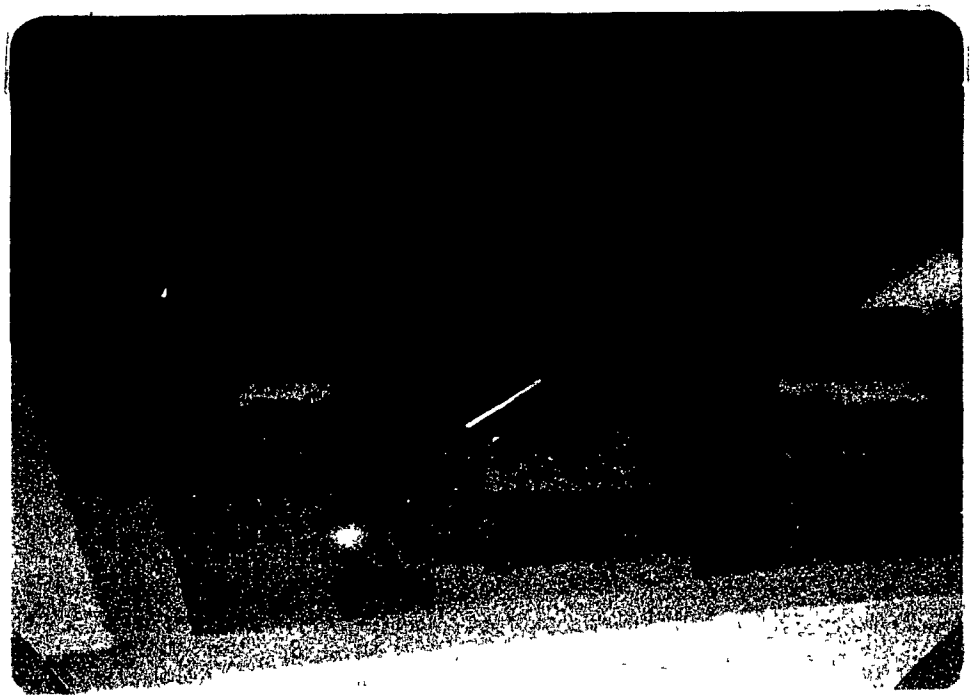

Figure 3: Close-up view of one of the cutting knives.

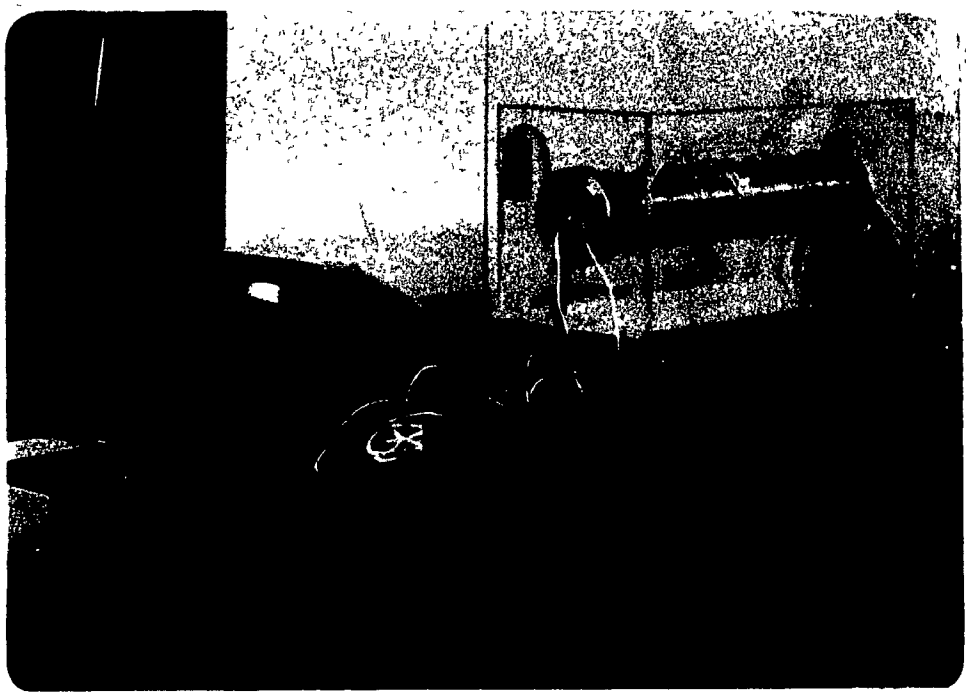

Figure 4: Photograph of the data acquisition, control and processing system. The power supply and digital multimeter are also visible in the right-hand side of the picture.

Figure 5: Photograph of the thermocouple welder and wire holder.

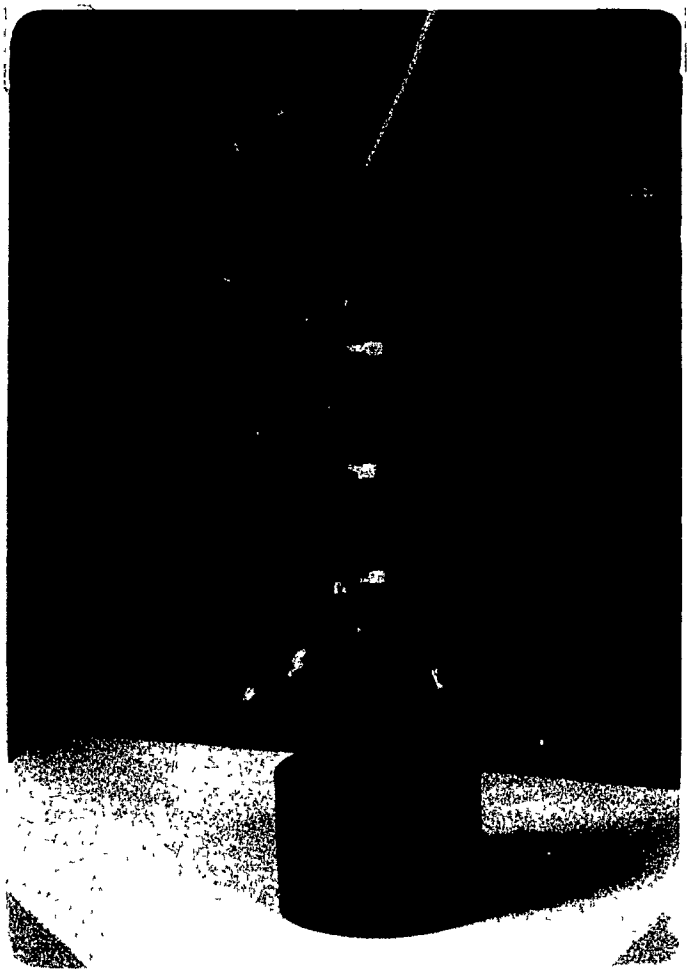

Figure 6: Photograph of the copper calibration block, with thermocouples and a quartz probe inserted into the holes.

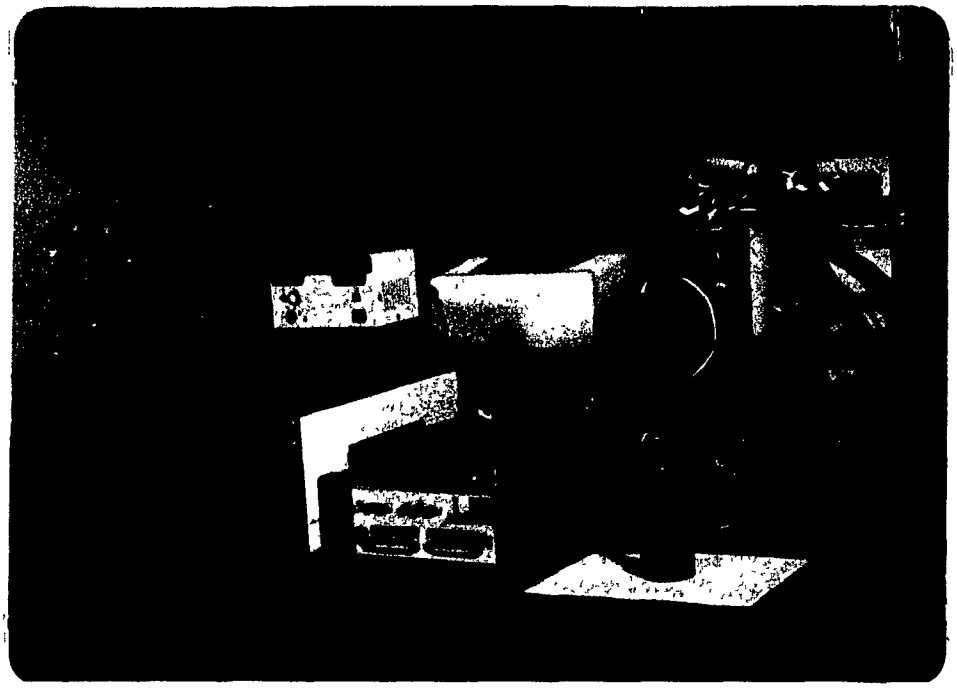

Figure 7: Photograph of the refrigerated water bath and the quartz thermometer instrumentation.

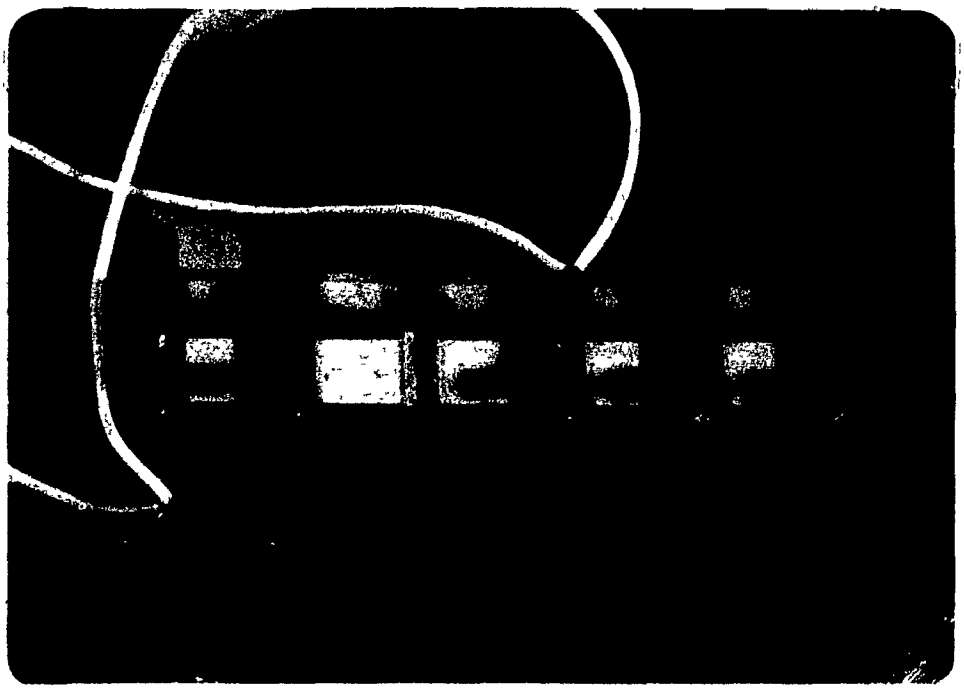

Figure 8: Photograph of the plexiglas apparatus used for taking electrical resistance measurements of 1 inch square gold-film samples.

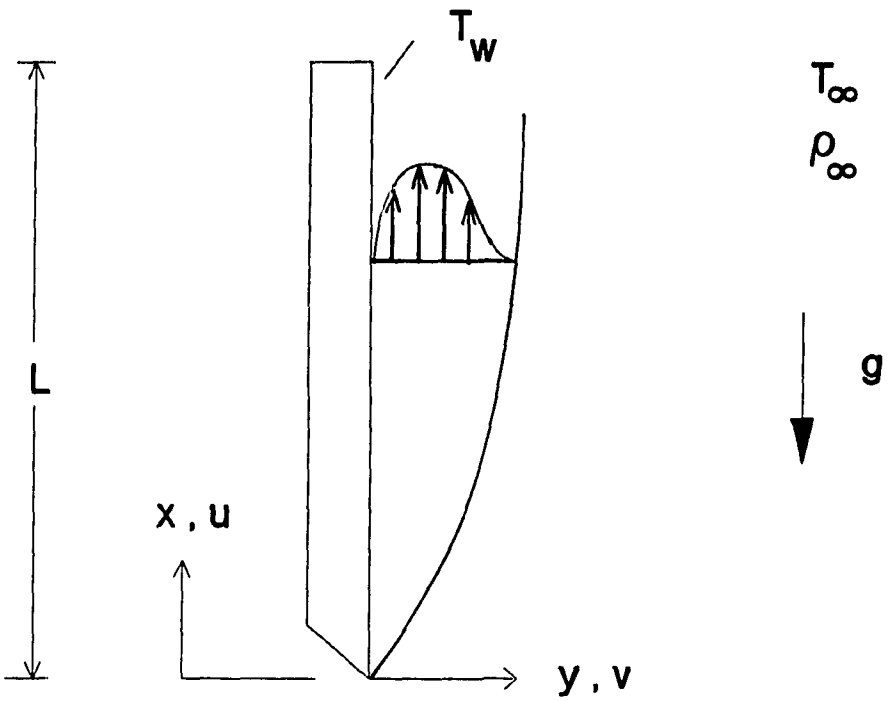

Figure 9: Diagram of the vertical flat plate problem.

Figure 10: Photograph of the vertical flat plate apparatus. The lines of constant colour on the plate indicate isotherms, and are produced by a liquid crystal sheet installed beneath the gold-film heater.

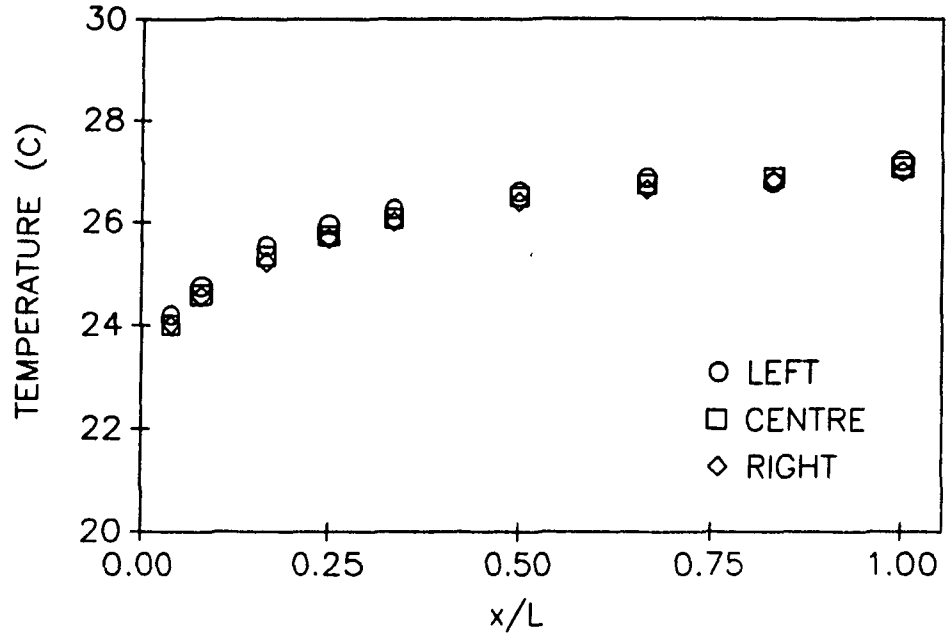

Figure 11: Spanwise temperature profiles on the vertical flat plate for $Gr_L^* = 5.6 \times 10^7$.

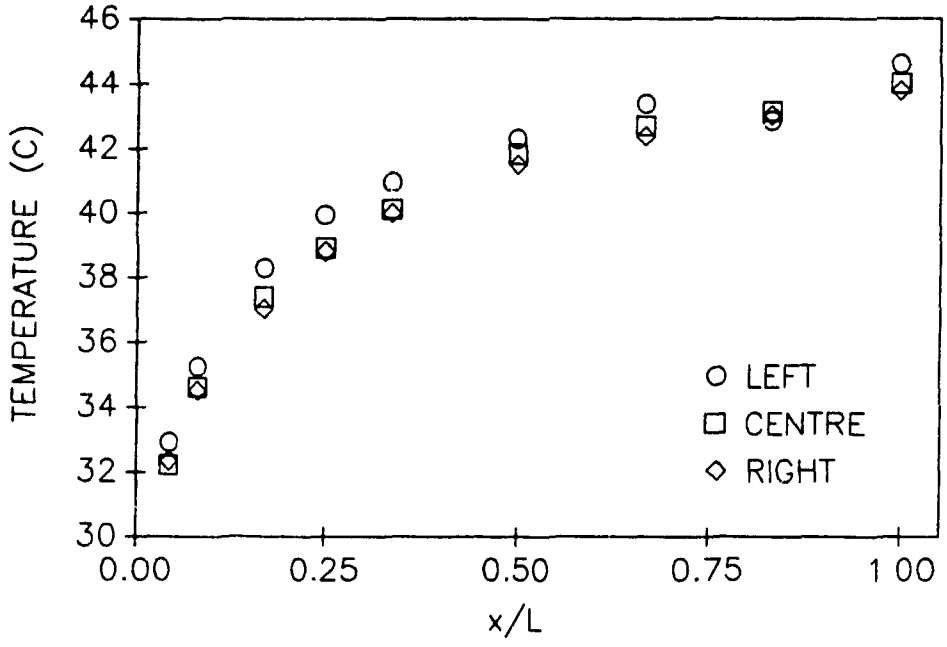

Figure 12: Spanwise temperature profiles on the vertical flat plate for $Gr_L^* = 2.7 \times 10^8$.

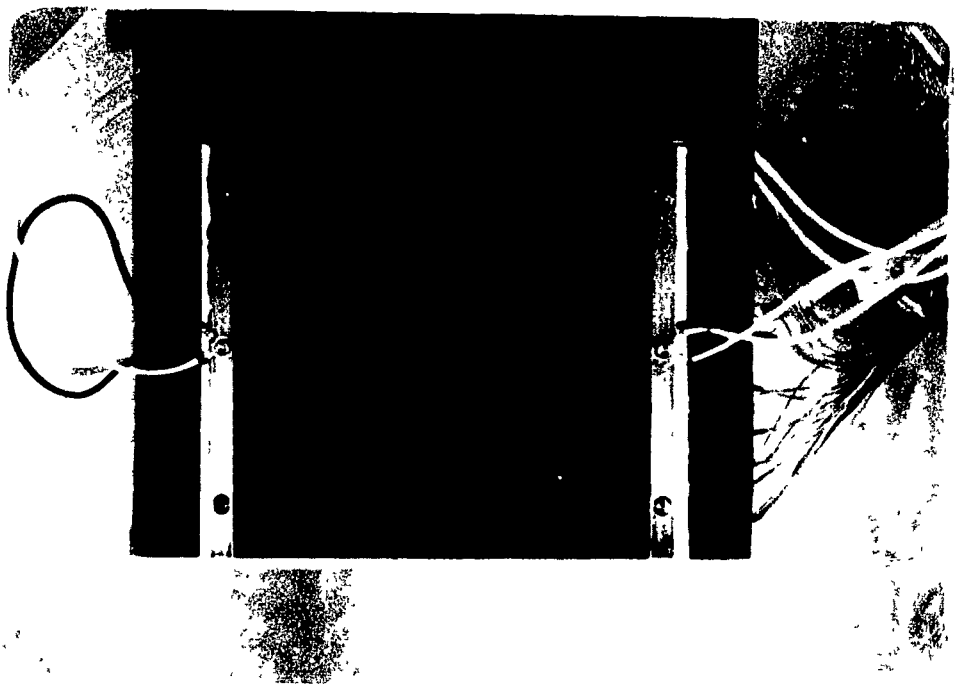

Figure 13: Close-up view of the vertical flat plate. The vertical lines in the photograph are due to light reflections from gaps between the strips of double-sided adhesive.

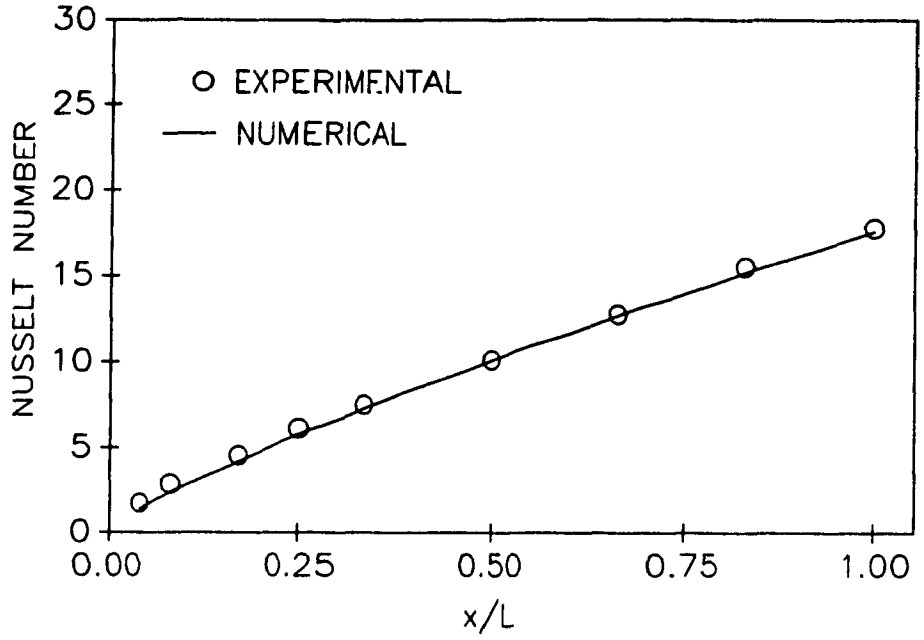

Figure 14: Local Nusselt number, Nu_x, versus distance along the vertical flat plate, x/L, results for $Gr_L^* = 5.6 \times 10^7$.

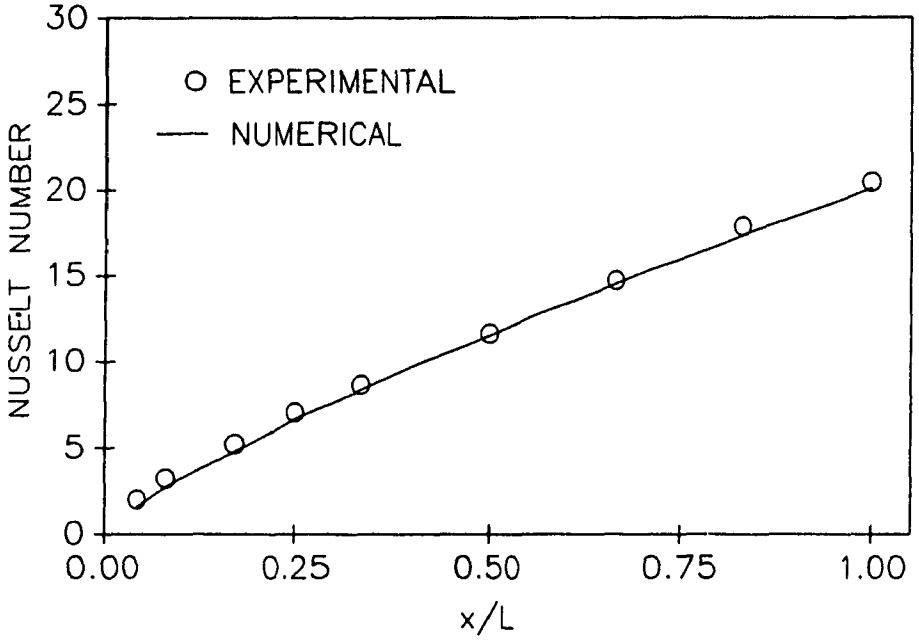

Figure 15: Local Nusselt number, Nu_x, versus distance along the vertical flat plate, x/L, results for $Gr_L^* = 1.1 \times 10^8$.

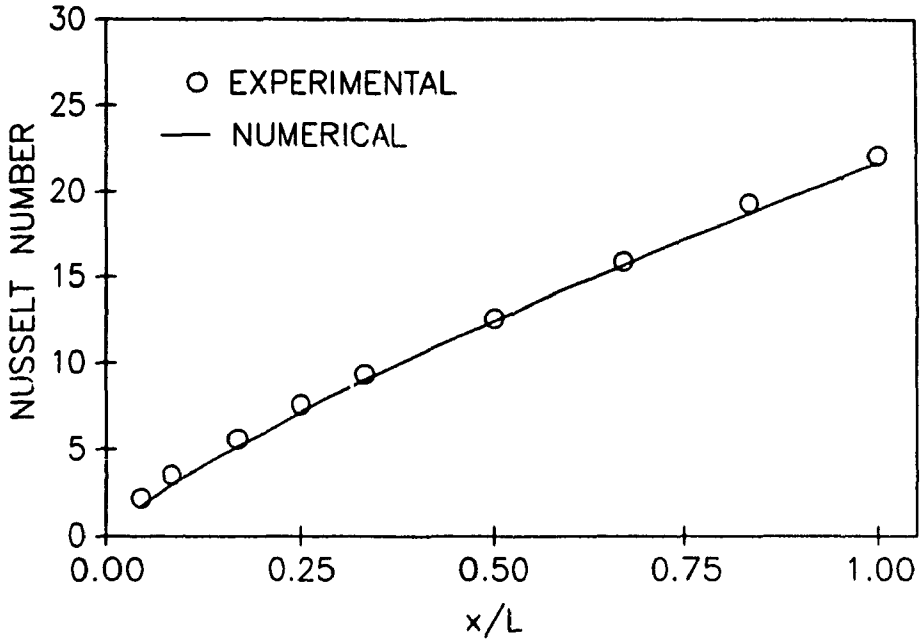

Figure 16: Local Nusselt number, Nu_x, versus distance along the vertical flat plate, x/L, results for $Gr_L^* = 1.6 \times 10^8$.

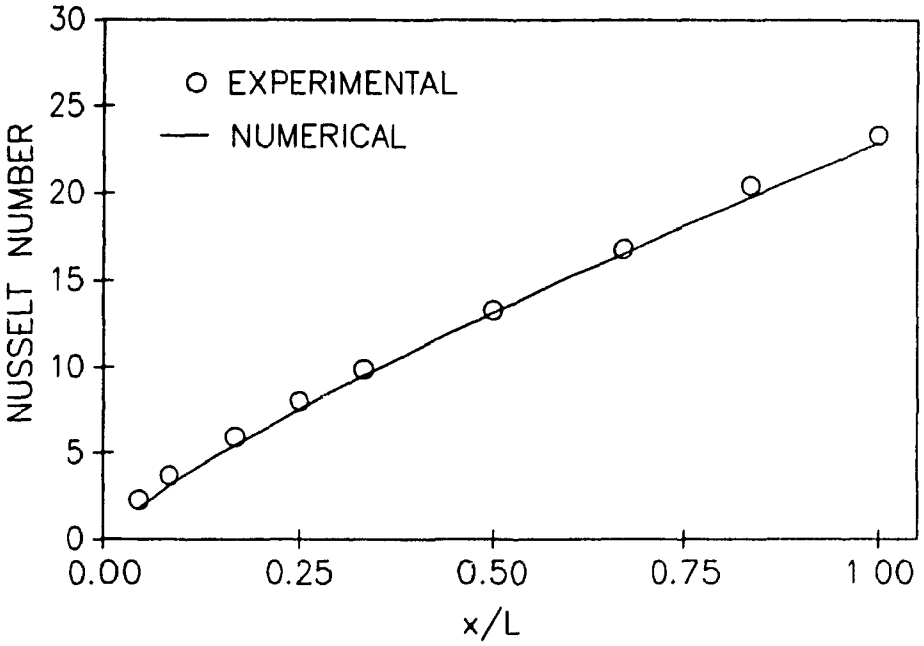

Figure 17: Local Nusselt number, Nu_x, versus distance along the vertical flat plate, x/L, results for $Gr_L^* = 2.1 \times 10^8$.

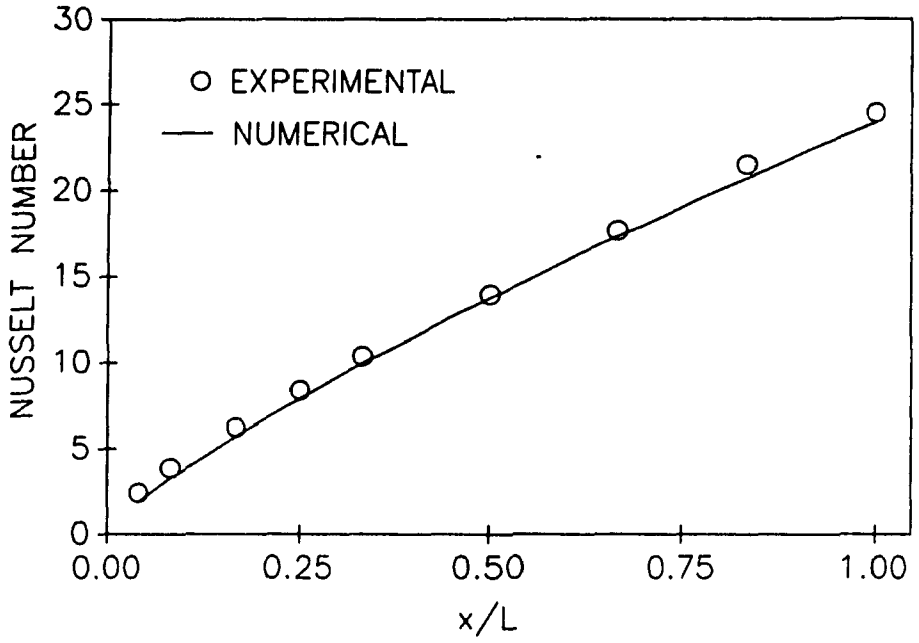

Figure 18: Local Nusselt number, Nu_x, versus distance along the vertical flat plate, x/L, results for $Gr_L^* = 2.7 \times 10^8$.

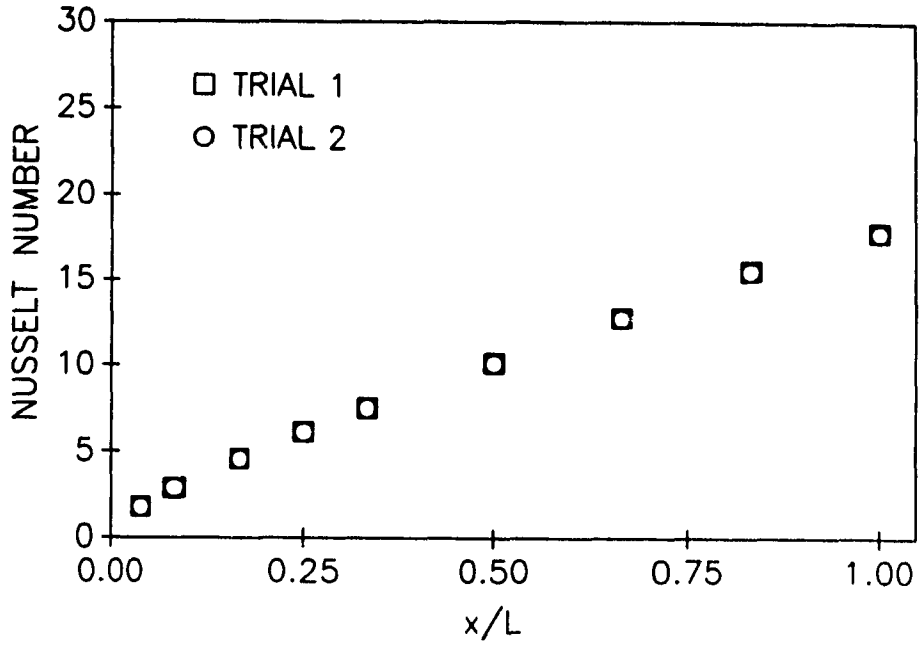

Figure 19: Repeatability of local Nusselt number, Nu_x, versus distance along the vertical flat plate, x/L, results for $Gr_L^* = 5.6 \times 10^7$.

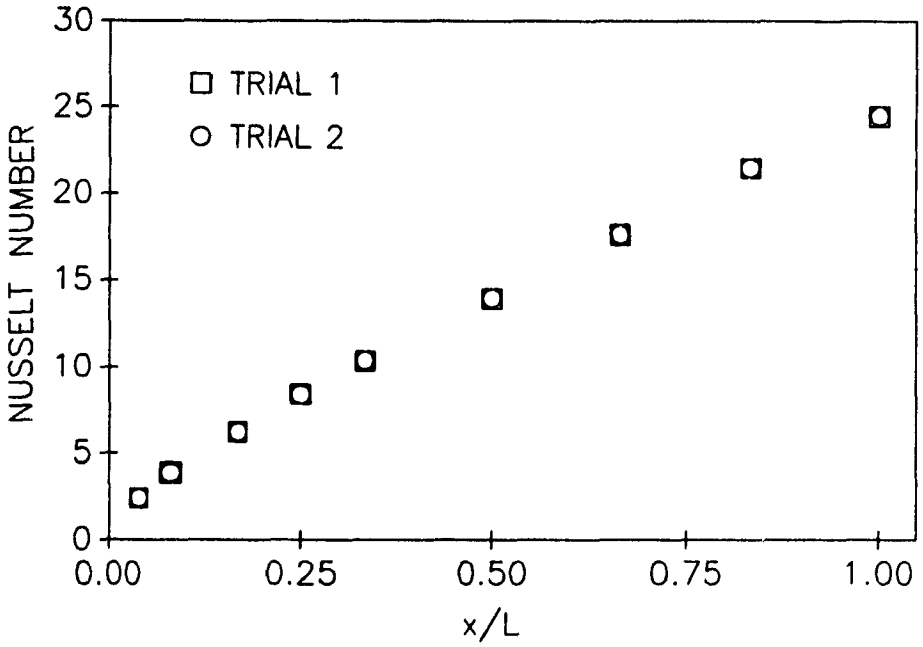

Figure 20: Repeatability of local Nusselt number, Nu_x, versus distance along the vertical flat plate, x/L, results for $Gr_L^* = 2.7 \times 10^8$.

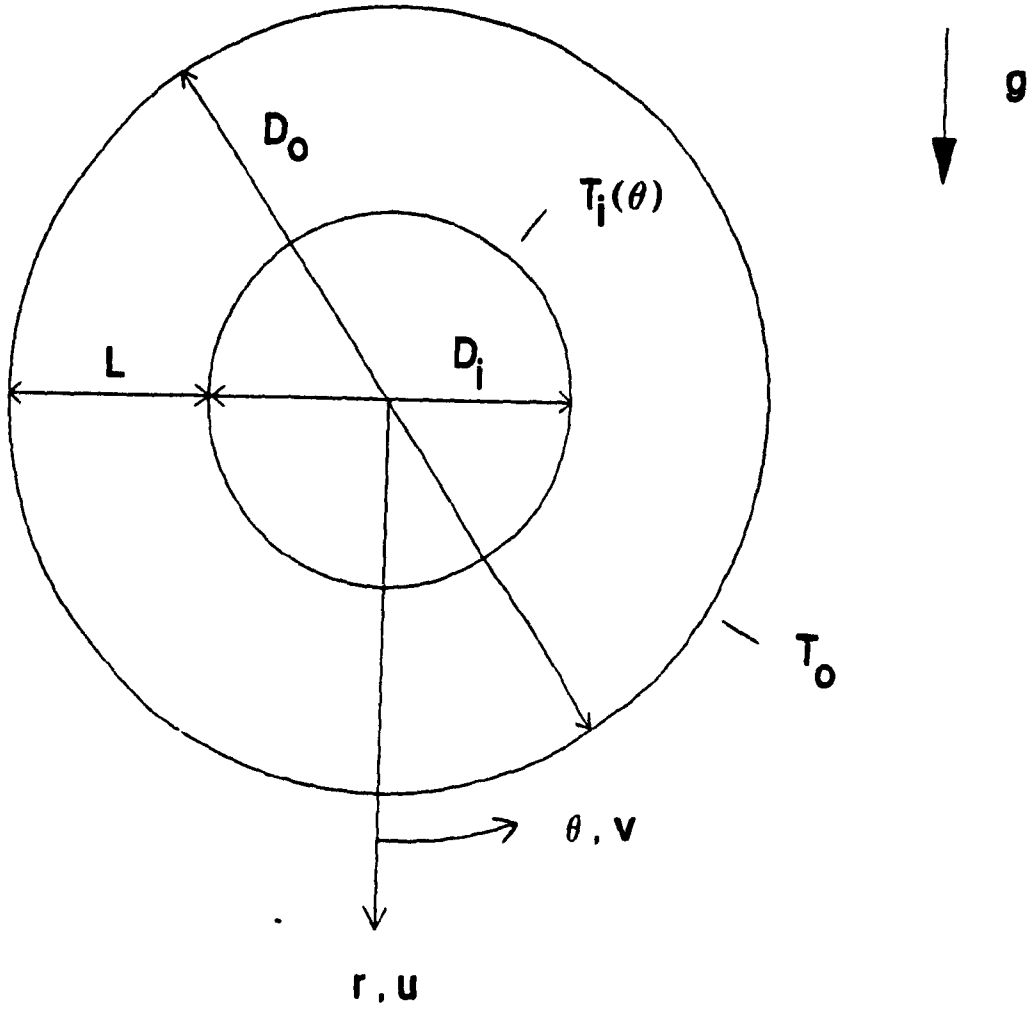

Figure 21: Diagram of the two-dimensional, horizontal concentric annulus problem.

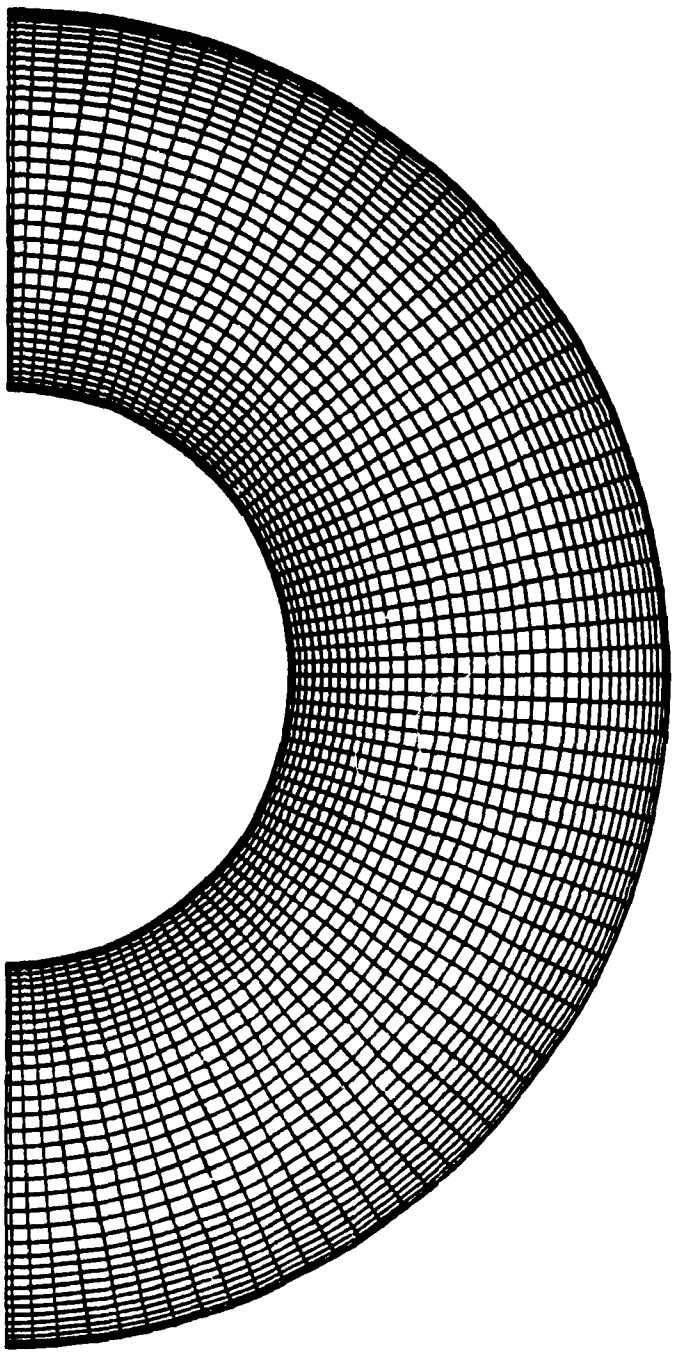

Figure 22: Domain discretization for the computations of natural convection in a horizontal concentric annulus.

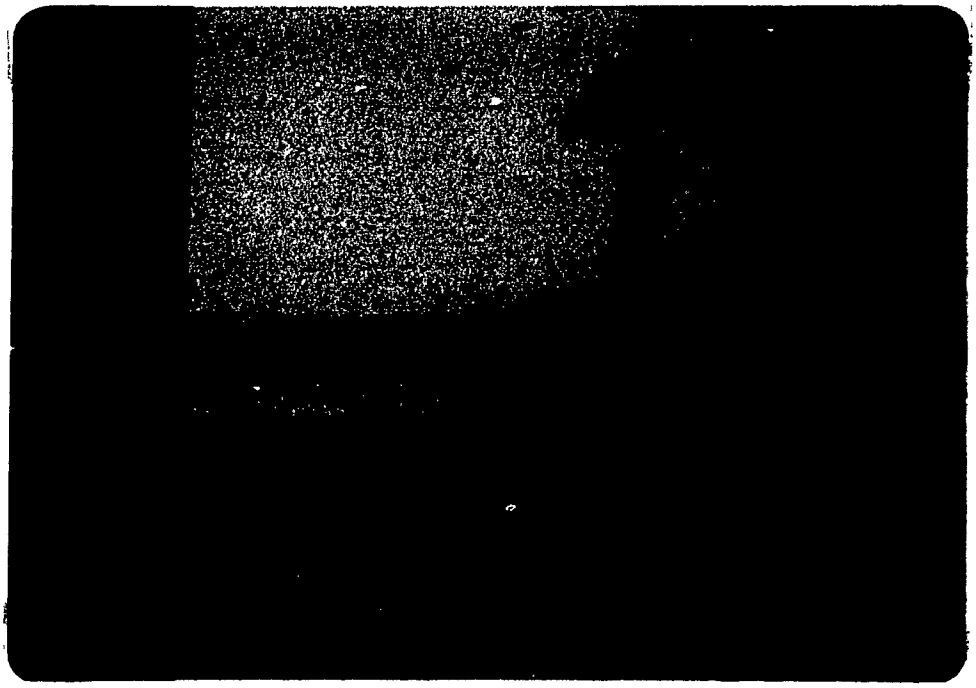

Figure 23: Photograph of the inner cylinder after the thermocouples have been attached. The three pieces of the inner cylinder can be seen in the picture.

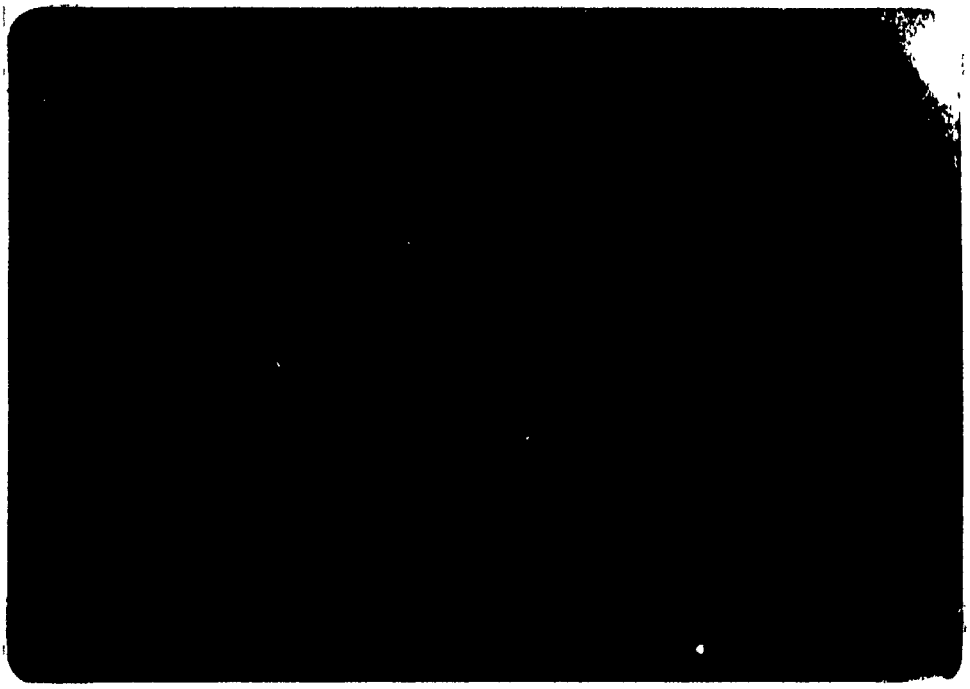

Figure 24: Photograph of the copper electrodes and the plexiglas end plates used for the concentric cylinder experiment. The semi-circular clamps may be seen in the left-hand side of the picture.

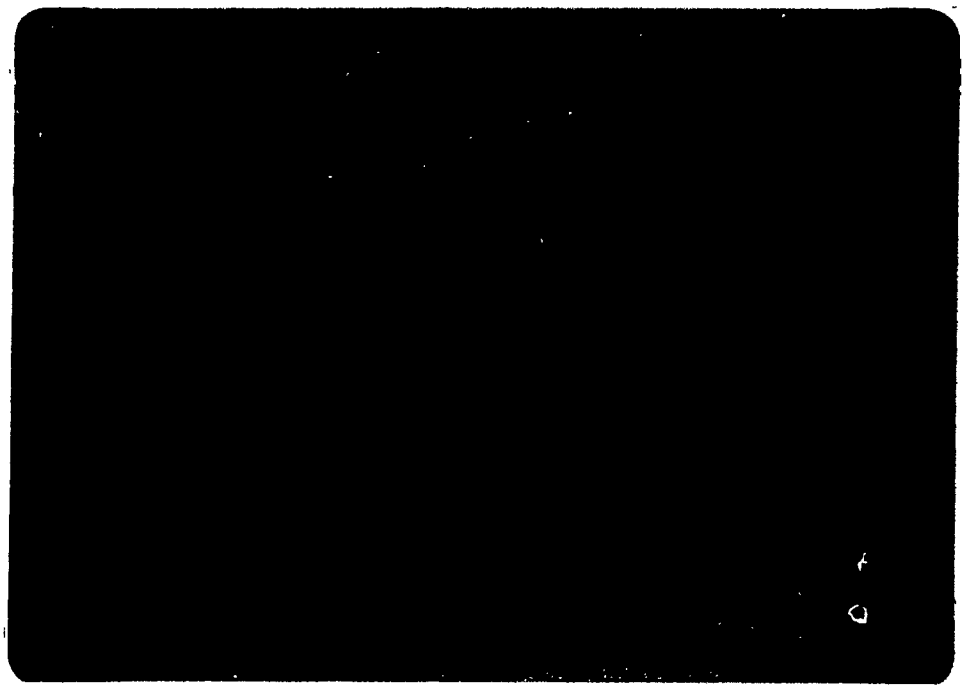

Figure 25: Photograph of one of the electrodes after it has been attached to the gold-film heater.

Figure 26: Photograph of the inner cylinder after it has been filled with vermiculite insulation. Removable tape is protecting the gold-film heater.

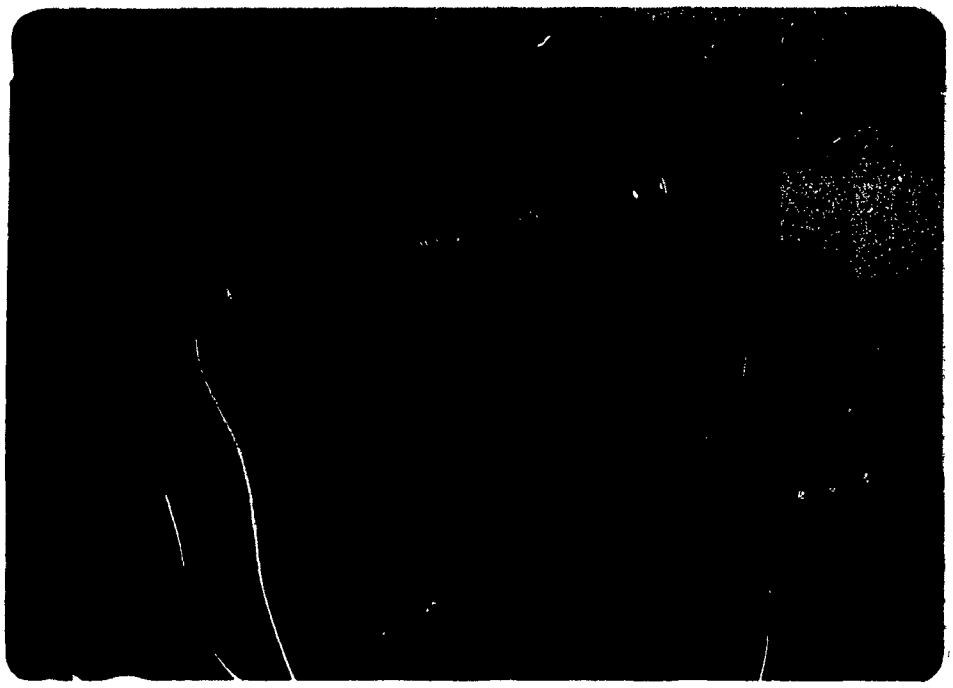

Figure 27: Photograph of the concentric cylinder apparatus.

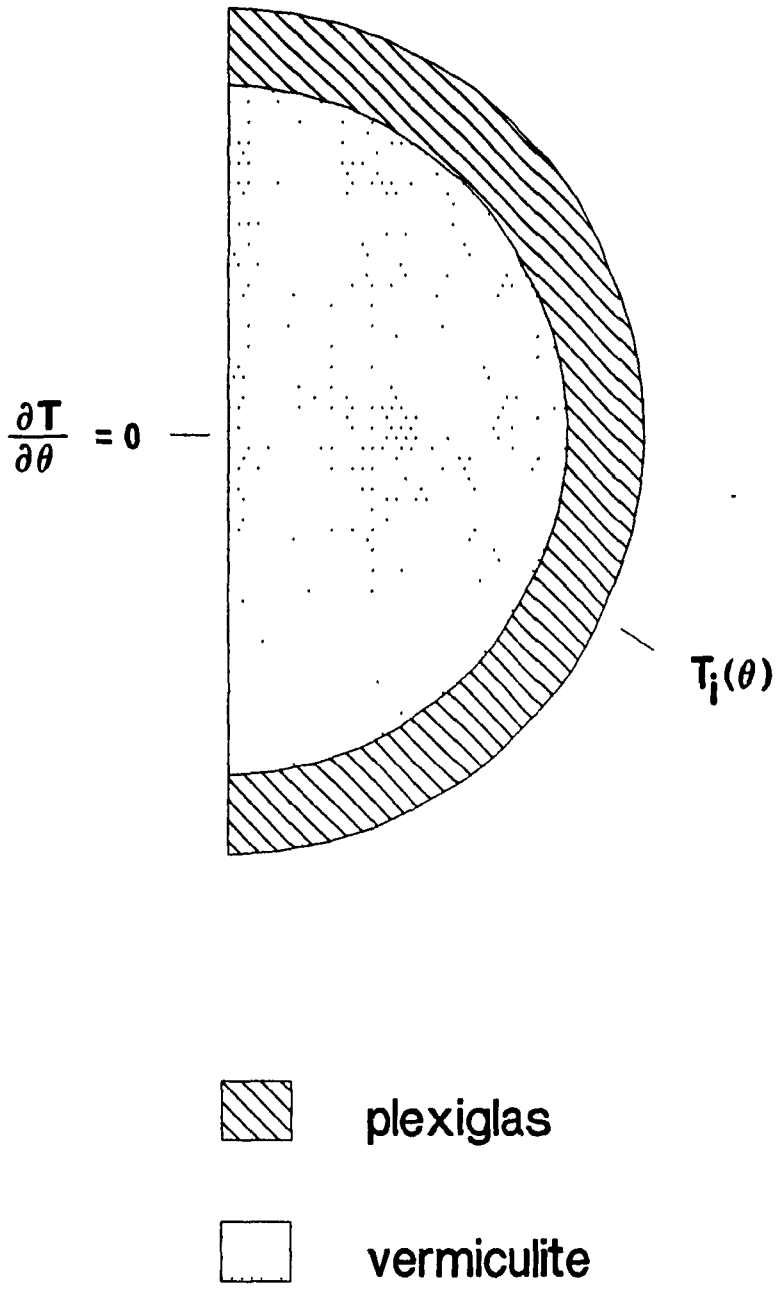

Figure 28: Diagram of the two-dimensional heat conduction problem inside the plexiglas cylinder.

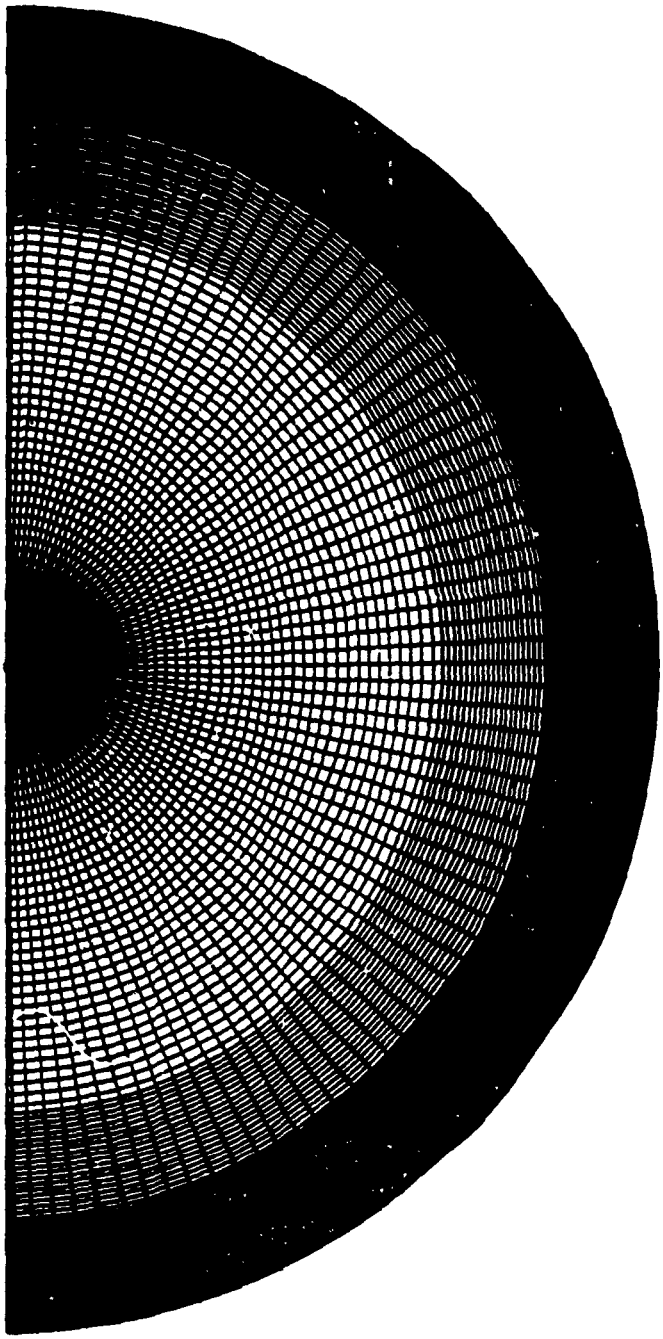

Figure 29: Domain discretization for the two-dimensional heat conduction problem.

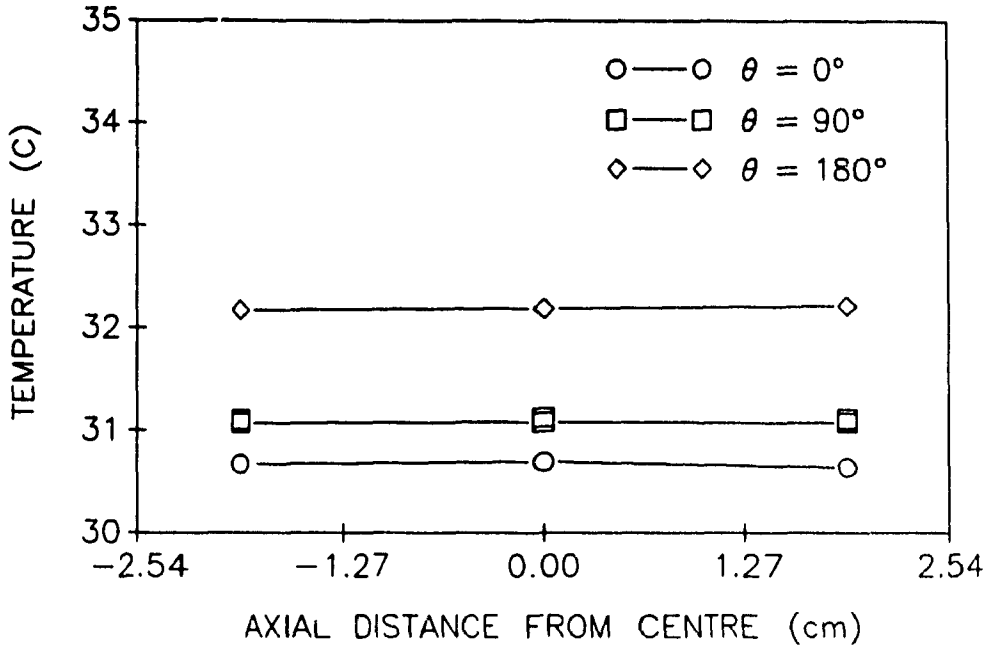

Figure 30: Axial temperature profile on the surface of the inner cylinder for $Ra_{D_i} = 2.97 \times 10^4$.

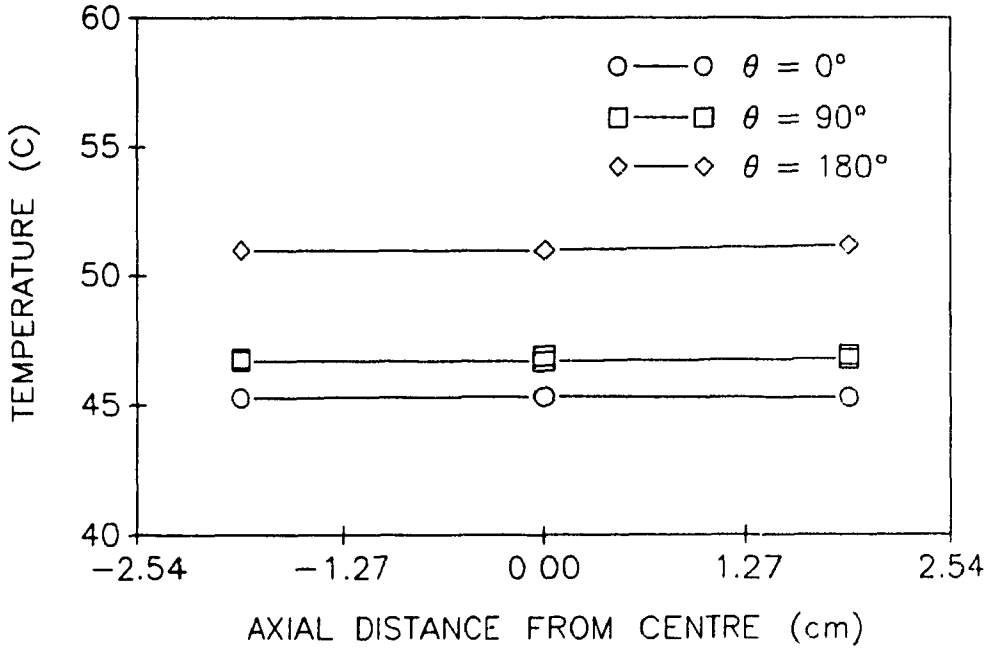

Figure 31: Axial temperature profile on the surface of the inner cylinder for $Ra_{D_i} = 9.88 \times 10^4$.

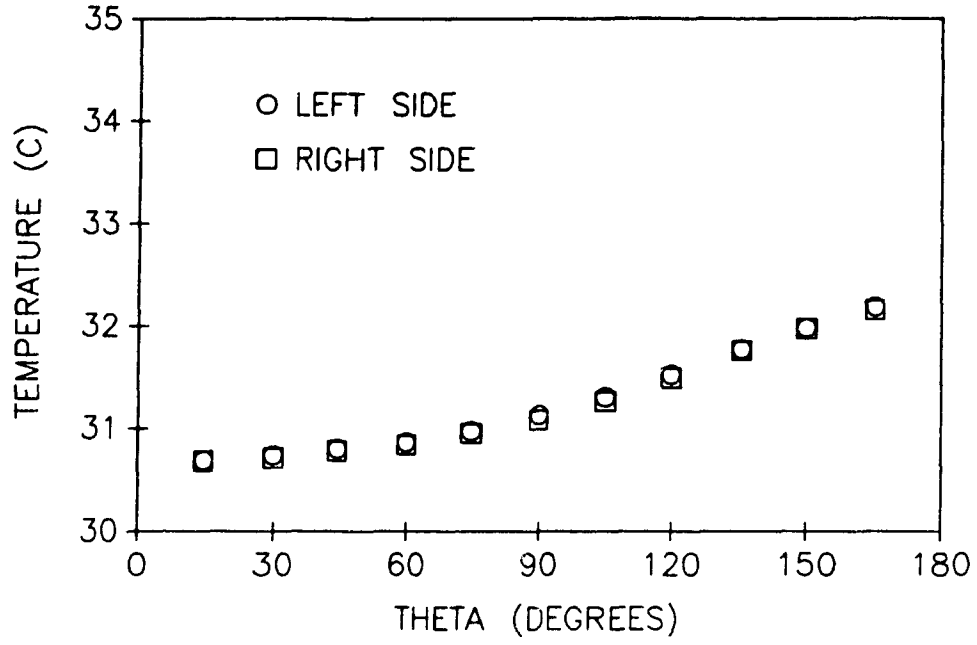

Figure 32: Symmetry of temperature in the θ-direction, about the vertical plane, on the surface of the inner cylinder for $Ra_{D_i} = 2.97 \times 10^4$.

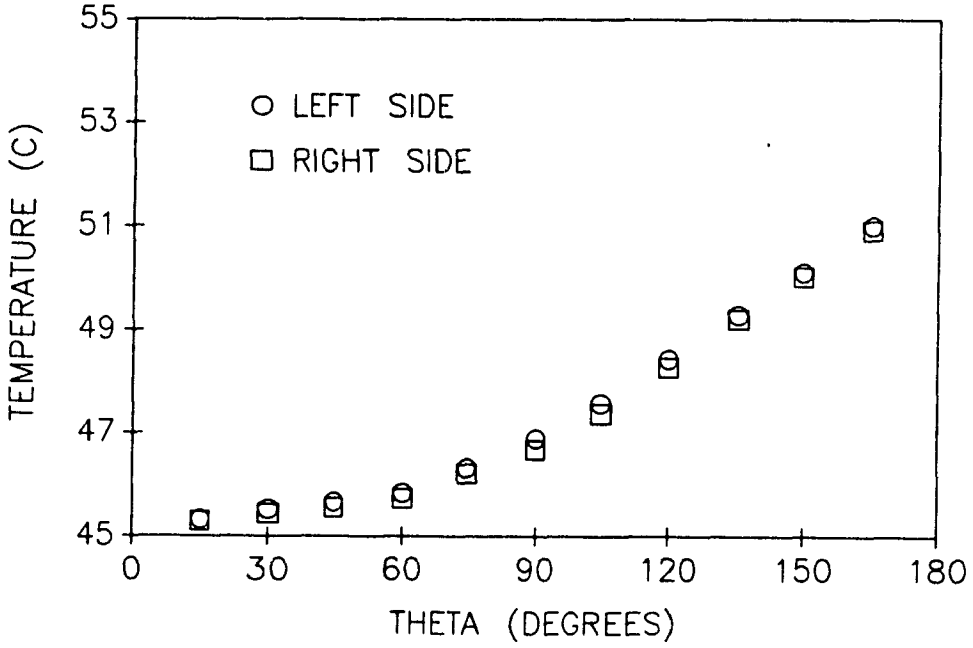

Figure 33: Symmetry of temperature in the θ-direction, about the vertical plane, on the surface of the inner cylinder for $Ra_{D_i} = 9.88 \times 10^4$.

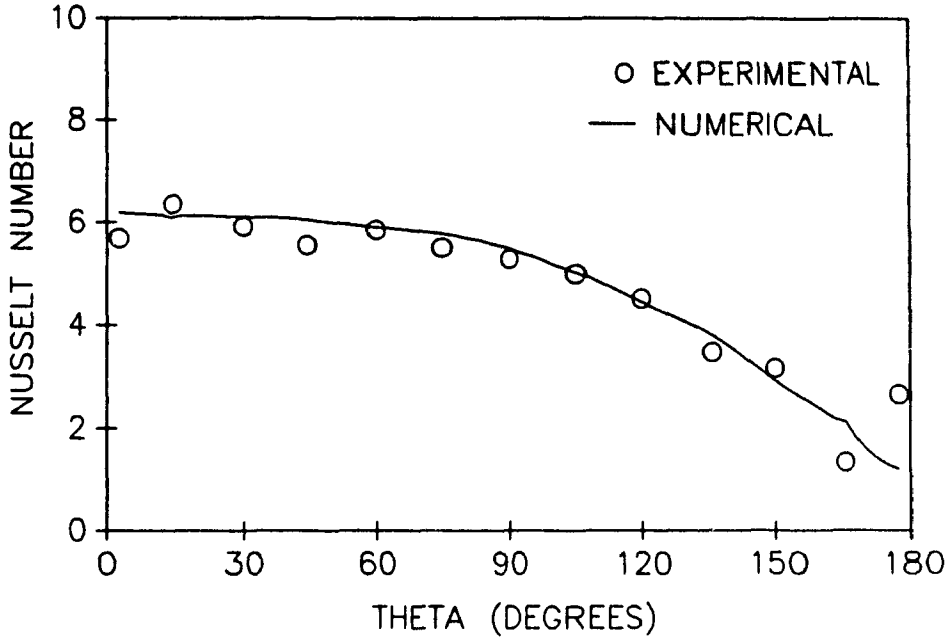

Figure 34: Local Nusselt number, Nu_{D_i}, versus θ results for $Ra_{D_i} = 2.97 \times 10^4$.

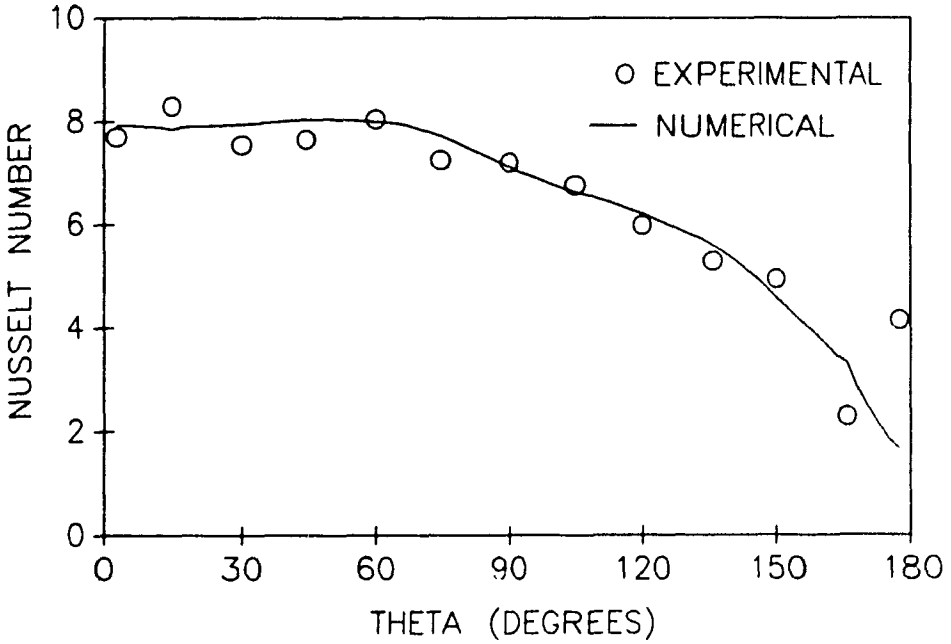

Figure 35: Local Nusselt number, Nu_{D_i}, versus θ results for $Ra_{D_i} = 9.88 \times 10^4$.

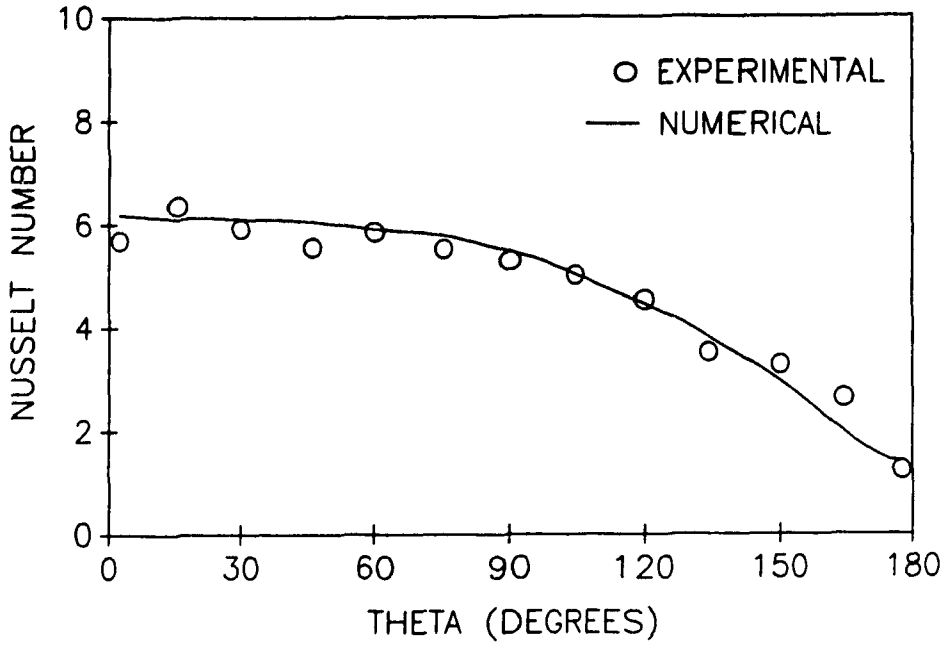

Figure 36: Local Nusselt number, Nu_{D_i}, versus θ results using an extrapolated temperature at $\theta = 180^{\circ}$ for $Ra_{D_i} = 2.97 \times 10^4$.

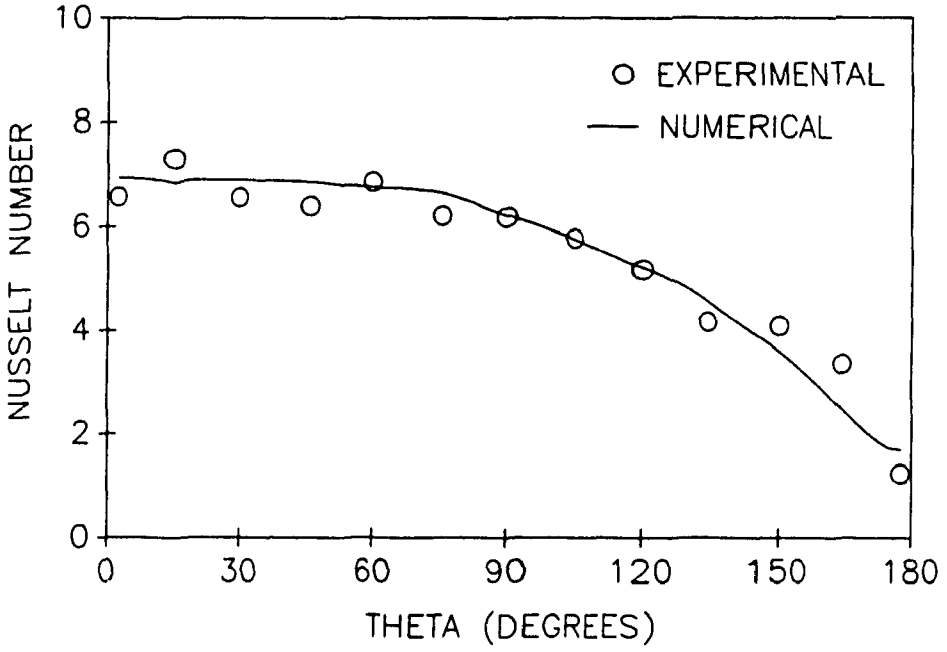

Figure 37: Local Nusselt number, Nu_{D_i}, versus θ results using an extrapolated temperature at $\theta = 180^{\circ}$ for $Ra_{D_i} = 5.04 \times 10^4$.

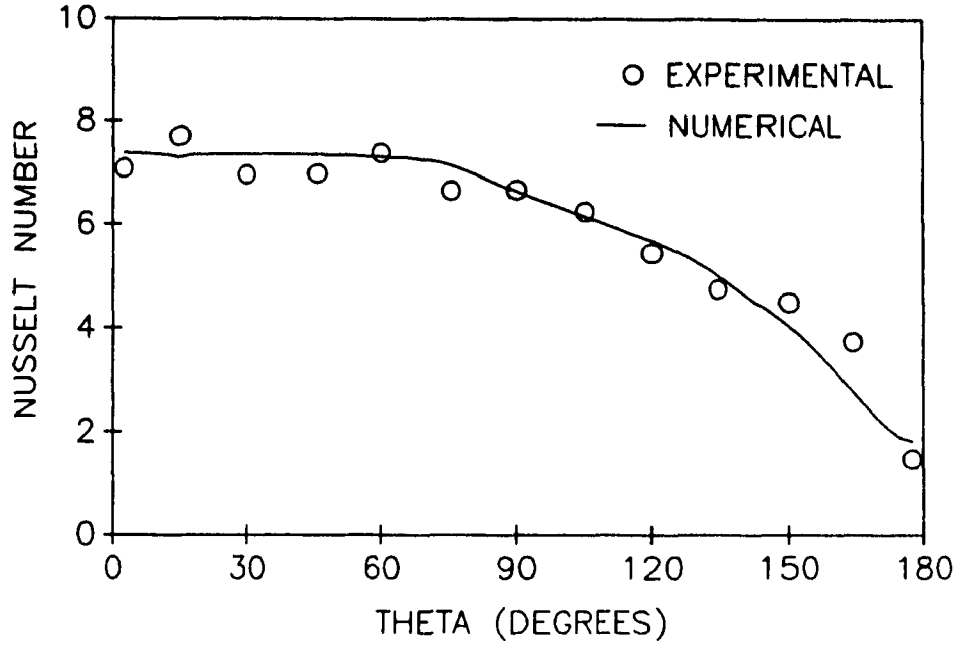

Figure 38: Local Nusselt number, Nu_{D_i}, versus θ results using an extrapolated temperature at $\theta = 180^{\circ}$ for $Ra_{D_i} = 6.83 \times 10^4$.

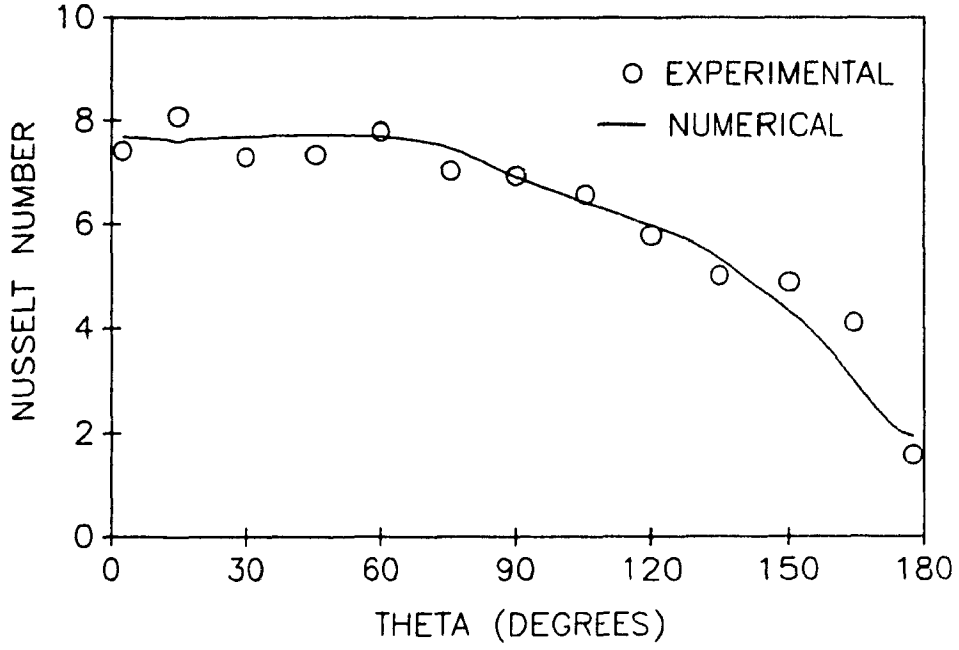

Figure 39: Local Nusselt number, Nu_{D_i}, versus θ results using an extrapolated temperature at $\theta = 180^{\circ}$ for $Ra_{D_i} = 8.41 \times 10^4$.

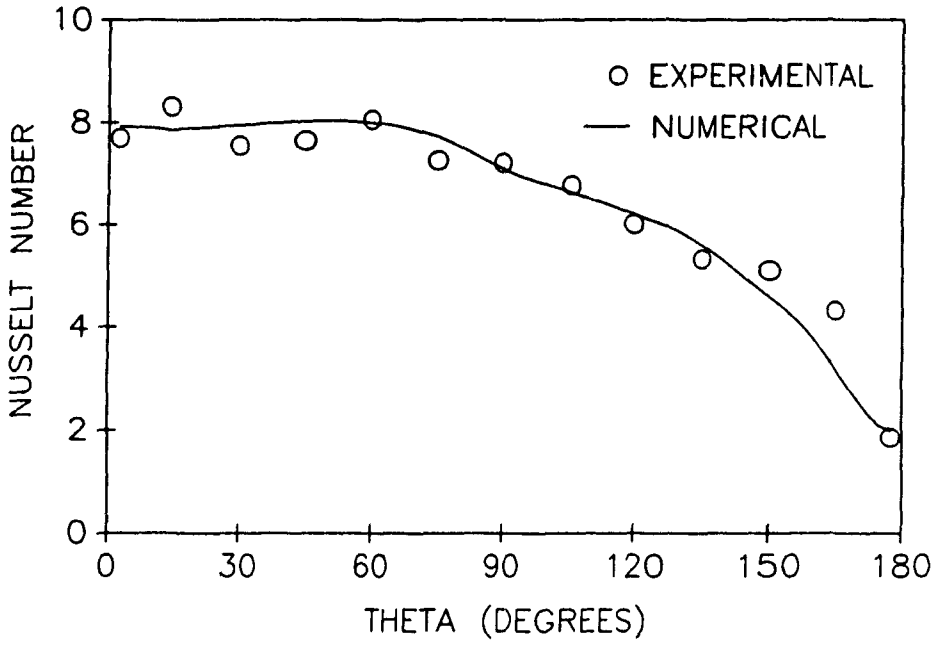

Figure 40: Local Nusselt number, Nu_{D_i}, versus θ results using an extrapolated temperature at $\theta = 180^{\circ}$ for $Ra_{D_i} = 9.88 \times 10^4$.

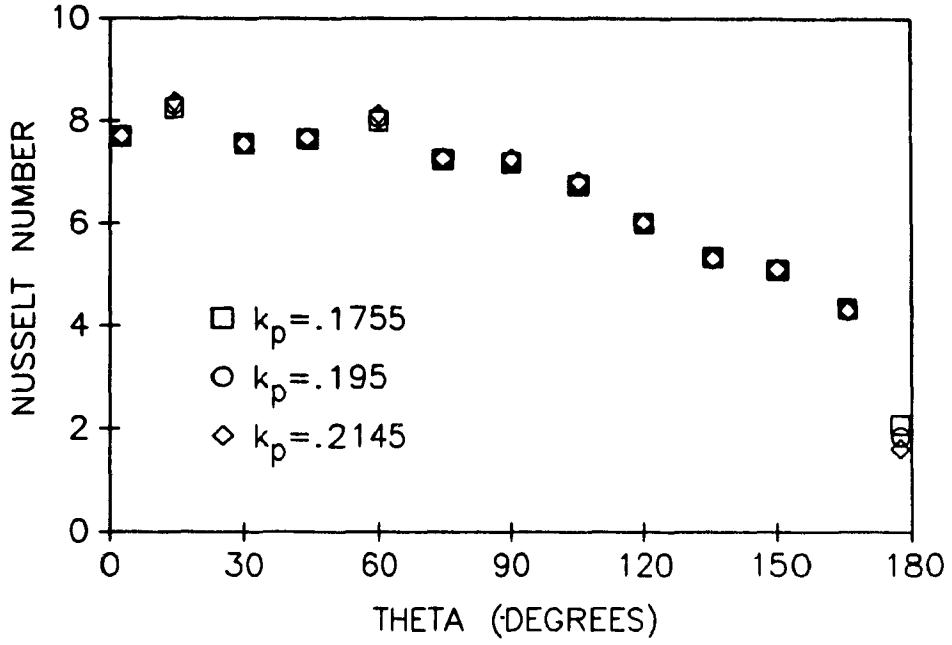

Figure 41: **Influence of uncertainty of plexiglas thermal conductivity on local Nusselt number, Nu_{D_i}, versus θ results using an extrapolated temperature at θ = 180° for Ra_{D_i} = 2.97 x 10^4.**

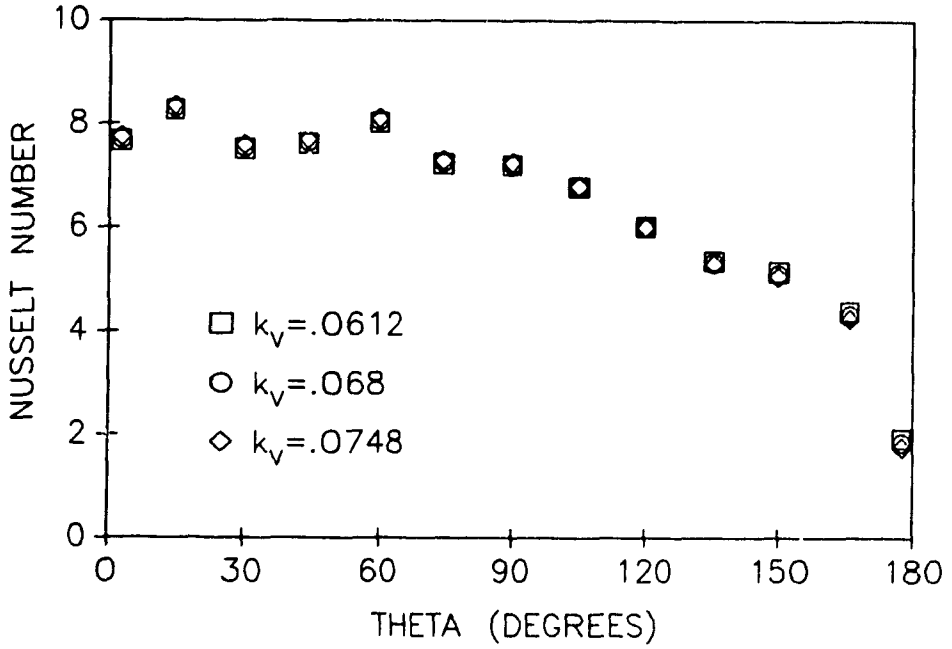

Figure 42: **Influence of uncertainty of vermiculite thermal conductivity on local Nusselt number, Nu_{D_i}, versus θ results using an extrapolated temperature at θ = 180° for Ra_{D_i} = 9.88 x 10^4.**

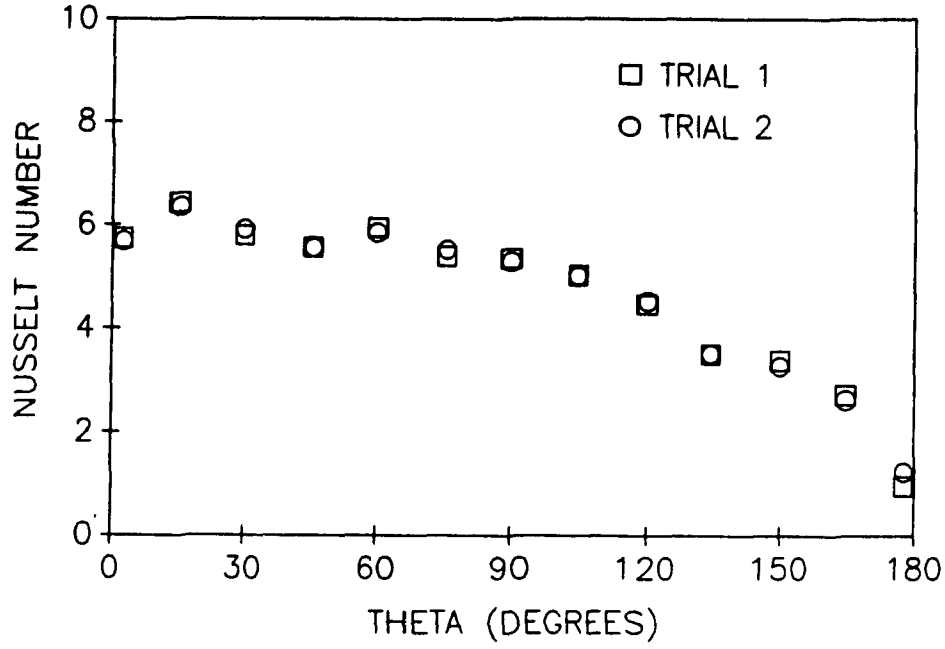

Figure 43: Repeatability of local Nusselt number, Nu_{D_i}, versus θ results using an extrapolated temperature at $\theta = 180^{\circ}$ for $Ra_{D_i} = 2.97 \times 10^4$.

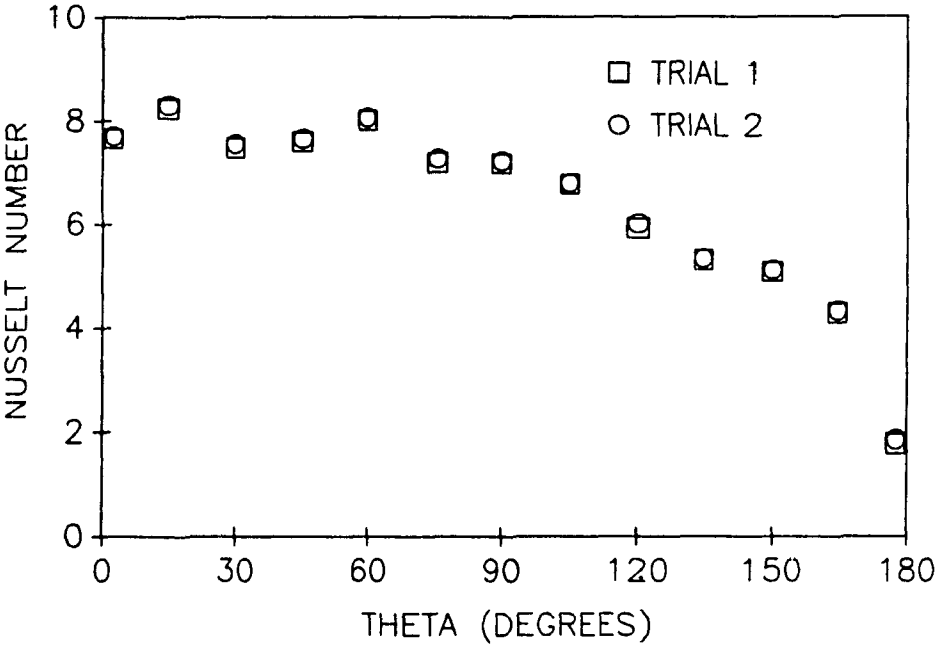

Figure 44: Repeatability of local Nusselt number, Nu_{D_i}, versus θ results using an extrapolated temperature at $\theta = 180^{\circ}$ for $Ra_{D_i} = 9.88 \times 10^4$.

GOLD-FILM RESISTIVITY MEASUREMENTS

SAMPLE	NUMBER 1	NUMBER 2	NUMBER 3	NUMBER 4	NUMBER 5
1	13.36	13.55	13.81	15.21	13.10
2	12.64	13.49	13.88	13.10	12.93
3	13.45	12.93	13.17	12.80	12.82
4	13.07	13.61	13.33	13.05	13.37
5	13.55	13.53	13.37	13.29	13.39
6	13.11	13.40	13.35	13.33	13.19
7		** RESISTANCE CHANGED WITH TIME **			
8	13.70	13.80	14.07	13.39	13.88
9	13.56	13.85	13.73	13.57	14.01
10	13.46	13.53	13.63	13.79	13.71
11	13.84	13.68	13.80	13.97	13.70
12	13.58	14.17	14.15	14.02	13.73

SUMMARY OF GOLD-FILM RESISTIVITY MEASUREMENTS

Average Resistivity = 13.54 Ω/sq.

Standard Deviation = 0.42 Ω/sq.

Table 1: Resistivity measurements of gold-film samples.

LAMINAR NATURAL CONVECTION ALONG A VERTICAL FLAT PLATE

			PRESENT	REFERENCE [47]
PRANDTL	$F''(0)$	$\theta(0)$	$Nu_x\ (Gr^*)^{-1/5}$	$Nu_x\ (Gr^*)^{-1/5}$
0.1	1.645	-2.752	0.263	0.263
0.7	0.8236	-1.500	0.483	-
1.0	0.7229	-1.358	0.534	0.534
10.0	0.3068	-0.7685	0.943	0.944
100.0	0.1264	-0.4668	1.55	1.56

Table 2: Comparison of local Nusselt number, Nu_x, versus distance along the vertical flat plate, x/L, between the present numerical results and those of Sparrow and Gregg [47].

LAMINAR NATURAL CONVECTION ALONG A VERTICAL FLAT PLATE

PARAMETERS

$Gr_L^* = 5.6 \times 10^7 \pm 3.32 \times 10^6$

$Pr = 0.71$

$q_e = 24.85\ W/m^2$

$T_{air} = 294.17\ K$

	EXPERIMENTAL				THEORETICAL	
x/L	T (K)	q_{rad} (W/m^2)	q_{cnv} (W/m^2)	Nu_x	Nu_x	Δ (%)
1/24	297.17	3.17	21.68	1.76 ± 0.22	1.38	27.5
1/12	297.76	3.81	21.05	2.86 ± 0.28	2.40	19.2
1/6	298.50	4.60	20.62	4.57 ± 0.43	4.18	9.3
1/4	298.90	5.04	20.25	6.13 ± 0.59	5.79	5.9
1/3	299.23	5.40	20.00	7.51 ± 0.74	7.29	3.0
1/2	299.67	5.88	19.81	10.10 ± 1.05	10.08	0.2
2/3	299.90	6.13	19.63	12.76 ± 1.36	12.68	0.6
5/6	300.02	6.27	19.46	15.51 ± 1.68	15.16	2.3
1	300.23	6.50	19.31	17.75 ± 1.97	17.55	1.1

Table 3: Local Nusselt number, Nu_x, versus distance along the vertical flat plate, x/L, results for $Gr_L^* = 5.6 \times 10^7$.

LAMINAR NATURAL CONVECTION ALONG A VERTICAL FLAT PLATE

PARAMETERS

$Gr_L^* = 1.1 \times 10^8 \pm 5.84 \times 10^6$

$Pr = 0.71$

$q_e = 49.73\ W/m^2$

$T_{air} = 294.25\ K$

	EXPERIMENTAL				THEORETICAL	
x/L	T (K)	q_{rad} (W/m^2)	q_{cnv} (W/m^2)	Nu_x	Nu_x	Δ (%)
1/24	299.56	5.68	44.05	2.01 ± 0.24	1.58	27.2
1/12	300.65	6.88	42.85	3.25 ± 0.30	2.75	18.2
1/6	301.94	8.32	42.07	5.22 ± 0.46	4.79	9.0
1/4	302.65	9.12	41.41	7.03 ± 0.63	6.63	6.0
1/3	303.22	9.76	40.95	8.65 ± 0.80	8.34	3.7
1/2	304.02	10.68	40.60	11.64 ± 1.13	11.54	0.9
2/3	304.42	11.14	40.28	14.73 ± 1.46	14.53	1.4
5/6	304.64	11.40	39.96	17.89 ± 1.80	17.37	3.0
1	305.03	11.84	39.68	20.46 ± 2.11	20.10	1.8

Table 4: Local Nusselt number, Nu_x, versus distance along the vertical flat plate, x/L, results for $Gr_L^* = 1.1 \times 10^8$.

LAMINAR NATURAL CONVECTION ALONG A VERTICAL FLAT PLATE

PARAMETERS

$Gr_L^* = 1.6 \times 10^8 \pm 8.02 \times 10^6$

$Pr = 0.71$

$q_e = 74.88\ W/m^2$

$T_{air} = 294.36\ K$

	EXPERIMENTAL				THEORETICAL	
x/L	T (K)	q_{rad} (W/m^2)	q_{cnv} (W/m^2)	Nu_x	Nu_x	Δ (%)
1/24	301.81	8.05	66.82	2.17 ± 0.26	1.70	27.6
1/12	303.35	9.80	65.08	3.49 ± 0.32	2.96	17.9
1/6	305.19	11.90	63.94	5.62 ± 0.49	5.16	8.9
1/4	306.18	13.06	62.97	7.58 ± 0.67	7.14	6.2
1/3	306.97	13.99	62.31	9.32 ± 0.84	8.99	3.7
1/2	308.09	15.32	61.82	12.56 ± 1.18	12.43	1.0
2/3	308.66	16.01	61.34	15.90 ± 1.53	15.65	1.6
5/6	308.97	16.38	60.89	19.33 ± 1.88	18.70	3.4
1	309.53	17.05	60.48	22.08 ± 2.21	21.64	2.0

Table 5: Local Nusselt number, Nu_x, versus distance along the vertical flat plate, x/L, results for $Gr_L^* = 1.6 \times 10^8$.

LAMINAR NATURAL CONVECTION ALONG A VERTICAL FLAT PLATE

PARAMETERS

$Gr_L^* = 2.1 \times 10^8 \pm 1.02 \times 10^7$

$Pr = 0.71$

$q_o = 100.19\ W/m^2$

$T_{air} = 294.26\ K$

	EXPERIMENTAL				THEORETICAL	
x/L	T (K)	q_{rad} (W/m^2)	q_{cnv} (W/m^2)	Nu_x	Nu_x	Δ (%)
1/24	303.65	10.25	89.94	2.30 ± 0.27	1.80	27.8
1/12	305.66	12.56	87.63	3.69 ± 0.33	3.13	17.9
1/6	307.98	15.30	86.15	5.94 ± 0.51	5.46	8.8
1/4	309.23	16.79	84.89	8.03 ± 0.69	7.55	6.4
1/3	310.24	18.02	84.03	9.88 ± 0.87	9.50	4.0
1/2	311.68	19.79	83.39	13.30 ± 1.22	13.14	1.2
2/3	312.42	20.71	82.77	16.82 ± 1.58	16.54	1.7
5/6	312.81	21.19	82.17	20.45 ± 1.95	19.77	3.4
1	313.54	22.11	81.62	23.34 ± 2.28	22.88	2.0

Table 6: Local Nusselt number, Nu_x, versus distance along the vertical flat plate, x/L, results for $Gr_L^* = 2.1 \times 10^8$.

LAMINAR NATURAL CONVECTION ALONG A VERTICAL FLAT PLATE

PARAMETERS

Gr_L^* = $2.7 \times 10^8 \pm 1.24 \times 10^7$

Pr = 0.71

q_e = 124.47 W/m^2

T_{air} = 294.30 K

	EXPERIMENTAL				THEORETICAL	
x/L	T (K)	q_{rad} (W/m^2)	q_{cnv} (W/m^2)	Nu_x	Nu_x	Δ (%)
1/24	305.38	12.19	112.28	2.42 ± 0.29	1.88	28.7
1/12	307.79	15.02	109.44	3.88 ± 0.35	3.28	18.3
1/6	310.56	18.37	107.63	6.24 ± 0.52	5.71	9.3
1/4	312.07	20.23	106.09	8.41 ± 0.72	7.90	6.5
1/3	313.27	21.72	105.03	10.36 ± 0.90	9.94	4.2
1/2	314.99	23.90	104.23	13.95 ± 1.27	13.75	1.5
2/3	315.86	25.02	103.47	17.64 ± 1.64	17.30	2.0
5/6	316.31	25.59	102.74	21.48 ± 2.02	20.69	3.8
1	317.18	26.72	102.08	24.51 ± 2.36	23.93	2.4

Table 7: Local Nusselt number, Nu_x, versus distance along the vertical flat plate, x/L, results for $Gr_L^* = 2.7 \times 10^8$.

LAMINAR NATURAL CONVECTION ALONG A VERTICAL FLAT PLATE

TRIAL 1

Gr_L^* = $5.6 \times 10^7 \pm 3.32 \times 10^6$

Pr = 0.71

q_o = 24.85 W/m^2

T_{air} = 294.17 K

TRIAL 2

Gr_L^* = $5.7 \times 10^7 \pm 3.36 \times 10^6$

Pr = 0.71

q_o = 24.96 W/m^2

T_{air} = 294.20 K

	TRIAL 1		TRIAL 2	
x/L	T (K)	Nu_x	T (K)	Nu_x
1/24	297.17	1.76 ± 0.22	297.20	1.77 ± 0.22
1/12	297.76	2.86 ± 0.28	297.80	2.86 ± 0.28
1/6	298.50	4.57 ± 0.43	298.54	4.58 ± 0.43
1/4	298.90	6.13 ± 0.59	298.94	6.15 ± 0.59
1/3	299.23	7.51 ± 0.74	299.27	7.53 ± 0.74
1/2	299.67	10.10 ± 1.05	299.71	10.14 ± 1.05
2/3	299.90	12.76 ± 1.36	299.94	12.81 ± 1.36
5/6	300.02	15.51 ± 1.68	300.06	15.56 ± 1.68
1	300.23	17.75 ± 1.97	300.27	17.81 ± 1.97

Table 8: Repeatability of local Nusselt number, Nu_x, versus distance along the vertical flat plate, x/L, results for $Gr_L^* = 5.6 \times 10^7$.

LAMINAR NATURAL CONVECTION ALONG A VERTICAL FLAT PLATE

TRIAL 1

Gr_L^* = $2.7 \times 10^8 \pm 1.24 \times 10^7$

Pr = 0.71

q_o = 124.47 W/m^2

T_{air} = 294.30 K

TRIAL 2

Gr_L^* = $2.7 \times 10^8 \pm 1.24 \times 10^7$

Pr = 0.71

q_o = 124.87 W/m^2

T_{air} = 294.31 K

	TRIAL 1		TRIAL 2	
x/L	T (K)	Nu_x	T (K)	Nu_x
1/24	305.38	2.42 ± 0.28	305.44	2.42 ± 0.28
1/12	307.79	3.88 ± 0.35	307.84	3.88 ± 0.35
1/6	310.56	6.24 ± 0.52	310.64	6.23 ± 0.52
1/4	312.07	8.41 ± 0.72	312.16	8.40 ± 0.72
1/3	313.27	10.36 ± 0.90	313.37	10.34 ± 0.90
1/2	314.99	13.95 ± 1.27	315.10	13.91 ± 1.26
2/3	315.86	17.64 ± 1.64	315.97	17.60 ± 1.63
5/6	316.31	21.48 ± 2.02	316.41	21.45 ± 2.02
1	317.18	24.51 ± 2.36	317.30	24.46 ± 2.36

Table 9: Repeatability of local Nusselt number, Nu_x, versus distance along the vertical flat plate, x/L, results for $Gr_L^* = 2.7 \times 10^8$.

GRID INDEPENDENCE CHECK FOR NATURAL CONVECTION COMPUTATIONS

PARAMETERS

Ra_{D_i} = 1.0×10^4

Pr = 0.70

D_o/D_i = 2.60

	Nu_θ							
GRID (r,θ)	10	30	60	90	120	150	170	AVE.
29 x 30	4.99	4.91	4.59	3.88	2.80	1.53	0.84	3.43
29 x 39	4.97	4.88	4.60	3.96	2.78	1.52	0.83	3.43
29 x 57	4.97	4.89	4.61	3.95	2.78	1.51	0.83	3.43
38 x 39	4.97	4.88	4.60	3.96	2.79	1.52	0.83	3.43

Table 10: Establishment of grid independence of results for the natural convection test problem.

LAMINAR NATURAL CONVECTION IN A HORIZONTAL CONCENTRIC ANNULUS

PARAMETERS

Ra_{D_i} = 1.0×10^4

Pr = 0.70

D_o/D_i = 2.60

		Nu_θ					
	GRID (r,θ)	30	60	90	120	150	AVE.
Present	29 x 39	4.88	4.60	3.96	2.78	1.52	3.43
Kuehn [22]	16 x 19	5.02	4.70	4.02	2.78	1.49	3.48

Table 11: Comparison of local Nusselt number, Nu_{D_i}, versus θ between present results and those of Kuehn [22].

INNER CYLINDER THERMOCOUPLE LOCATIONS

AXIAL LOCATION (mm)	THERMOCOUPLE LOCATIONS (deg.)
-38.1	-90, 0, 90, 180
-19.1	-165, -120, -75, -30, 30, 75, 120, 165
0.0	-135, -90, -45, 0, 45, 90, 135, 180
19.1	-150, -105, -60, -15, 15, 60, 105, 150
38.1	-90, 0, 90, 180

NOTES

(1) Axial distances are measured from the centre of the test section.

(2) Thermocouple locations are angles measured from the bottom of the cylinder in the counterclockwise direction.

Table 12: Location of thermocouples at the surface of the inner cylinder for the horizontal concentric annulus problem.

GRID INDEPENDENCE CHECK FOR NATURAL CONVECTION COMPUTATIONS

PARAMETERS

Ra_{D_i} = 9.88×10^4

Pr = 0.71

D_o/D_i = 2.33

$q_\bullet$ = 125.02 W/m^2

T_o = 298.82 K

	Nu_θ							
GRID (r,θ)	10	30	60	90	120	150	170	AVE.
29 x 39	7.89	7.99	7.95	7.03	6.15	4.53	2.47	6.28
38 x 39	7.88	7.97	7.93	7.03	6.15	4.53	2.47	6.27
38 x 57	7.91	8.00	7.98	7.05	6.23	4.60	2.46	6.32
38 x 75	7.91	7.95	8.01	7.12	6.21	4.59	2.46	6.32
38 x 111	7.92	7.96	8.01	7.13	6.22	4.60	2.46	6.33

Table 13: Establishment of grid independence of the natural convection computations.

GRID INDEPENDENCE CHECK FOR HEAT CONDUCTION COMPUTATIONS

PARAMETERS

Ra_{D_i} = 9.88×10^4

Pr = 0.71

D_o/D_i = 2.33

q_e = 125.02 W/m^2

T_o = 298.82 K

	q_{cnd_θ}						
GRID (r,θ)	10	30	60	90	120	150	170
52 x 75	8.10	4.96	14.03	8.48	-0.98	-9.46	-25.55
77 x 75	8.09	4.94	14.10	8.50	-0.98	-9.42	-25.52
102 x 75	8.09	4.93	14.14	8.52	-0.98	-9.40	-25.51
102 x 51	--	4.94	14.07	8.50	-0.97	-9.41	--
102 x 39	8.00	4.95	13.99	8.47	-0.97	-9.42	-25.13

Table 14: Establishment of grid independence of the heat conduction computations.

LAMINAR NATURAL CONVECTION IN A HORIZONTAL CONCENTRIC ANNULUS

PARAMETERS

Ra_{D_i} = $2.97 \times 10^4 \pm 3.20 \times 10^2$

Pr = 0.71

D_o/D_i = 2.33

q_e = 25.05 W/m^2

T_o = 298.63 K

		EXPERIMENTAL				THEORETICAL	
θ	T	q_{cnd}	q_{rad}	q_{cnv}	Nu_x	Nu_x	Δ
(deg)	(K)	(W/m^2)	(W/m^2)	(W/m^2)			(%)
0	303.86						
15	303.85	-3.75	5.82	22.98	6.36 ± 0.63	6.10	4.3
30	303.89	-2.38	5.87	21.56	5.92 ± 0.63	6.10	-3.0
45	303.95	-1.38	5.95	20.49	5.56 ± 0.62	6.05	-8.1
60	304.01	-2.81	6.02	21.84	5.86 ± 0.62	5.90	-0.7
75	304.13	-2.08	6.14	20.99	5.51 ± 0.61	5.78	-4.7
90	304.27	-1.92	6.31	20.67	5.29 ± 0.60	5.48	-3.5
105	304.44	-1.62	6.51	20.16	5.01 ± 0.58	5.02	-0.2
120	304.67	-0.63	6.77	18.91	4.52 ± 0.57	4.45	1.6
135	304.93	2.69	7.07	15.30	3.51 ± 0.55	3.80	-7.6
150	305.14	2.98	7.31	14.76	3.27 ± 0.54	2.95	10.8
165	305.33	5.33	7.54	12.18	2.62 ± 0.53	2.01	30.3
180	305.50						
180*	305.35						

Table 15: Local Nusselt number, Nu_{D_i}, versus θ results using an extrapolated temperature at θ = 180° for Ra_{D_i} = 2.97×10^4.

LAMINAR NATURAL CONVECTION IN A HORIZONTAL CONCENTRIC ANNULUS

PARAMETERS

Ra_{D_i} = $5.04 \times 10^4 \pm 3.98 \times 10^2$

Pr = 0.71

D_o/D_i = 2.33

q_e = 50.28 W/m^2

T_o = 298.68 K

		EXPERIMENTAL				THEORETICAL	
θ	T	q_{cnd}	q_{rad}	q_{cnv}	Nu_x	Nu_x	Δ
(deg)	(K)	(W/m^2)	(W/m^2)	(W/m^2)			(%)
0	307.96						
15	307.94	-7.49	10.55	47.22	7.31 ± 0.66	6.84	6.9
30	308.03	-3.15	10.66	42.77	6.56 ± 0.66	6.90	-4.9
45	308.12	-2.60	10.77	42.11	6.40 ± 0.65	6.86	-6.7
60	308.21	-6.19	10.88	45.59	6.86 ± 0.65	6.76	1.5
75	308.43	-3.07	11.14	42.21	6.21 ± 0.64	6.65	-6.6
90	308.67	-4.27	11.43	43.12	6.19 ± 0.63	6.23	-0.6
105	309.00	-3.12	11.82	41.57	5.78 ± 0.61	5.75	0.5
120	309.42	-0.84	12.33	38.79	5.18 ± 0.60	5.22	-0.8
135	309.89	4.85	12.90	32.53	4.16 ± 0.58	4.56	-8.8
150	310.27	3.86	13.36	33.05	4.09 ± 0.57	3.59	13.9
165	310.67	8.35	13.85	28.08	3.36 ± 0.55	2.48	35.5
180	311.08						
180*	310.69						

Table 16: Local Nusselt number, Nu_{D_i}, versus θ results using an extrapolated temperature at θ = 180° for Ra_{D_i} = 5.04×10^4.

LAMINAR NATURAL CONVECTION IN A HORIZONTAL CONCENTRIC ANNULUS

PARAMETERS

Ra_{D_i} = $6.83 \times 10^4 \pm 4.83 \times 10^2$

Pr = 0.71

D_o/D_i = 2.33

q_o = 75.50 W/m^2

T_o = 298.79 K

		EXPERIMENTAL				THEORETICAL	
θ	T	q_{cnd}	q_{rad}	q_{cnv}	Nu_x	Nu_x	Δ
(deg)	(K)	(W/m^2)	(W/m^2)	(W/m^2)			(%)
0	311.79						
15	311.77	-9.73	15.09	70.15	7.70 ± 0.69	7.30	5.5
30	311.89	-3.71	15.23	63.98	6.96 ± 0.68	7.36	-5.4
45	311.99	-4.51	15.35	64.66	6.98 ± 0.68	7.36	-5.2
60	312.11	-9.00	15.51	69.00	7.38 ± 0.67	7.31	1.0
75	312.43	-3.99	15.90	63.60	6.65 ± 0.66	7.15	-7.0
90	312.76	-6.11	16.31	65.29	6.66 ± 0.65	6.63	0.5
105	313.23	-4.69	16.90	63.29	6.25 ± 0.63	6.15	1.6
120	313.82	0.41	17.65	57.44	5.45 ± 0.62	5.67	-3.9
135	314.44	4.90	18.42	52.18	4.75 ± 0.60	5.01	-5.2
150	314.99	5.20	19.12	51.18	4.50 ± 0.59	4.03	11.7
165	315.57	11.57	19.87	44.07	3.74 ± 0.57	2.79	34.1
180	316.18						
180*	315.58						

Table 17: Local Nusselt number, Nu_{D_i}, versus θ results using an extrapolated temperature at $\theta = 180^\circ$ for $Ra_{D_i} = 6.83 \times 10^4$.

LAMINAR NATURAL CONVECTION IN A HORIZONTAL CONCENTRIC ANNULUS

PARAMETERS

Ra_{D_i} = $8.41 \times 10^4 \pm 5.65 \times 10^2$

Pr = 0.71

D_o/D_i = 2.33

q_e = 100.10 W/m^2

T_o = 298.81 K

		EXPERIMENTAL				THEORETICAL	
θ	T	q_{cnd}	q_{rad}	q_{cnv}	Nu_x	Nu_x	Δ
(deg)	(K)	(W/m^2)	(W/m^2)	(W/m^2)			(%)
0	315.19						
15	315.17	-12.62	19.33	93.38	8.10 ± 0.70	7.60	6.6
30	315.32	-4.33	19.52	84.90	7.29 ± 0.70	7.69	-5.2
45	315.43	-5.63	19.67	86.06	7.34 ± 0.70	7.73	-5.0
60	315.58	-11.84	19.85	92.08	7.79 ± 0.69	7.69	1.3
75	315.98	-5.37	20.37	85.11	7.03 ± 0.68	7.47	-5.9
90	316.42	-6.94	20.93	86.11	6.94 ± 0.67	6.91	0.4
105	316.99	-5.84	21.68	84.26	6.57 ± 0.65	6.42	2.3
120	317.73	0.17	22.65	77.27	5.79 ± 0.63	5.98	-3.2
135	318.51	6.71	23.66	69.72	5.02 ± 0.62	5.35	-6.2
150	319.18	5.22	24.55	70.33	4.90 ± 0.60	4.34	12.9
165	319.93	13.24	25.56	61.30	4.12 ± 0.59	3.01	36.9
180	320.76						
180*	319.95						

Table 18: Local Nusselt number, Nu_{D_i}, versus θ results using an extrapolated temperature at $\theta = 180^\circ$ for $Ra_{D_i} = 8.41 \times 10^4$.

LAMINAR NATURAL CONVECTION IN A HORIZONTAL CONCENTRIC ANNULUS

PARAMETERS

Ra_{D_i} = $9.88 \times 10^4 \pm 6.45 \times 10^2$

Pr = 0.71

D_o/D_i = 2.33

q_e = 125.02 W/m^2

T_o = 298.82 K

		EXPERIMENTAL				THEORETICAL	
θ	T	q_{cnd}	q_{rad}	q_{cnv}	Nu_x	Nu_x	Δ
(deg)	(K)	(W/m^2)	(W/m^2)	(W/m^2)			(%)
0	318.49						
15	318.47	-14.32	23.60	115.74	8.31 ± 0.72	7.85	5.9
30	318.64	-5.01	23.83	106.20	7.56 ± 0.71	7.95	-4.9
45	318.77	-7.26	23.99	108.30	7.66 ± 0.71	8.04	-4.7
60	318.94	-14.24	24.23	115.03	8.07 ± 0.71	8.00	0.9
75	319.43	-5.94	24.87	106.10	7.27 ± 0.69	7.72	-5.8
90	319.94	-8.68	25.56	108.14	7.22 ± 0.68	7.11	1.5
105	320.64	-6.45	26.49	104.99	6.79 ± 0.67	6.64	2.3
120	321.51	0.61	27.67	96.74	6.01 ± 0.65	6.21	-3.2
135	322.41	6.88	28.89	89.25	5.34 ± 0.63	5.60	-4.6
150	323.23	6.56	30.01	88.45	5.11 ± 0.62	4.60	11.1
165	324.13	16.16	31.26	77.60	4.33 ± 0.60	3.18	36.2
180	325.10						
180*	324.13						

Table 19: Local Nusselt number, Nu_{D_i}, versus θ results using an extrapolated temperature at $\theta = 180^\circ$ for $Ra_{D_i} = 9.88 \times 10^4$.

LAMINAR NATURAL CONVECTION IN A HORIZONTAL CONCENTRIC ANNULUS

TRIAL 1

Ra_{D_i} = $2.97 \times 10^4 \pm 3.20 \times 10^2$

Pr = 0.71

D_o/D_i = 2.33

q_e = 25.05 W/m^2

T_o = 298.63 K

TRIAL 2

Ra_{D_i} = $2.96 \times 10^4 \pm 3.20 \times 10^2$

Pr = 0.71

D_o/D_i = 2 33

q_e = 25.05 W/m^2

T_o = 298.68 K

	TRIAL 1		TRIAL 2	
θ (deg)	T (K)	Nu_{D_i}	T (K)	Nu_{D_i}
15	303.85	6.36 ± 0.63	303.90	6.44 ± 0.63
30	303.89	5.92 ± 0.63	303.95	5.80 ± 0.63
45	303.95	5.56 ± 0.62	304.01	5.56 ± 0.62
60	304.01	5.86 ± 0.62	304.07	5.95 ± 0.62
75	304.13	5.51 ± 0.61	304.19	5.39 ± 0.61
90	304.27	5.29 ± 0.60	304.32	5.35 ± 0.61
105	304.44	5.01 ± 0.58	304.50	5.03 ± 0.58
120	304.67	4.52 ± 0.57	304.73	4.47 ± 0.57
135	304.93	3.51 ± 0.55	304.98	3.50 ± 0.55
150	305.14	3.27 ± 0.54	305.19	3.38 ± 0.54
165	305.33	2.62 ± 0.53	305.40	2.72 ± 0.53

Table 20: Repeatability of local Nusselt number, Nu_{D_i}, versus θ results using an extrapolated temperature at θ = 180° for $Ra_{D_i} = 2.97 \times 10^4$.

LAMINAR NATURAL CONVECTION IN A HORIZONTAL CONCENTRIC ANNULUS

TRIAL 1

Ra_{D_i} = $9.88 \times 10^4 \pm 6.45 \times 10^2$

Pr = 0.71

D_o/D_i = 2.33

q_e = 125.02 W/m^2

T_o = 298.82 K

TRIAL 2

Ra_{D_i} = $9.65 \times 10^4 \pm 6.30 \times 10^2$

Pr = 0.71

D_o/D_i = 2.33

q_e = 124.81 W/m^2

T_o = 298.96 K

	TRIAL 1		TRIAL 2	
θ (deg)	T (K)	Nu_{D_i}	T (K)	Nu_{D_i}
15	318.47	8.31 ± 0.72	318.69	8.25 ± 0.72
30	318.64	7.56 ± 0.71	318.87	7.48 ± 0.71
45	318.77	7.66 ± 0.71	318.99	7.60 ± 0.71
60	318.94	8.07 ± 0.71	319.16	8.02 ± 0.70
75	319.43	7.27 ± 0.69	319.65	7.20 ± 0.69
90	319.94	7.22 ± 0.68	320.16	7.18 ± 0.68
105	320.64	6.79 ± 0.67	320.86	6.77 ± 0.66
120	321.51	6.01 ± 0.65	321.75	5.93 ± 0.65
135	322.41	5.34 ± 0.63	322.64	5.31 ± 0.63
150	323.23	5.11 ± 0.62	323.46	5.07 ± 0.62
165	324.13	4.33 ± 0.60	324.37	4.29 ± 0.60

Table 21: Repeatability of local Nusselt number, Nu_{D_i}, versus θ results using an extrapolated temperature at $\theta = 180^\circ$ for $Ra_{D_i} = 9.88 \times 10^4$.